THESE DE DOCTORAT

Présentée et soutenue publiquement

pour obtenir le titre de docteur des

UNIVERSITE PARIS-EST

et

ECOLE SUPERIEURE DE TECHNOLOGIE CHIMIQUE DE PRAGUE

par

Jindřich KOUBEK

Sujet: Etude rovibrationnelle de la bande ν_5 de DNO_3 et l´étude des effets collisionnels dans les spectres microonde de CH_3F sans et sous effet Stark

Soutenue le 15 Septembre 2011 devant le Jury composé de:

M.	C. Boulet	Prof. Dr., Université Paris-Sud, Orsay	Président
M.	F. Thibault	Dr., MCf HDR Université de Rennes I, Rennes	Rapporteur
M.	P. Pracna	Dr., Institut J. Heyrovský AS RT, Prague	Rapporteur
M.	J.-M. Hartmann	Dr., DR CNRS, LISA, Créteil	Examinateur
Mme	A. Perrin	Dr., DR CNRS, LISA, Créteil	Co-Directeur de thèse
M.	Š. Urban	Prof. Dr., ESTC Prague, Prague	Co-Directeur de thèse

Thèse en co-tutelle : Université Paris-Est (France) et Ecole Supérieure de technologie chimique de Prague (République Tchèque), préparée au LISA à Créteil (CNRS UMR 7583, Universités Paris Est-Créteil et Paris Diderot) et au LMSVR à Prague (Département de Chimie Analytique, ESTC).

Universite Paris-Est

Ecole doctorale: SIE – Sciences, Ingénierie et Environnement

Spécialité: Physique

Co-directrice de thèse: A. Perrin (DR, CNRS, LISA)

Ecole Supérieure de technologie chimique de Prague

Faculté de l'Ingénierie Chimique, Département de Chimie Analytique

Programme: Chimie

Domaine   Chimie Analytique

Co-directeur de thèse: Š. Urban (Prof., ESTC Prague)

THESIS

presented and publicly defended

to obtain the doctorate degree of

UNIVERSITE PARIS-EST

and

INSTITUTE OF CHEMICAL TECHNOLOGY, PRAGUE

by

Jindřich KOUBEK

Subject: Rovibrational study of DNO_3 ν_5 band and collisional effect studies of CH_3F microwave spectra with and without Stark effect

Defended on 15th of September 2011 in front of a Jury composed of:

Mr.	C. Boulet	Prof. Dr., Université Paris-Sud, Orsay	President
Mr.	F. Thibault	Prof. Dr., Université de Rennes I, Rennes	Reviewer
Mr.	P. Pracna	Dr., J. Heyrovský Institute AS CR, Prague	Reviewer
Mr.	J.-M. Hartmann	Dr., DR CNRS, LISA, Créteil	Member
Mrs.	A. Perrin	Dr., DR CNRS, LISA, Créteil	Co-Advisor
Mr.	Š. Urban	Prof. Dr., ICT Prague, Prague	Co-advisor

Co-tutelle thesis: Université Paris-Est (France) and Institute of Chemical Technology, Prague (Czech Republic), prepared in LISA in Créteil (CNRS UMR 7583, Universités Paris Est-Créteil et Paris Diderot) and in LMSVR in Prague (Department of Chemical Analysis, ICT).

<u>Universite Paris-Est</u>

Graduate school: SIE– Sciences, Ingénierie et Environnement

Speciality: Physics

Thesis co-advisor: A. Perrin (DR, CNRS, LISA)

<u>Institute of Chemical Technology, Prague</u>

Faculty of Chemical Engineering, Department of Analytical Chemistry

Program: Chemistry

Domain: Analytical Chemistry

Thesis co-advisor: Š. Urban (Prof., ICT Prague)

DISERTAČNÍ PRÁCE

k získání doktorského titulu

UNIVERSITE PARIS-EST

a

VYSOKÁ ŠKOLA CHEMICKO-TECHNOLOGICKÁ V PRAZE

Vypracoval a veřejně obhájil

Jindřich KOUBEK

Téma: Rovibrační studie pásu ν_5 DNO$_3$ a studie kolizních efektů v

mikrovlnných spektrech CH$_3$F pod vlivem a bez vlivu Starkova jevu

Obhájeno 15. září 2011 před komisí ve složení:

C. Boulet	prof. Dr., Université Paris-Sud, Orsay	Předseda
F. Thibault	prof. Dr., Université de Rennes I, Rennes	Oponent
P. Pracna	Dr., Ústav J. Heyrovského AV ČR, Praha	Oponent
J.-M. Hartmann	Dr., DR CNRS, LISA, Créteil	Zkoušející
A. Perrin	Dr., DR CNRS, LISA, Créteil	Školitelka
Š. Urban	prof. Dr., VŠCHT Praha, Praha	Školitel

Dizertační práce byla vypracována v rámci doktorátu pod dvojím vedením (co-tutelle) na Université Paris-Est (Francie) a Vysoké škole chemicko-technologické v Praze (Česká republika), v laboratořích LISA (CNRS UMR 7583, Universités Paris Est - Paris Diderot, Créteil) a LMSVR (Ústav analytické chemie, VŠCHT Praha).

Université Paris-Est

Škola PGS: SIE– Sciences, Ingénierie et Environnement

Specializace: Fyzika

Školitelka co-tutelle: A. Perrin (DR, CNRS, LISA)

Vysoká škola chemicko-technologické v Praze

Fakulta chemicko-inženýrská, Ústav analytické chemie

Studijní program: Chemie

Studijní obor: Analytická chemie

Školitel co-tutelle: Š. Urban (prof., VŠCHT Praha)

Résumé

Le travail qui est présenté dans ce mémoire de thèse s'inscrit dans le domaine de la Spectroscopie moléculaire en phase gazeuse théorique et expérimentale. Il comprend deux parties dédiées à des aspects relativement différents de cette discipline.

La première partie présente l'analyse à haute résolution des positions et intensité des raies de la bande ν_5 (ouverture angulaire du groupe NO_2 dans le plan de la molécule) de DNO_3 dans la région spectrale de 11 μm. Pour ce faire, nous avons utilisé un spectre infrarouge enregistré dans la région $700-1400$ cm^{-1} à l'aide d'un spectromètre à transformée de Fourier de l'université « Bergische Universität » à Wuppertal, en Allemagne. Ce travail nous a permis de montrer que la bande ν_5, centrée à 887.657 cm^{-1}, est fortement perturbée. L'analyse prouve en effet que les niveaux d'énergie 5^1 et 7^1+9^1 sont couplés par des résonances de Coriolis de types A et B. Le schéma de résonances pour la variété isotopique DNO_3 diffère donc fortement de ceux observés pour les états 5^1 et 9^2 de $H^{14}NO_3$ et $H^{15}NO_3$ qui sont majoritairement de type Fermi.

Le deuxième problème abordé dans ce travail est celui des profils de raies rotationnelles pures de CH_3F avec l'étude des élargissements collisionnels (collisions CH_3F-CH_3F et CH_3F-He) des transitions optiques et de leurs composantes Stark. Des mesures microondes ont été réalisées à l'ESTC à Prague. Leur analyse a permis d'en extraire des paramètres collisionnels à l'aide de divers profils de raies (Voigt, Rautian, dépendantes de vitesse) pour les transitions $J, K \rightarrow J + 1,\ K$ $(K = 0,\ \ldots,\ J)$ avec $J = 1$ et $J = 3$ et leurs diverses composantes Stark $J, K, M \rightarrow J + 1,\ K,\ M'$ $(|M| = 0,\ \ldots, J\,;\ |M - M'| = 0, 1)$. De plus, un modèle fondé sur l'approximation Infinite Order Sudden (IOS) a été construit pour décrire les effets d'interférences collisionnelles observés. Les résultats expérimentaux obtenus complètent et étendent des travaux précédents et sont la première démonstration de la capacité de l'approximation IOS à modéliser les couplages collisionnels entre composantes Stark.

Mots clefs: DNO_3, spectroscopie infrarouge, positions, intensités, résonance Coriolis, bande ν_5, bande $\nu_7 + \nu_9$, CH_3F, spectroscopie microonde, profils de raies, profil de Rautian, profil avec dépendance de vitesse, élargissement collisionel, effet Stark, moment dipolaire, couplage des raies, approximation IOS.

Summary

The work presented in this thesis belongs to the domain of theoretical and experimental gas phase molecular spectroscopy. It consists of two parts dedicated to two relatively different aspects in this field.

The first part presents a high resolution analysis of the ν_5 fundamental band (NO_2 in plane bending mode) positions and intensities of $D^{14}NO_3$ (deuterated nitric acid) in the $11\,\mu$m spectral region. For this study, we used an infrared spectrum of $D^{14}NO_3$ recorded in the $700-1400$ cm^{-1} region on a Fourier transform spectrometer at Bergische Universität in Wuppertal (Germany). Our analysis demonstrates that the fundamental ν_5 band centered at 887.657 cm^{-1} is strongly perturbed. Indeed, it proves that 5^1 and 7^1+9^1 energy levels of DNO_3 are coupled through A and B type Coriolis resonances. The resonance scheme for the isotopologue $D^{14}NO_3$ therefore differs substantially from the schemes of $H^{14}NO_3$ and $H^{15}NO_3$ that feature dominantly Fermi type resonances.

The second theme treated in this work is devoted to the lineshapes of pure rotational transitions of CH_3F with the study of collisional broadening (collisions CH_3F-CH_3F and CH_3F-He) of optical transitions and their Stark components. The microwave measurements were realised at ICT in Prague. Their analysis enabled to provide collisional parameters using various line profiles (Voigt, Rautian, Speed dependent) for the $J, K \rightarrow J + 1, K$ ($K = 0, \ldots, J$) transitions with $J = 1$ and $J = 3$ as well as for their various Stark components $J, K, M \rightarrow J + 1, K, M'$ ($|M| = 0, \ldots, J$; $|M - M'| = 0, 1$). Moreover, a correct use of model based on Infinite Order Sudden approximation led to very satisfactory results of the observed line-mixing effects. The retrieved experimental results complete and extend the previous studies and provide the first successful demonstration of the ability of the IOS approximation to model line-mixing effects among Stark transitions.

Key words: DNO_3, Infrared spectroscopy, Positions, Intensities, Coriolis resonance, ν_5 band, $\nu_7 + \nu_9$ band, CH_3F, Microwave spectroscopy, Line shapes, Rautian profile, Speed dependent profile, Collisional broadening, Stark effect, Dipole moment, Line-Mixing, IOS

Shrnutí

Předkládaná dizertační práce tematicky zahrnuje jak teoretickou, tak i experimentální molekulovou spektroskopii v plynné fázi. Předmětem práce jsou dvě relativně nezávislé studie, které spojuje právě zaměření na vysoce rozlišenou spektroskopii plynů.

V první části je vypracována analýza poloh a intenzit linií vysoce rozlišeného spektra základního vibračního pásu ν_5 (mód kyvadlové rovinné vibrace skupiny NO_2) DNO_3 v 11 μm spektrální oblasti. V této studii bylo použito infračervené spektrum naměřené v rozsahu $700-1400$ cm^{-1} na FT spektrometru v Bergische Universität ve Wuppertalu (Německo). Tato práce ukazuje, že základní pás ν_5 o poloze 887.657 cm^{-1} je silně porušen. Podrobná analýza naměřených spekter dokázala, že energetické hladiny 5^1 a 7^1+9^1 jsou spřaženy prostřednictvím Coriolisových rezonancí typu A a B. Rezonanční schéma isotopologu DNO_3 se tedy podstatně liší od rezonancí pozorovaných u $H^{14}NO_3$ a $H^{15}NO_3$, kde mezi stavy 5^1 a 9^2 dominují Fermiho rezonance.

Druhá část práce se věnuje profilům čistě rotačních linií CH_3F. Studováno je kolizní rozšíření (kolize CH_3F s CH_3F a kolize CH_3F s He) rotačních přechodů a jejich Starkových komponent. Mikrovlnná spektra byla naměřena na VŠCHT Praha. Jejich analýza vedla k určení kolizních parametrů vybraných profilů (Voigtův, Rautianův, rychlostně závislé profily) u přechodů $J, K \rightarrow J + 1, K$ ($K = 0, \ldots, J$) s $J = 1$ a $J = 3$ a jejich Starkových komponent $J, K, M \rightarrow J + 1, K, M'$ ($|M| = 0, \ldots, J$; $|M - M'| = 0, 1$). Navíc byl pro popis pozorovaných kolizních interferenčních jevů sestaven model založený na Infinite Order Sudden (IOS) aproximaci. Získané výsledky doplňují a rozšiřují předchozí práce a jsou zároveň první úspěšnou aplikací aproximace IOS pro modelování kolizního spřažení (line-mixing) mezi Starkovými komponentami.

Klíčová slova: DNO_3, infračervená spektroskopie, pozice, intenzita, Coriolisovy rezonance, pás ν_5, pás $\nu_7 + \nu_9$, CH_3F, mikrovlnná spektroskopie, profily linií, Rautianův profil, rychlostně závislý profil, kolizní rozšíření, Starkův jev, dipólový moment, Line-Mixing, model IOS

Thesis aims (form as required by ICT Prague)

The thesis projects aim at three tasks:

1. Analysis of rovibrational spectra of the deuterated nitric acid (DNO$_3$) fundamental band ν_5 with respect to the interactions between states 5^1 and $7^1 9^1$.

2. Measurement of the methyl fluoride (diluted or not in helium) pure rotational microwave spectra with and without Stark effect.

3. Analysis of the collisional effects observed in the measured spectra of CH$_3$F, comparison of the Stark lines' experimental collisional broadening values with those calculated using Infinite Order Sudden (IOS) approximation method.

Acknowledgements

Contents

I   Introduction

The work presented in this thesis had been done in the frame of co-tutelle thesis program organized by Université Paris-Est (UPE) and by Institute of Chemical Technology, Prague (ICT Prague). Some studies have been carried out in the Laboratoire Interuniversitaire des Systèmes Atmosphériques (LISA, CNRS UMR 7583) under the supervision of Dr. Agnès Perrin and at the Department of Analytical Chemistry (DAC-402) of ESCT Prague in the laboratory LMSVR under direction of Prof. Štěpán Urban. Another topic of the thesis, suggested at the end of the first year of the co-tutelle, was studied afterwards and continued further on, in cooperation with Dr. Jean-Michel Hartmann (LISA) and Prof. Christian Boulet (ISMO). The text describes therefore two completely independent spectroscopic studies, as the thesis name suggests: an analysis of the infrared spectra of deuterated nitric acid (DNO_3) and an analysis of collisional effects in the Stark and non Stark microwave spectra of the methyl fluoride (CH_3F). These two subjects are introduced in the following two sections. The lay-out of the thesis text is presented afterwards.

I.1   Rovibrational study of DNO_3 ν_5 band

Nitric acid (HNO_3) plays an important role as a ''reservoir'' molecule for both the NO_x (nitrogen oxides) and HO_x (hydrogen oxides) species in the stratosphere ([1, 2]). These radicals are potentially active contributors to the ozone destruction in the stratosphere through catalytic reactions. The 11 μm region corresponds to one of the strongest absorption bands of nitric acid and coincides with a rather clear atmospheric window of the atmosphere. This spectral region is therefore commonly used for the retrieval of nitric acid in the atmosphere, not only for the most abundant isotopic species ($H^{14}NO_3$, Refs. ([3, 4]) and references therein) but also for $H^{15}NO_3$ (isotopic concentration of about $\alpha \sim .00365(7)$) which could be detected by MIPAS (Michelson Interferometer for Passive Atmospheric Sounding) aboard the ENVISAT satellite ([5]). For this reason, numerous spectroscopic studies were devoted to the improvement of line position, line intensities (([6-9]) and references therein) and line broadening parameters ([10]) for nitric acid at 11 µm for both the $H^{14}NO_3$ and $H^{15}NO_3$ species.

On the other hand, the chances to detect DNO_3 in atmospheric spectra at 11 μm are rather weak. DNO_3 exists with rather weak isotopic abundance in a natural sample of nitric acid ($\alpha \sim 1.55 \ 10^{-4}$) and the ν_5 band of DNO_3 is located at 887.7 cm^{-1} in the middle of the 11 μm absorption region for $H^{14}NO_3$, where strong absorptions from the ν_5, $2\nu_9$ and $\nu_5+\nu_9-\nu_9$ Q-

branches are clearly observable in atmospheric spectra at 879.109, 896.448, 885.424 cm^{-1}, respectively. However studying DNO_3 is interesting since it provides input for the validation of recent and future *ab initio* studies on nitric acid (*11*). Indeed the resonance scheme for the interacting DNO_3 vibrational states differs as compared to $H^{14}NO_3$ and $H^{15}NO_3$.

I.2   Collisional effect studies of CH$_3$F microwave spectra with and without Stark effect

Line-mixing (LM) is a process manifesting through transfers of intensity among overlapping optical transitions and resulting from rotational population exchanges induced by inter-molecular collisions. It has been the subject of numerous experimental and theoretical studies for various molecular systems and types of spectra, as reviewed in Chapter IV of Ref. (*17*). However, few of these studies have considered the case of collisional exchanges among Stark resolved molecular lines, i.e. when an applied electric field removes the spatial degeneracy of the rotational levels. As first shown by Bréchignac (*12*) and afterwards measured (*13-15*) for CH_3F in the IR region, the "zero field widths" are much smaller than the widths of the various Stark resolved lines. Various theoretical treatments have been proposed to describe collisional couplings between *M*-components. Let us first mention the pioneering work of Buffa, Tarrini and co-workers (*13*), based on a generalization of the well known Anderson-Tsao-Curnutte (ATC) model (*16*). An alternative approach to take LM into account is to build the associated relaxation matrix using the Infinite Order Sudden (IOS) approximation (*17, 18*) or its improved Energy Corrected Sudden (ECS) extension (*17, 19, 20*). IOS/ECS models have enabled precise modeling of LM effects for many systems and types of spectra (*17*), including hyperfine components due to nuclear spin (*21, 22*) and symmetric-top spectra (*23, 24*). However, quite surprisingly, as shown in Ref. (*14*), the IOS model developed in (*12*) apparently failed to reproduce the details of coupling processes between the Stark components of CH_3F lines. With the aim of clarifying this result we have re-examined the problem and the present work shows that this failure was only due to an oversimplification of the IOS formalism.

During the analysis of the measured CH_3F pure rotational spectra using Voigt line shapes, a "W signature", characteristic of a narrowing, was observed in the fits residuals. The line shapes were therefore also studied with more refined models that involve a more thorough description of collisional effects by taking Dicke and speed dependence effects into account,

in order to attempt to diminish the residuals and to understand the contributions of various collisional processes.

* * *

The remained of the thesis text is divided into the following parts:

After this introductory chapter, a chapter dedicated to infrared spectra of deuterated nitric acid is presented, in which the general theory is first recalled. Then the model used for the rovibrational spectra of asymmetric top molecules like DNO_3 is discussed following the approach established by J.K.G. Watson for cases with vibrationaly isolated states and generalised further by J.-M. Flaud and C. Camy-Peyret for cases with interacting vibrational states. The final section of the chapter presents the results of the analysis of ν_5 band of DNO_3 using the previously mentioned formalism.

The next three chapters are devoted to collisional effects on rotational spectra of CH_3F. The third chapter describes the experimental apparatus used for in this study as well as some experimental details on the measurements made using the Stark effect.

The fourth chapter is devoted to the analysis of the shapes of isolated lines in the pure rotational CH_3F spectra. Some general theory is first mentioned before some selected models describing isolated line profiles are discussed. The results obtained CH_3F $J = 1$ and $J = 3$ pure rotational transitions are then presented and discussed.

The fifth chapter is devoted to the analysis of the Stark pure rotational CH_3F spectra in situations when lines overlap and collisional line mixing effect get involved. The modelling of this effect using the Infinite Order Sudden (IOS) approximation is detailed before the analysis of Stark and non Stark CH_3F (pure or diluted in helium) $J = 1$ and $J = 3$ pure rotational transitions is presented.

The next and final parts cover a general conclusion, references and appendices.

II Vibration –rotation study for a molecule of atmospheric and theoretical interest: the case of the DNO_3 isotopomer of nitric acid

The present chapter is organized in the following way. Paragraph II.1 will describe the overall approximation which led to establish the vibration rotational Hamiltonian written in the form given by Darling and Dennison. Assuming that the nuclei vibrations are small compared to the interatomic distances, the Hamiltonian can be developed in series according to the vibrational quanta. The structure of the DNO_3, its vibrational modes, its symmetry properties will be presented in Paragraph II.2.1 together with the rigid rotor rotational wavefunctions. The selection rules for an electric dipole moment transition will be deduced in Paragraph II.2.3. The "contact transformations" which lead to a partial block diagonalization of the vibration rotation Hamiltonian will be presented in Paragraph II.2.4. Finally the effective Hamiltonian used in this work will be described shortly in Paragraph II.3.4.

II.1 General considerations, Rovibrational Hamiltonian

A molecule can be considered as a rather stable aggregate of atomic nuclei and electrons. The time dependence of $\Phi(t)$ is defined by the Schrödinger equation:

$$i\hbar\frac{\partial\Phi(t)}{\partial t}=H\Phi(t) \tag{II.1}$$

where $\Phi(t)$ is the molecule wavefunction of the molecule which is function of its electronic and nuclear coordinates. In Eq. (II.1) H is the Hamiltonian of the molecule which is assumed, in the following, to be time independent. In this way the $\Phi(t)$ eigenfunctions for the different stationary states are solutions of the equation:

$$H\Phi(t) = E\ \Phi(t) \tag{II.2}$$

Solving Eq. (II.2) for a molecular system consisting in moving particles (several atoms and numerous electrons) is usually impossible. Several more or less severe approximations must be formulated.

¤ The Born Oppenheimer approximations (*25*):

The fact that the nuclei are much heavier than electrons (neutron-electron mass ratio $m_n/m_e = 1838.683\ 6605(11)$ – 2006 CODATA values (*26*), proton-electron mass ratio $m_p/m_e = 1836.152\ 672\ 47(80)$) led Born and Oppenheimer (*25*) to formulate approximation that fast movements of electrons are separated from the relatively slow movements of nuclei. The rovibronic (electronic vibration rotational) Hamiltonian then takes the form:

$$H_{evr} = H_e + H_{vr}, \tag{II.3}$$

where H_e is electronic Hamiltonian describing the movements of electrons considered for a given fixed nuclear geometry, and H_{vr} is the rovibrational (vibration rotational) Hamiltonian describing the movement of the nuclei for the corresponding electronic state.

In the following of this manuscript, the Born Oppenheimer approximation is assumed to be appropriate. The studies presented here are for molecules (nitric acid and methyl fluoride) in their ground electronic state.

¤ The molecules under study are assumed to be isolated and moving in an isotropic laboratory space. By using a reference system of axes centered at the molecular center of gravity, *O*, the translation of the center of inertia is completely separated from the internal

coordinates (vibration and rotation) of the molecule. The so-called vibration-rotational Hamiltonian involve $3N - 3$ degrees of freedom, for a molecule with N nuclei. We are dealing with non linear polyatomic molecules, and the molecular rotation and the nuclear vibrations around their equilibrium positions are associated to 3 and $3N - 6$ degrees of freedom, respectively.

¤ It is assumed that the amplitudes of the nuclei vibrations are small compared to the interatomic distances. This is relevant for the present DNO_3 study. Let us mention, however, that this approximation fails when considering the OH torsional motion (v_9 mode) for the H isotopomers of nitric acid ($H^{14}NO_3$ and $H^{15}NO_3$).

Even in such conditions, it is not possible to separate completely rotation from the vibration motion. At this level we need to define two orthogonal systems of axes centered at O, the molecular center of gravity: a floating O_{xyz} - reference system of molecular axis – bound to a reference molecular configuration (i.e. equilibrium configuration in case of rigid or semi-rigid molecules) and the O_{XYZ} "laboratory fixed" reference system that is in translational motion relative to the laboratory system. In order to fix the origin, O, of both systems to the center of gravity of the molecule, the following relationship applies:

$$\sum_{i=1}^{N} m_i \, \mathbf{r}_i = \mathbf{0} \tag{II.4}$$

where $\mathbf{r}_i$ is instantaneous radius vector of nucleus i with mass m_i.

In order to minimize the interactions between rotation and vibration, Eckart wrote the following constrains (27) which set the orientation of O_{xyz} relative to O_{XYZ} :

$$\sum_{i=1}^{N} m_i \, \mathbf{r}_i^0 \wedge \mathbf{r}_i = \mathbf{0} \, , \tag{II.5}$$

where $\mathbf{r}_i^0$ is radius vector of nucleus i at its reference position.

In this way, the vibration-rotation Hamiltonian, as developed by Darling-Dennison (28) takes the following form, presented here as it was simplified later by Watson (29):

$$H = \frac{\hbar^2}{2} \sum_{\alpha,\beta} \left(J_\alpha - \pi_\alpha \right) \mu_{\alpha\beta} \left(J_\beta - \pi_\beta \right) + \frac{1}{2} \sum_k P_k^2 + U + V \tag{II.6}$$

In this equation, α and β refer to the molecular axes with values x, y or z, k refers to the $3N - 6$ normal coordinates Q_k. The other symbols are defined as follows:

- J_α are components of the molecular axes of the total angular momentum in $\hbar$ units

- π_α are components on the molecular axes of the vibrational moment defined as:

$$\pi_\alpha = \frac{1}{\hbar} \sum_{k,l} \varsigma^\alpha_{k,l} Q_k P_l \tag{II.7}$$

- $\mu_{\alpha\beta}$ is matrix element (α, β) of the inverse matrix of the effective inertia tensor referring to the O_{xyz} molecular system of axis

- P_k is conjugate moment to the normal coordinate Q_k, and V is the vibrational potential energy function whose quadratic part can be diagonalized through the $3N - 6$ vibrational coordinates:

$$V = \tfrac{1}{2} \sum_{k=1}^{(3N-6)} \lambda_k Q_k^2 + ... \tag{II.8}$$

and:

-   $U = \sum_\alpha \mu_{\alpha\alpha}$, $\tag{II.9}$

as shown by J.K.G. Watson (29)

In the following of the text, we will use q_k, p_k which are the dimensionless normal coordinates and their conjugate momenta defined by:

$$q_k = \frac{\lambda_k^{1/4}}{\hbar^{1/2}} Q_k, \quad p_k = -i \frac{\partial}{\partial q_k} \tag{II.10}$$

In case of small vibrations (in comparison to interatomic distances), V and $\mu_{\alpha\beta}$ can be expanded as series in the normal coordinates q_k:

$$H = H_0 + H_1 + H_2 + ... \tag{II.11}$$

with:

$$H_0 = \frac{1}{2} \sum_k \omega_k \left(p_k^2 + q_k^2 \right) + \sum_\alpha B_\alpha J_\alpha^2 \tag{II.12}$$

$$H_1 = \sum_k \sum_{\alpha,\beta} B_k^{\alpha,\beta} J_\alpha J_\beta q_k - 2 \sum_{k,l} \left(\frac{\omega_l}{\omega_k} \right)^{1/2} q_k p_l \sum_\alpha B_\alpha \varsigma^\alpha_{kl} J_\alpha + \sum_{k<l<m} K_{klm} q_k q_l q_m \tag{II.13}$$

$$H_2 = \frac{3}{8} \sum_{k,l} q_k q_l \sum_{\alpha,\beta,\gamma} \left(B_k^{\gamma\alpha} B_l^{\gamma\beta} + B_k^{\gamma\beta} B_l^{\gamma\alpha} \right) B_\gamma^{-1} J_\alpha J_\beta - \sum_k \sum_{\alpha,\beta} B_k^{\alpha\beta} \left(\pi_\alpha q_k + q_k \pi_\alpha \right) J_\beta$$
$$+ \sum_\alpha B_\alpha \pi_\alpha^2 - \frac{1}{4} \sum_\alpha B_\alpha + \sum_{k<l<m<n} K_{klmn} q_k q_l q_m q_n \tag{II.14}$$

In these formulas,

- ω_k is the harmonic vibrational wavenumber of the kth normal mode:

$$\omega_k = \frac{\lambda_k^{1/4}}{2\pi c} \tag{II.15}$$

- B_α is the equilibrium rotational constants (in cm^{-1}):

$$B_\alpha = \frac{\hbar}{8\pi^2 c I_\alpha} \tag{II.16}$$

- $B_k^{\alpha,\beta}$ are rotational derivatives:

$$B_k^{\alpha,\beta} = \left(\frac{\partial \mu_{\alpha\beta}}{\partial q_k} \right)_0, \left(B_k^{\gamma\alpha} B_l^{\gamma\beta} + B_k^{\gamma\beta} B_l^{\gamma\alpha} \right) B_\gamma^{-1} = \left(\frac{\partial^2 \mu_{\alpha\beta}}{\partial q_k \partial q_l} \right)_0 \tag{II.17}$$

- ς_{kl}^α are Coriolis coupling constants

- π_α are components on the molecular axes of the vibrational momentum:

$$\pi_\alpha = \frac{1}{\hbar} \sum_{k,l} \varsigma_{k,l}^\alpha q_k p_l \left(\frac{\omega_l}{\omega_k} \right)^{1/2} \tag{II.18}$$

- K_{klm}, (resp. K_{klmn}) are cubic, (resp. quartic) potential constants.

We can rewrite the Eq. (II.12) as:

$$H_0 = H_0^{vib} + H_0^{rot}, \tag{II.19}$$

where

$$H_0^{vib} = \frac{1}{2} \sum_{k=1}^3 \omega_k \left(p_k^2 + q_k^2 \right), \tag{II.20}$$

$$H_0^{rot} = \sum_\alpha B_\alpha J_\alpha^2 \,, \qquad\qquad\qquad\qquad\qquad\qquad\qquad (\text{II.21})$$

with $\omega_k, B_\alpha, H_0^{vib}, H_0^{rot}$ in cm^{-1}.

The zeroth order Hamiltonian is a rough approximation. At this level, the vibration and rotation are separated, and it is easy to label the vibrorotational energy levels. We will detail the description of the eigenfunctions and eigenvalues of the rotational and vibrational zeroth order Hamiltonian. Let us remind, however, that at higher orders (H_1, H_2 and over …) the vibration and rotational motions are coupled.

II.2 Application to the nitric acid molecule

II.2.1 Description of the molecule

II.2.1.1 Nitric acid structure

Figure II.1 gives the structure of nitric acid molecule which is planar in its equilibrium configuration.
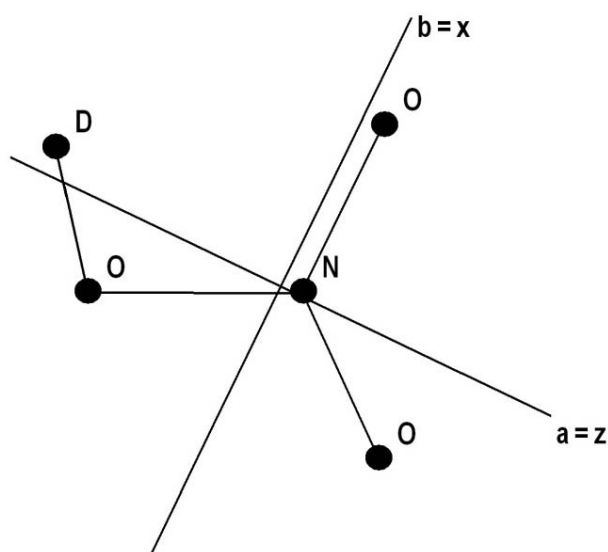
Fig. II.1 Scheme of DNO$_3$ structure.

Recently, a semi-experimental equilibrium structure has been derived from experimental ground state rotational constants achieved for several isotopomers of nitric acid ((*30*), (*31*) and Refs. therein) and of rovibrational interaction parameters calculated from the ab initio force field. In this way, the best equilibrium structure was found to be

r_e(N=O$_{syn}$) = 1.209(1) Å, r_e(N=O$_{anti}$) = 1.194(1) Å, r_e(N-O) = 1.397(1) Å,

r_e(O−H) = 0.968(1) Å, ∠(ONO$_{syn}$) = 115.8(1)°, ∠(ONO$_{anti}$) = 114.2(1)° and

∠(NOH) = 102.2(1)° (*11*).

II.2.1.2 Inertia axes and rotational constants

Figure II.1 gives also the system of principal axes for the DNO$_3$ isotopomer. As compared to H^{14}NO$_3$, the inertia system of axes rotates of about 9° clockwise from H^{14}NO$_3$ to D^{14}NO$_3$.

DNO$_3$ is an asymmetric top molecule (it has three different inertial moments). Following the common usage, the three principal inertial constants are noted as $B_a = A$, $B_b = B$ and $B_c = C$ and ordered by the relation $A \geq B \geq C$.

	A (cm^{-1})	B (cm^{-1})	C (cm^{-1})	Ref.
H^{14}NO$_3$	0.43399948	0.40360889	0.2088321	(30)
H^{15}NO$_3$	0.43404204	0.40350885	0.20881543	(31)
DNO$_3$	0.43265388	0.37734832	0.2013037	(31)

Table II.1 Ground state rotational constants for the H^{14}NO$_3$, H^{15}NO$_3$ and D^{14}NO$_3$ isotopomers of nitric acid.

Table II.1 gives the ground state rotational constants for the H^{14}NO$_3$, H^{15}NO$_3$ and D^{14}NO$_3$ isotopomers. The following approximation holds:

$$A \sim B \sim 2C \tag{II.22}$$

Therefore nitric acid may be considered as a "near oblate rotor".

For a near-symmetric top molecule, it is useful to define the (x,y,z) reference axes, choosing the z axis as the symmetry axis of the rotor. In this way, the standard base $|J\ k\rangle$ formed by eigenvectors common to $\mathbf{J}^2$ and J_z is the bases of all rotational wavefunctions. The eigenstates and eigenvalues of the asymmetric Hamiltonian rotor, H_0^{rot}, are retrieved by diagonalization of matrix associated to the standard base $|J\ k\rangle$. Different conventions can be chosen for the orientation of the (x, y, z) reference system for the symmetric rotor relative to the (a,b,c) inertia axes of the actual molecule. Naturally the III^r representation, with $z = c$, $x = a$, $y = b$ seems the most appropriate for a near oblate molecule like nitric acid, because c is the z- reference axis. However, the most recent and accurate determinations of the rotational constants for various isotopomers of nitric acid by millimeter wave techniques (30, 31) were satisfactorily performed using a rotational Hamiltonian written in the I^r representation ($x = b$, $y = c$, $z = a$), and the so called A-type reduction which will be defined further in the text. Therefore the I^r convention was also adopted in this study. Under these conditions, the zeroth order rotational Hamiltonian has following form:

$$H_0^{rot} = AJ_z^2 + BJ_x^2 + CJ_y^2 \tag{II.23}$$

The eigenstates of H_0^{rot} are labeled by $J\ K_a\ K_c$, K_a and K_c being associated, respectively, to the components of the total kinetic moment $\vec{J}$ on molecular axes a and c. Though these two last labels are not well behaved quantum numbers, nevertheless the triplet $J\ K_a\ K_c$ (that follows conditions $0 \le K_a \le J$, $0 \le K_c \le J$ and $K_a + K_c = J$ or $J+1$) enables labeling of the molecular rotational energy levels in a single way.

Equation of the eigenvalues of H_0^{rot} has the form:

$$H_0^{rot} \left| J\ K_a\ K_c \right\rangle_0 = E_{0(J\ K_a\ K_c)}^{rot} \left| J\ K_a\ K_c \right\rangle_0 \tag{II.24}$$

II.2.1.3 Vibration

Nitric acid molecule has $3N - 6 = 9$ non degenerated vibrations.

Symmetry	Mode	Approximation type		$D^{14}NO_3$	Ref.	$H^{14}NO_3$	Ref.	$H^{15}NO_3$	Ref.
A'	ν_1	O–H stretch	E_v	2621.5	(32)	3550.0	(32)	3550.0	(32)
	ν_2	NO$_2$ a-stretch	E_v	1688.3629	(33)	1709.567	(4)	1675.4	(32)
	ν_3	NO$_2$ s-stretch	E_v	1308.5	(32)	1326.185	(4)	1327.0	(32)
	ν_4	H–ON bend	E_v	1013.22	(32)	1303.069	(4)	1320.6	(32)
	ν_5	NO$_2$ bend (planar)	E_v	887.658	(34)	886.229	(7)	875.050	(8)
		NO$_2$ bend (planar)	$\widetilde{\nu}$	887.658	(34)	879.1075		871.086	(8)
	ν_6	O–NO$_2$ stretch	E_v	642.1383	(35)	646.826	(4)	646.96407	(36)
	ν_7	O–NO$_2$ bend	E_v	541.5847	(35)	580.304	(4)	578.47191	(36)
A"	ν_8	NO$_2$ bend (out of plane)	E_v	762.8738	(37)	763.154	(4)	743.61660	(36)
	ν_9	H–ONO torsion	E_v	343.8496	(38)	458.229	(4)	458.29167	(36)
A'	$2\nu_9$	Overtone of ν_9:	E_v	677.5827	(38)	886.229	(7)	889.498	(8)
			$\widetilde{\nu}$	677.5827	(38)	896.447		893.452	
A"	$\nu_7+\nu_9$	Combination of ν_7 and ν_9	E_v	882.21	(34)	1038	(39)	~ 1037	(estimation)

Table II.2 Vibrational modes of several nitric acid isotopologues. The E_v and $\widetilde{\nu}$ are the vibrational energy and the band center, respectively, expressed in cm^{-1}. $\widetilde{\nu}$ is the calculated position for the [J=0, K_a=0, K_c=0] energy level.

Table II.2 gives the description, the frequency, and the symmetry type according to C_s of the nine vibrational modes of the $D^{14}NO_3$, $H^{14}NO_3$ and $H^{15}NO_3$ isotopologs. The C_s point group will be defined later in the text.

At zeroth-order, the rotation and vibration are well separated as shown previously ($H_0 = H_0^{vib} + H_0^{rot}$). The eigenstates of H_0 are the product of vibrational eigenstate of H_0^{vib} denoted as $\left|v_1 \, v_2 \, \dots \, v_9\right\rangle_0$ and of the rotational eigenstate of H_0^{rot}, denoted as $\left|J \, K_a \, K_c\right\rangle_0$:

$$\left|v_1 \, v_2 \, \dots \, v_9 \, J \, K_a \, K_c\right\rangle_0 = \left|v_1 \, v_2 \, \dots \, v_9\right\rangle_0 \left|J \, K_a \, K_c\right\rangle_0 \qquad (\text{II.25})$$

The zeroth-order vibrational Hamiltonian, H_0^{vib}, is a tensorial product of nine non degenerated harmonic oscillators. Each corresponding vibrational eigenstate, $\left|v_1 \, v_2 \, \dots \, v_9\right\rangle_0$ is the product of nine $\left|v_i\right\rangle$ harmonic oscillators eigenstates. Each associated eigenvalue is the sum of the nine associated eigenvalues:

$$E_0^{vib} = \omega_1 \left(v_1 + \frac{1}{2}\right) + \omega_2 \left(v_2 + \frac{1}{2}\right) + \dots + \omega_9 \left(v_9 + \frac{1}{2}\right) \qquad (\text{II.26})$$

II.2.2 Symmetry properties

II.2.2.1 Symmetry group of DNO_3

The equilibrium structure of nitric acid has two elements of symmetry: the identity E and the reflection in the molecular plane σ_{xz}. Therefore the appropriate symmetry point group is C_s with $C_s = \{E, \sigma\}$. This point group is isomorph to the $G_2 = \{E, E^*\}$, where E^* is the inversion of the positions of all particles (electron and atomic nuclei) in the center of mass.

Table II.3 presents the characters of the C_s group together with the symmetry species of the molecular (μ_x, μ_y, μ_z) and space-fixed (μ_Z) electric dipole moment components, of the total angular moment **J** molecular components, of the normal coordinates, and the rotational levels with regards to the K_c parity.

C_s G_2	E E	σ_{xz} E^*		μ	J		Vibrations	$[J \, K_a \, K_c]$ parity of K_c
A'	1	1		$\mu_x \; \mu_y$	J_z		$q_1, \dots, q_7$	even
A"	1	-1		μ_z , μ_Z	$J_x \; J_y$		q_8, q_9	odd

Table II.3 Symmetry properties of DNO_3 molecule

Let us remind that for the $H^{14}N^{16}O_3$ and $H^{15}N^{16}O_3$ isotopomers, the v_9 mode (H–ONO torsion around the $-N\!<^O_O$ group) is a large amplitude motion. This means that for excited energy levels in the v_9 vibrational quantum numbers, splittings of the energy levels can be observed, whose values are of about 2 MHz for $v_9 = 1$, 60 MHz for $v_9 = 2$ and 1800 MHz for $v_9 = 3$. This is because the v_9 large amplitude motion enables the $^O_O\!>N-O_H \quad \Leftrightarrow \quad ^O_O\!>N-O^H$

tunneling effects. In this operation, the two ^{16}O in the $-N\!<^O_O$ radical are exchanged through a (12) permutation. The C_s or G_2 groups are no more suitable, and it is necessary to use the $G_4 = \{E, (12), E^*, (12)^*\}$ permutation-inversion group to characterize the symmetry properties of the vibration- torsion- rotation wavefunctions. Of course G_4 is homomorph onto G_2 or C_s.

For DNO_3 such large amplitude motions are expected to be significantly weaker than for HNO_3 because of the mass ratio D/H~2. For example the tunneling splitting in the $v_9 = 2$ vibrational state of DNO_3 is expected to be only of 2 MHz, instead of 60 MHz for HNO_3. Therefore, the D-O tunneling around the $-N\!<^O_O$ moiety will not be considered for this DNO_3 study.

II.2.2.2 Symmetry properties of H_0 eigenstates

The eigenstates of H_0 can also be classified using the two irreducible representations of C_s group, their type of symmetry Γ (Γ = A' or A") depends on the parity of the rotational and vibrational quantum numbers and is obtained by multiplication of the types of symmetry of the vibrational state and of the rotational level:

$$\Gamma\left(\left|v_1\ v_2\ ...\ v_9\ J\ K_a\ K_c\right\rangle_0\right) = \Gamma\left(\left|v_1\ v_2\ ...\ v_9\right\rangle_0\right) \otimes \Gamma\left(\left|J\ K_a\ K_c\right\rangle_0\right) \tag{II.27}$$

Afterwards, it is convenient to calculate the matrix elements of the operators involved in the Hamiltonian using a symmetry adapted basis defined from the $\left|J\ k\right\rangle$ and $\left|v_1\ v_2\ ...\ v_9\right\rangle_0$.

II.2.2.2.1 Symmetry of vibrational states

The C_s symmetry group is an Abelian group and the type of symmetry of a particular vibrational state $\left|v_1\ v_2\ ...\ v_9\right\rangle$ is therefore given by the direct product of the types of symmetry of its each vibrational state $\left|v_i\right\rangle$:

$$\Gamma\left(\left|v_1\ v_2\ \dots\ v_9\right\rangle\right)=\Gamma\left(\left|v_1\ \right\rangle\right)\otimes\Gamma\left(\left|\ v_2\right\rangle\right)\otimes\dots\otimes\Gamma\left(\left|v_9\right\rangle\right) \tag{II.28}$$

The eigenfunctions of an one dimension harmonic oscillator $\left|v_i\right\rangle$, are Hermite's polynomes, $H_v(q_i)$. During the $q_i \rightarrow -q_i$ change of sign, the $\left|v_i\right\rangle$ wavefunction changes as:

$$q_i \rightarrow \text{-}q_i \qquad H_{v_i}(q_i) \rightarrow H_{v_i}(-q_i) = (-1)^{v_i}\, H_{v_i}(q_i). \tag{II.29}$$

The symmetry type of the $\left|v_i\right\rangle$ vibrational wave function according to C_s depends on the i and v_i values. For i = 1 to 7, the q_i normal mode does not change during any C_s symmetry operation (E or σ_{xz}). Consequently, $\Gamma\left(\left|v_i\right\rangle\right) = A'$ for i = 1 to 7 and for all v_i values. On the other hand, for i = 8 or 9, $\Gamma\left(\left|v_i\right\rangle\right) = A'$ and $\Gamma\left(\left|v_i\right\rangle\right) = A''$ for v_i even and v_i odd, respectively. Therefore, for nitric acid, the $\left|v_1\ v_2\ \dots\ v_9\right\rangle$ vibrational states with even v_8+v_9 values (resp. odd v_8+v_9 values) are of A' symmetry (resp. of A" symmetry):

$$\Gamma\left(\left|v_1\ v_2\ \dots\ v_9\right\rangle\right) = A'\ (\text{resp. A''})\ \text{if}\ (v_8 + v_9) = \text{even (resp.}\ (v_8 + v_9) = \text{odd)} \tag{II.30}$$

Symmetry of rotational levels

The inertia ellipsoid has at least three planes of symmetry and three binary axes, whatever the molecular symmetry group is. The molecular rotation Hamiltonian is therefore invariant under any operation of the V symmetry group (Vierergruppe, noted also D_2): identity, three rotations by π around the respective axes x, y and z. The symmetry types of the rotational levels in this group are hence to be determined. The characters of the V symmetry group are given in Table II.4.

V (D_2)	E	C_x^2	C_y^2	C_z^2
A	1	1	1	1
B_x	1	1	-1	-1
B_y	1	-1	1	-1
B_z	1	-1	-1	1

Table II.4 Character table of the V group of symmetry

As was already mentioned, the eigenstates of H_0^{rot} are determined through diagonalization of this Hamiltonian in a standard basis $\left|J\ k\right\rangle$, and the wavefunctions $\left|J\ K_a\ K_c\right\rangle_0$ are given as

linear combinations of $|J\ k\rangle$ basis sets. In order to determine the symmetry of the $|J\ K_a\ K_c\rangle_0$ levels it is necessary to determine the symmetry of the $|J\ k\rangle$ functions.

An appropriate symmetric basis of rotational wavefunctions is the Wang type basis defined as:

$$|J\ K\ \gamma\rangle = \frac{1}{\sqrt{2}}\left(|J\ k\rangle + \gamma|J\ -k\rangle\right)$$
(II.31)

with $K = |k|,\ \gamma = \pm 1$

and

$$|J\ 0\ \gamma = +1\rangle = |J\ 0\rangle$$
(II.32)

The $|J\ K\ \gamma\rangle$ are grouped in four classes named usually E$_+$, E$_-$, O$_+$ and O$_-$ with regards to the K parity (K even or odd) and the γ sign ($\gamma = \pm 1$).

The following useful relations were demonstrated (*40*):

$$R_z^\beta|J\ k\rangle = \exp\left(i\ k\ \beta\right)|J\ k\rangle$$
(II.33)

$$R_\alpha^\pi|J\ k\rangle = (-1)^J \exp\left(-2\ i\ k\ \alpha\right)|J\ -k\rangle$$
(II.34)

In this expression R_z^β is the rotation of a β angle around z of the x and y axes. Also, R_α^π is the π rotation of the x, y and z axes around an "α" axis. This "α" axis is located in the (xy) plane with an α angle with regards to the x axis.

The three rotation operations of the group V (C_x^2, C_y^2, C_z^2) are equivalent to the $R_0^\pi, R_{\pi/2}^\pi, R_z^\pi$ operations, respectively. The equations (II.33-34) give the $|J\ K\ \gamma\rangle$ symmetry types under the V operations. The irreducible representation of this group under the I^r convention ($x = b$, $y = c$, $z = a$) is:

A $\rightarrow$ A, B$_x$ $\rightarrow$ B$_b$, B$_y$ $\rightarrow$ B$_c$, B$_z$ $\rightarrow$ B$_a$
(II.35)

Table II.5 gives the symmetry of the basis functions $|J\ K\ \gamma\rangle$ under the V symmetry group following the I^r convention.

	J even	*J* odd
E_+	A	B_a
E_-	B_a	A
O_+	B_b	B_c
O_-	B_c	B_b

Table II.5 Symmetry of fonctions $\left| J \ K \ \gamma \right\rangle$ **under the V group of symmetry**

Under the under the I^r convention, the $\left| J \ K_a \ K_c \right\rangle_0$ symmetry types according to V operation are deduced from those of $\left| J \ K \ \gamma \right\rangle$ in the two limit cases, $K \rightarrow K_a$ and $K \rightarrow K_c$. This is possible since the levels sharing the same *J* do not cross each other and the symmetry properties are conserved. As a final result, the symmetry type of $\left| J \ K_a \ K_c \right\rangle_0$ depends only on the K_a and K_c parity, as reported in the Table II.6.

K_a	K_c	type
e	e	A
e	o	B_a
o	o	B_b
o	e	B_c

Table II.6 Symmetry of the rotational levels under the V symmetry group

Once the symmetry types of the $\left| J \ K_a \ K_c \right\rangle_0$ and $\left| J \ K \ \gamma \right\rangle$ wavefunction relative to V are established, it is easy to set the symmetry properties of these wavefunctions relative to the C_s point group. Indeed V is homomorph onto G_2 or C_s.

Therefore, the correspondence between the irreductible representations of the V and C_s group is obtained:

$$V \rightarrow C_s; \quad A, B_y \ \rightarrow \ A'; \quad B_a, B_b \ \rightarrow \ A'' \tag{II.36}$$

The symmetry of the $\left| J \ K_a \ K_c \right\rangle_0$ levels and of the basis functions $\left| J \ K \ \gamma \right\rangle$ under the C_s symmetry group is given in Tables II.7-8.

	J even	J odd
E+	A'	A"
E-	A"	A'
O+	A"	A'
O-	A'	A"

Table II.7 Symmetry of the levels $\left| J \ K \ \gamma \right\rangle$ **under** C_s **symmetry group**

	$J\,K_a\,K_c$
K_c even	A'
K_c odd	A"

Table II.8 Symmetry of the levels $\left| J \ K_a \ K_c \right\rangle_0$ **under** C_s **symmetry group**

II.2.2.2.2 Symmetry of the rovibrational levels

The symmetry of the H_0 eigenstates can be determined using the equation (II.29) from the known symmetry of the H_0^{vib} and H_0^{rot} eigenstates and depends only on the K_c and (v_8+v_9) parities, as is shown in Table II.9.

		K_c even	K_c odd
$\Gamma\left(\left| v_1 \ v_2 \ \ldots \ v_9 \ J \ K_a \ K_c \right\rangle_0 \right)$	(v_8+v_9) = even	A'	A"
	(v_8+v_9) = odd	A"	A'

Table II.9 Symmetry of rovibrational levels of DNO$_3$ under C_s **symmetry group**

II.2.3 Selection rules

The intensity of an electric dipole moment transition between two levels $\left| v_1' \ v_2' \ \ldots \ v_9' \ J' \ K_a' \ K_c' \right\rangle$ and $\left| v_1" \ v_2" \ \ldots \ v_9" \ J" \ K_a" \ K_c" \right\rangle$ is proportional to the square of the transition moment matrix element:

$$\left| \left\langle v_1' \ v_2' \ \ldots \ v_9' \ J' \ K_a' \ K_c' \left| \mu_Z \right| v_1" \ v_2" \ \ldots \ v_9" \ J" \ K_a" \ K_c" \right\rangle \right|^2 \tag{II.37}$$

where μ_Z is the component on the laboratory axis Z of the molecule electric dipole moment $\boldsymbol{\mu}$. In order this matrix element be non-zero, the following conditions must be satisfied:

- For an electric dipolar transition, one has:

$$\Delta J = 0, \ \pm 1 \tag{II.38}$$

- The transition moment matrix element must belong to the totally symmetric representation of the molecular symmetry group. For a C_s type molecule this is stated by:

$$\Gamma\left(\left|v_1' \ v_2' \ \dots \ v_9' \ J' \ K_a' \ K_c'\right\rangle\right) \otimes \Gamma\left(\left|\mu_z\right\rangle\right) \otimes \Gamma\left(\left|v_1'' \ v_2'' \ \dots \ v_9'' \ J'' \ K_a'' \ K_c''\right\rangle\right) = A' \tag{II.39}$$

Following Table II.3, $\Gamma\left(\left|\mu_z\right\rangle\right) = A''$, and in order to satisfy the equation (II.39), the following relation must hold:

$$\Gamma\left(\left|v_1' \ v_2' \ \dots \ v_9' \ J' \ K_a' \ K_c'\right\rangle\right) \otimes \Gamma\left(\left|v_1'' \ v_2'' \ \dots \ v_9'' \ J'' \ K_a'' \ K_c''\right\rangle\right) = A'' \tag{II.40}$$

The symmetry types of the vibration − rotational wavefunctions are gathered in Table II.9. Using these results, it is easy to deduce the $\Delta K_a = |K_a' - K_a''|$ and $\Delta K_c = |K_c' - K_c''|$ selection rules as a function of the $\Delta(v_8+v_9)$ variation. These results are collected in Table II.10. Let us remind that the v_5 and v_7+v_9 bands of DNO$_3$ bands correspond to $\Delta(v_8+v_9) = 0$ and $\Delta(v_8+v_9) = 1$, respectively.

$\Delta\lvert v_8 + v_9 \rvert$ = odd (v_7+v_9 band)	$\Delta\lvert v_8 + v_9 \rvert$ = even (v_5 band)	
C-type transitions	A-type transitions	B-type transitions
$\lvert\Delta K_a\rvert = odd$ $\lvert\Delta K_c\rvert = even$	$\lvert\Delta K_a\rvert = even$ $\lvert\Delta K_c\rvert = odd$	$\lvert\Delta K_a\rvert = odd$ $\lvert\Delta K_c\rvert = odd$

Table II.10 Selection rules for an electric dipole moment transition

For vibrational transitions with $\Delta(v_8+v_9) = $ even, the band is in principle hybrid, with both A- and B-type characters. This is the case, in principle for the v_2 to v_7 fundamental bands of H^{14}NO$_3$ or DNO$_3$. For example, during the analysis of the v_4 band of H^{14}NO$_3$, both A and B type vibro-rotational transitions were observed (41).

It is important to underline that for a hybrid band the A to B character depends on the relative values of the a to b components of the transition moment operator of the considered band. Indeed, for H^{14}NO$_3$, H^{15}NO$_3$ and DNO$_3$, the v_2 bands are almost pure B-type bands, while v_3, v_6 and v_7 are mostly A-type bands. This is obvious when comparing the general structure of the v_6 to v_2 bands of nitric acid (Figs II.2 and II.3, respectively). Finally the v_5 band is a pure

A-type band for $H^{14}NO_3$ and $H^{15}NO_3$, and is hybrid for DNO_3 with a significantly stronger A-type component as compared to its B-type counterpart.
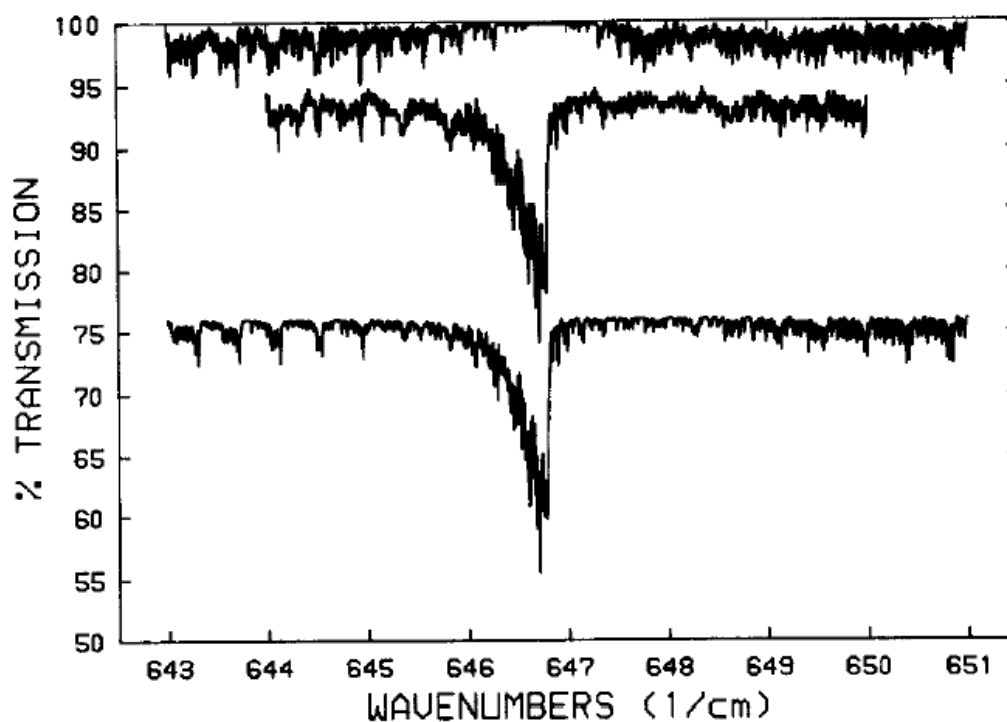
Fig. II.2 Calculated and observed spectrum of the ν_6 Q branch of HNO_3 (*42*). The upper curve is the calculated spectrum for only b-type transitions; the middle curve is the observed spectrum; and the lower curve is the calculated spectrum for only A-type transitions. The spectra are offset for clarity.
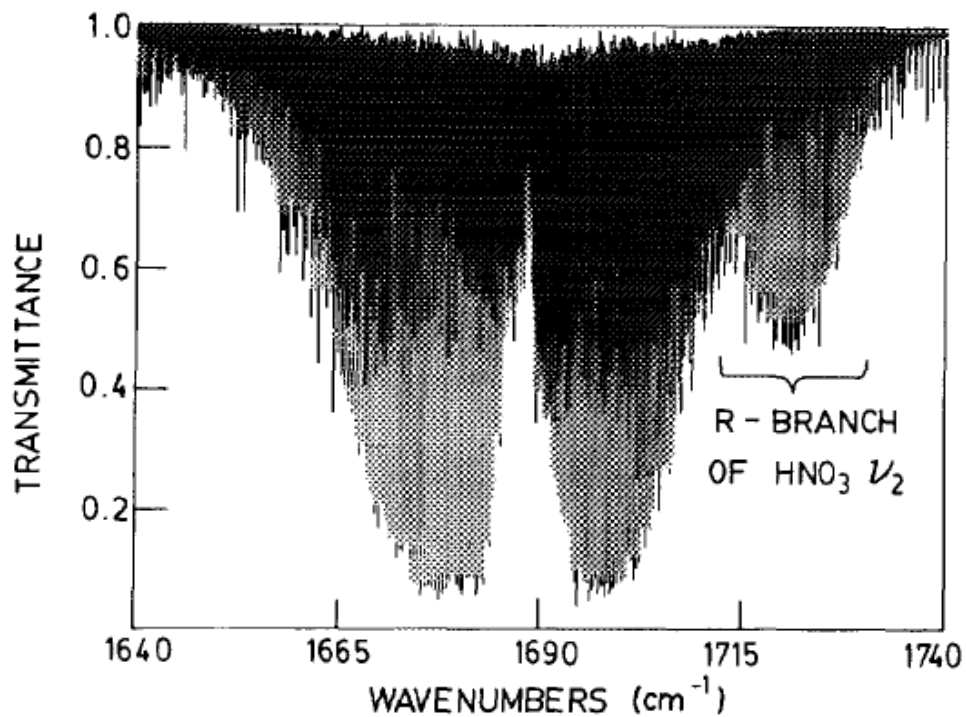
Fig. II.3 Overview of the ν_2 band of DNO$_3$ and HNO$_3$ for an D-enriched sample of nitric acid. The absence of sharp Q structure indicates a B-type character of the ν_2 band. From Ref. (*33*).
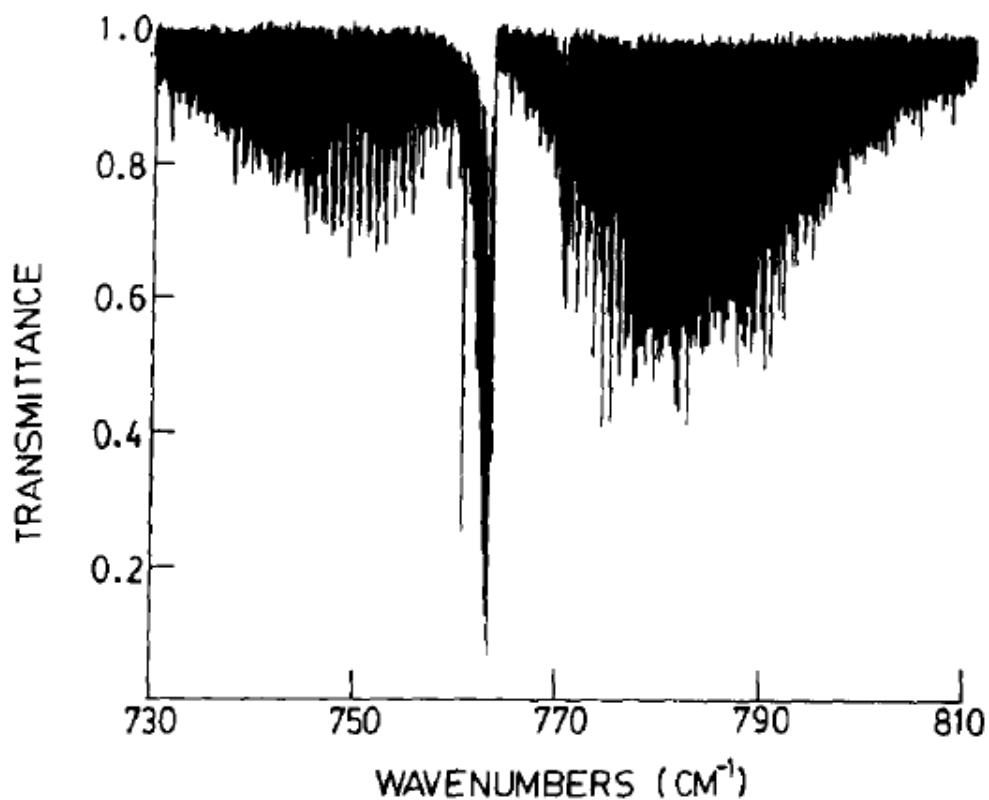
Fig. II.4 Overview of the C-type ν_8 band of DNO$_3$. From Ref. (*37*).

Finally, Fig. II.4 gives an overview of the C-type ν_8 band of DNO_3: it is clear that C-type bands differ in its structure from A- or B-type bands (see Figs. II.2-3).

II.2.4 Contact transformation and energy levels calculation

It is possible, in principle, to compute the rotation-vibration energy levels of a given molecule together with its associated transition intensities. For this it is necessary to build a potential energy surface generated through ab initio calculations and subsequently fitted against experimental data. Such studies are presently performed for water (*43*), methane (*44*), ozone (*45*), phosphine (*46*). These calculations necessitate important computation capacities and a large set of accurate experimental data to validate the results of the calculations. Even in this case, the accuracy of the calculation is often far from the experiment.

Such theoretical methods are far for being applicable for nitric acid at the present time. Nitric acid with five atoms, several N-O bonds and the existence of the large amplitude OH bonds is quite a challenge for ab initio calculations (*11*). In addition the experimental data are still scarce. To give an example, the ν_1 fundamental band at 3 μm was not yet investigated at high resolution. Finally, in the literature, the infrared studies pointed out the existence of numerous complicated resonances.

For this reason it is not possible to perform a full diagonalisation of the vibration- rotation Hamiltonian. To perform the analyses presented here, it is necessary to use effective Hamiltonians which were generated through the so called contact transformations which are described here.

II.2.4.1 Vibrational Hamiltonian

A widely used perturbation method in molecular spectroscopy is the unitary transformation method first proposed by Van Vleck (*47*) and developed further in Refs. (*48-50*). This method leads to a partial vibrational diagonalization of the Hamiltonian matrix in vibrational blocks and is based on the physical properties of the molecule. Each vibrational block groups together vibrational states with close enough vibrational energies. These states are presumed to interact together, while interactions between states belonging to different blocks are assumed to be much weaker. The goal of the contact transformation method is to

eliminate, at a given order of approximation, the matrix elements coupling the states that do not belong to the same polyad.

For instance, let the Hamiltonian H be developed:

$$H = H_0 + H_1 + H_2 + \ldots + H_p + \ldots \tag{II.41}$$

The first contact transformation T_1 leads to:

$$\begin{aligned} H' &= T_1\ H\ T_1^{-1} \\ &= H_0' + H_1' + H_2' + \ldots + H_p' + \ldots \end{aligned} \tag{II.42}$$

T_1 is chosen such that $H_0' = H_0$ applies and H_1' is block diagonal in the basis $\left| v_1\ v_2\ \ldots\ v_9 \right\rangle$ following the scheme of resonance.

A second contact transformation T_2 leads to:

$$\begin{aligned} H'' &= T_2\ H\ T_2^{-1} \\ &= H_0'' + H_1'' + H_2'' + \ldots + H_p'' + \ldots \end{aligned} \tag{II.43}$$

T_2 is chosen such that $H_0'' = H_0' = H_0$ and $H_1'' = H_1'$ apply and H_1'' is block diagonal in the basis $\left| v_1\ v_2\ \ldots\ v_9 \right\rangle$ following the scheme of resonance.

The contact transformation may be repeated, in principle, until the elimination, in sufficient order of approximation, of all operators coupling states belonging to different polyads. The Hamiltonian matrix appears then in a bloc diagonal form following a chosen resonance scheme. This simplifies the Hamiltonian matrix diagonalization because it is sufficient to calculate individually each block related to the particular polyad of interacting states.

However, as it is detailed in Ref. (*51*), it is important to underline that this method is suitable only if several conditions are fulfilled.

The T_i ($i = 1, 2, \ldots$) unitary operators are usually written as $T_i = \exp(S_i)$. The vibration (and or) rotational operators, S_i, must obey the following conditions.

- as it is the case for H_i, the S_i operators must fulfill strict symmetry conditions for all the terms appearing at a given order in the expansion of the T expansion.

- There exist also severe criteria of convergence, both for the H_i and S_i operators appearing in the expansion of the Hamiltonian and of T, respectively.

More or less, and without going into details, one must have:

$$H_{i+1}/H_i \approx \eta \text{ and } S_{i+1}/S_i \approx \eta \text{ with of course } \eta{<}{<}1 \tag{II.44}$$

with depending on the authors, different definitions for η. One is based on the Born-Oppenheimer parameter $\eta = \left(m_e \middle/ m_p\right)^{1/4}$ where m_e and m_p are the electron and proton masses, respectively, the other one adopted by Nielsen (52) is $\eta = \left(B\middle/\omega\right)^{1/2}$, where B and ω are mean values of the rotational constants and vibrational frequencies, respectively.

II.2.4.2 Rotational Hamiltonian for non resonating states

Two cases are discerned: isolated vibrational state and polyad of interacting states.

Let us consider the Hamiltonian H^{T} obtained by a series of contact transformations and an isolated (non resonating) state $|v\rangle$. The relevant part $\mathscr{H}^{\mathrm{T}}$ of the transformed Hamiltonian H^{T} is:

$$\begin{aligned}\mathscr{H}^{\mathrm{T}} &= |v\rangle\langle v|H^{\mathrm{T}}|v\rangle\langle v| \\ &= |v\rangle H_{vv}\langle v|\end{aligned} \tag{II.45}$$

In the vibrational state v, $H_{vv} = E_v + H_v^{rot}$ contains only the operators acting on rotational functions, i.e. the powers of operators $J_\alpha (\alpha = x, y, z)$ and can be written as:

$$H_{vv} = E_v + H_v^{rot}, \tag{II.46}$$

Where E_v is vibrational energy dependent on v and coinciding with the band center, in this case of non resonating state. H_v^{rot} is the rotational Hamiltonian of the state v which can be written in general form proposed by J.K.G. Watson (29, 53-55, 56) as:

$$H_v^{rot} = \sum_{pqr} h_v^{pqr}\left(J_x^p J_y^q J_z^r + J_z^r J_y^q J_x^p\right), \; h_v^{pqr} \in \mathbb{R}, \; p+q+r \in 2\mathbb{N} \tag{II.47}$$

This expansion of H_v^{rot} is written with strict conditions for the existing non zero h_v^{pqr} parameters and for the p, q and r exponents values which can appear at a given n order ($p + q + r = n$). Indeed, H_v^{rot} must be fully symmetrical in the molecular symmetry group, and remain unchanged during other symmetry operations (time reversal, exchange of the particules etc…).

The direct diagonalization of H_{vv} gives the energy levels if the h_v^{pqr} coefficients are known. The inverse problem consists in the determination of the h_v^{pqr} coefficients from the observed eigenvalues which are the experimental energy levels. As J.K.G. Watson showed all the h_v^{pqr} coefficients cannot be determined simultaneously from the experimental energy levels. The method proposed by J.K.G. Watson consists in performing a series of rotational contact transformations. These unitary transformations do not change the eigenvalues of a given rotational Hamiltonian and eliminate the undeterminable parameters at a given order. The used unitary operator is e^{iS_v} where S_v is a rotational operator that can be expanded as a series with respect to the components of $\mathbf{J}$:

$$S_v = \sum_{pqr} s_v^{pqr} \left(J_x^p J_y^q J_z^r + J_z^r J_y^q J_x^p \right), \ s_v^{pqr} \in \mathbb{R}, p + q + r \in 2\mathbb{N} \qquad (\text{II.48})$$

There are multiple ways of reduction to go from H_v^{rot} to $H_v^{red} = e^{iS_v} H_v^{rot} e^{-iS_v}$ (J.K.G. Watson (*53*)).

Case of an orthorhombic molecule:

Orthorhombic molecule are molecules for which the symmetry point group is isomorph to V (C_{2v}, D_2 etc..) or homomorph into V (D_{2V} etc..). For this type of molecules several types of reductions exist, among which Watson described in detail the *A* and *S* type reductions.

We will only consider here the *A* reduction, where H_v^{red} has non zero matrix elements only for $\Delta K = 0, \pm 2$. In this way, the rotational Hamiltonian is written as:

$$H_v^{red} = H_{(2)} + H_{(4)} + H_{(6)} + \dots, \qquad (\text{II.49})$$

with

$$H_{(2)} = \left(A_\mathrm{v} - \frac{1}{2}(B_\mathrm{v} + C_\mathrm{v}) J_z^2 \right) + \frac{1}{2}(B_\mathrm{v} + C_\mathrm{v}) \mathbf{J}^2 + \frac{1}{2}(B_\mathrm{v} - C_\mathrm{v}) J_{xy}^2 \qquad \text{(II.50)}$$

$$\begin{aligned}
H_{(4)} = & -\Delta_K^\mathrm{v} J_z^4 - \Delta_{JK}^\mathrm{v} J_z^2 \mathbf{J}^2 - \Delta_J^\mathrm{v} \left(\mathbf{J}^2 \right)^2 \\
& - \delta_K^\mathrm{v} \left\{ J_z^2, J_{xy}^2 \right\} - 2\delta_J^\mathrm{v} J_{xy}^2 \mathbf{J}^2
\end{aligned} \qquad \text{(II.51)}$$

$$\begin{aligned}
H_{(6)} = & H_K^\mathrm{v} J_z^6 + H_{KJ}^\mathrm{v} J_z^4 \mathbf{J}^2 + H_{JK}^\mathrm{v} J_z^2 \left(\mathbf{J}^2 \right)^2 + H_J^\mathrm{v} \left(\mathbf{J}^2 \right)^3 \\
& + h_K^\mathrm{v} \left\{ J_z^4, J_{xy}^2 \right\} + h_{KJ}^\mathrm{v} \left\{ J_z^2, J_{xy}^2 \right\} \mathbf{J}^2 + 2h_J^\mathrm{v} J_{xy}^2 \left(\mathbf{J}^2 \right)^{2}{}^{,}
\end{aligned} \qquad \text{(II.52)}$$

where

$$J_{xy}^2 = J_x^2 - J_y^2, \quad \{A, B\} = AB + BA . \qquad \text{(II.53)}$$

Case of a C_s type molecule:

We are dealing here with DNO_3 which is not an orthorhombic molecule. At the second order its rotational Hamiltonian takes a form which is more complicated than for a V molecule:

$$H_{(2)}^{Non\,Red} = A_\mathrm{v} J_z^2 + B_\mathrm{v} J_z^2 + C_\mathrm{v} J_z^2 + h_{xz}^\mathrm{v} \{J_x, J_z\} \qquad \text{(II.54)}$$

In this expression the $\{J_x, J_z\}$ is a non-orthorhombic term. However, Watson has demonstrated that, in principle, it is possible to remove all the non-orthorhombic terms (in $h_{xz}^\mathrm{v} \{J_x, J_z\}$ for example) by a suitable contact transformation. For this reason the form of the reduced rotational Hamiltonian written in Eqs. (II.50-53) can be used for a C_s type molecule for DNO_3.

In the present study, the rotational Hamiltonian that was used for DNO_3 was written in the A reduction and with a I^r representation. Indeed the same model was successfully used recently during the ground state studies performed for HNO_3 and DNO_3 ((*30, 31*) and Refs. therein).

II.2.4.3 Resonance conditions

As was suggested previously, interactions can couple energy levels belonging to different vibrational states with rather close energy. These resonances must be taken into account explicitly.

Let us consider two states $|v_1\rangle$, $|v_2\rangle$ with energies $E_{v_1}^0$, $E_{v_2}^0$. If an interaction X is considered, the second order corrections to the energies are: $\dfrac{\langle v_1|X|v_2\rangle}{E_{v_2}^0 - E_{v_1}^0}$. If this correction is small when compared to 1, the problem can be solved by perturbation methods. If $E_{v_2}^0 - E_{v_1}^0$ is of the same order as $\langle v_1|X|v_2\rangle$, the two states in question are in resonance.

In order that the $\langle v_1|X|v_2\rangle$ matrix element differs from zero, several conditions must be fulfilled:

$$\Gamma(v_1)\otimes\Gamma(X)\otimes\Gamma(v_2)=A' \qquad\qquad\qquad\text{(II.55)}$$

$\left[H,\mathbf{J}^2\right]=0$, and therefore

$$\left[X,\mathbf{J}^2\right]=0. \qquad\qquad\qquad\text{(II.56)}$$

The resonance conditions for states therefore are:

- same value of J quantum number

- same type of symmetry

- close energy levels

II.2.4.4 Rotational operators appearing in the expansion of the v-off diagonal operators in case of resonances

When several vibrational state have to be considered in the same block of interacting states, the relevant part $\mathscr{H}^\mathrm{T}$ of the transformed Hamiltonian H^T has the following general form:

$$\mathcal{H}^{\mathrm{T}} = \sum_{\mathrm{v\,v'}} |\mathrm{v}\rangle \langle \mathrm{v}|H^{\mathrm{T}}|\mathrm{v'}\rangle \langle \mathrm{v'}|$$
$$= \sum_{\mathrm{v\,v'}} |\mathrm{v}\rangle H_{\mathrm{vv'}} \langle \mathrm{v'}| \qquad\qquad\qquad\qquad \text{(II.57)}$$

with $H_{\mathrm{vv'}} = \langle \mathrm{v}|H^{\mathrm{T}}|\mathrm{v'}\rangle$ \qquad\qquad\qquad\qquad\qquad (II.58)

where v and v' represent vibrational states belonging to the same polyad.

¤ v diagonal blocks

When v = v', it is possible, in principle, to apply the results of the previous discussion. By performing rotational contact transformation the v- diagonal H_{vv} Hamiltonian is reduced to the Hamiltonian H_{vv}^{red} that can be written as:

$$H_{\mathrm{vv}}^{red} = E^{\mathrm{v}} + H_{\mathrm{v}}^{red} \qquad\qquad\qquad\qquad\qquad \text{(II.59)}$$

where the operator, H_{v}^{red} takes the form given in Eqs. (II.50-52). One defines the vibrational band center $\widetilde{\nu}$ as the (fictive) position of the $[J = 0, K_a = 0, K_c = 0]$ energy levels. The vibrational level energy E^{v} does not always coincide with $\widetilde{\nu}$ especially when anharmonic interaction operators exist. This is particularly the case for the $\{5^1, 9^2\}$ system of interacting states for $H^{14}NO_3$ and $H^{15}NO_3$, as it can be seen in Table II.2.

¤ v ≠ v' off diagonal blocks.

When strong resonances couple energy levels from different vibrational states, it is necessary to account explicitly these interactions. The theoretical approach used to carry out the calculation of the resonating energy levels is described by J.-M. Flaud and C. Camy-Peyret (*57*). In this approach, the expansion of the rotational operators in the off diagonal blocks is written in an expansion based on symmetry considerations. The rotational terms are, in principle, expanded according to their **J** power.

Indeed for a molecule with symmetry C_s like DNO_3, the $H_{\mathrm{v\,v'}}$ rotational operator belongs to A' the totally symmetric representation of the group. Following expressions apply for the non diagonal operators of $H_{\mathrm{vv'}}$:

$$\Gamma\left(H_{\mathrm{vv'}}\right) \otimes \Gamma\left(|\mathrm{v}\rangle\right) \otimes \Gamma\left(|\mathrm{v'}\rangle\right) = \mathsf{A'} \qquad\qquad\qquad \text{(II.60)}$$

The form of the $H_{vv'}$ rotational operator for $|v\rangle$ and $|v'\rangle$ interacting vibrational states depends on the $\Delta(v_8+v_9)$ variation, more explicitly:

¤ $\Delta(v_8+v_9)$ = even, $H_{vv'}$ = anharmonic and Fermi- type rotational operators together with C-type Coriolis operators

¤ $\Delta(v_8+v_9)$ = odd, $H_{vv'}$ = A- and B-type Coriolis operators.

Table II.11 gives the type of rotational operators which appears in the expansion of the off diagonal in v rotational operators (up to n = 2).

$\Delta(v_8+v_9)$ = even	Fermi or anharmonic		C-type Coriolis	
	n = 0	n = 2	n = 1	n = 2
A' rotational operators:	Cst	$\mathbf{J}^2 , J_z^2 , \left(J_x^2 - J_z^2\right)$	iJ_y	$\left\{J_x, J_z\right\}$
$\Delta(v_8+v_9)$ = odd	A-type Coriolis		B-type Coriolis	
	n = 1	n = 2	n = 1	n = 2
A" rotational operators:	J_z	$\left\{J_x, iJ_y\right\}$	J_x	$\left\{J_z, iJ_y\right\}$

Table II.11 Type of rotational operators appearing in the expansion of the v- off diagonal resonating blocks as a function of $\Delta(v_8+v_9)$.

If we consider the dyad $\{5^1, 7^1+9^1\}$ of DNO$_3$, with 5^1 and 7^1+9^1 of A' and A" symmetry, respectively, all operators appearing in the expansion of the $H_{vv'}$ off diagonal interaction block are of A- or B- Coriolis types and must be of A" symmetry.

On the other hand, for the dyad $\{5^1, 9^2\}$ of HNO$_3$, Fermi and C-type Coriolis resonances couple together the 5^1, and 9^2 energy levels of H^{14}NO$_3$ (7) and H^{15}NO$_3$ (8).

Finally, let us mention that in the expansion of the interacting operators, the terms in $\mathbf{J}^1$ (J_x, iJ_y and J_z for an B–type, C-type or A-type Coriolis resonances), are usually, but not always weaker but than those in $\mathbf{J}^2$ ($\{iJ_y,J_z\}$, $\{J_x,J_z\}$, or $\{J_x,iJ_y\}$, respectively). This was discussed in details by Perevalov and Tyuterev in 1982 (58), considering the rotational constants values, the strength of the resonance, and the distance between the interacting vibrational states.

II.2.4.5 Symmetrized basis for energy level calculation

The expansion of $\left| v_1\ v_2\ \ldots\ v_9\ J\ K_a\ K_c \right\rangle$ wavefunctions is performed on $\left| v \right\rangle \otimes \left| J\ K\ \gamma \right\rangle$ cross product of zero order vibration and rotation wavefunctions:

$$\left| v_1\ v_2\ \ldots\ v_9\ J\ K_a\ K_c\ \right\rangle_\Gamma = \sum_{v'} \sum_{K} C_K^{v'} \left| v' \right\rangle_{\Gamma_v} \left| J\ K\ \gamma \right\rangle_{\Gamma_{rot}} \tag{II.61}$$

with $\Gamma_v \otimes \Gamma_{rot} = \Gamma$ symmetry conditions. In this expression the sum over v' runs only through the states belonging to the same polyad of interacting states, B'. For the study performed during this thesis for DNO_3, B' = $\{5^1,\ 7^1+9^1\}$.

II.2.5 Intensities

The intensity of a line (*57*) for a "pure" isotopic sample of DNO_3 is given (in cm^{-1}/(molecule.cm^{-2})) by:

$$k_{\tilde{v}}^N = \frac{8\pi^3 \tilde{v}}{4\pi\varepsilon_0 3hc\ Z(T)} \left(1 - exp\left(-\frac{hc\tilde{v}}{kT}\right)\right) exp\left(-\frac{hcE_L}{kT}\right) R_L^U \tag{II.62}$$

where L and U are respectively the lower and upper levels of the transition, $\tilde{v} = \left(E_U - E_L\right)/\left(hc\right)$ is the wavenumber of the transition in cm^{-1}, $Z(T)$ is the total partition function and R_L^U is line strength.

The total partition function can be written as:

$$Z(T) = Z_{vib}(T) \cdot Z_{rot}(T) \tag{II.63}$$

and includes a vibrational contribution $Z_{vib}(T)$ and a rotational contribution $Z_{rot}(T)$.

Finally, R_L^U is the square of the matrix element:

$$R_L^U = \sum_l \sum_u \left| \left\langle l \left| \mathbf{\mu} \right| u \right\rangle \right|^2, \tag{II.64}$$

where $\left| l \right\rangle$ and $\left| u \right\rangle$ are the states corresponding to the degeneracy in quantum number M of the lower and upper level, and $\mathbf{\mu}$ is the transition moment operator.

In case of zero external field, the expression (II.64) simplifies in to

$$R_L^U = 3 \sum_l \sum_u \left| \langle l | \mu_Z | u \rangle \right|^2 , \tag{II.65}$$

where μ_Z is the projection of electric dipole moment on axis OZ of the laboratory system of axis.

Intensities are often given other units, and the following correspondence applies:

$$k_{\tilde{\nu}} = N \, k_{\tilde{\nu}}^N \quad \text{(in cm}^{-1}/\text{(cm}^{-2}\text{))} \tag{II.66}$$

$$k_{\tilde{\nu}}^P = \frac{k_{\tilde{\nu}}}{P} = L \frac{T_0}{T} k_{\tilde{\nu}}^N \quad \text{(in cm}^{-2}.\text{atm}^{-1}\text{)}, \tag{II.67}$$

where L is Loschmidt constant ($L = 2.686754 \ 10^{19}$ cm^{-3} at 0 °C and 1 atm), N is number of molecules and P is the pressure.

In Eq. (II.62) the quantity difficult to evaluate is R_L^U. Also, the initial upper and lower state Hamiltonian were transformed by rotational and vibrational contact transformations in order to enable the energy levels calculation. As a consequence, these contact transformations also affect the transition moment operator. Therefore, the transformed dipole moment, μ_Z', is used for the calculation of R_L^U :

$$R_L^U = \left| \langle \nu', J' K_a' K_c' | \mu_Z' | \nu'', J'' K_a'' K_c'' \rangle \right|^2 \tag{II.68}$$

It is, in principle possible to calculate explicitly the transformed dipole moment using the expression of the vibrational and rotational contact transformations. This was indeed performed numerically for several C_{2v} triatomic molecules (59). However, for molecules with five atoms, like DNO$_3$, this task is impossible. Therefore it is necessary to use an a priori expansion of the transformed transition moment operator based on the symmetry properties of the molecule.

II.2.5.1 Transformed dipolar moment

In the present study we are dealing only on cold bands, and the lower vibrational state is the ground state $(|0\rangle)$. The operator of the transformed dipole moment may be written as:

$$\mu_Z^{'} = \sum_v |0\rangle \; {}^{v,0}\mu_Z^{'} \langle v|, \tag{II.69}$$

where v runs through all members of the polyad B', and ${}^{v,0}\mu_Z^{'}$ is the transition moment between the ground state and the state v that can be written as:

$$^{v,0}\mu_Z^{'} = \sum_j {}^{v,0}\mu_j^{'} A_j , \tag{II.70}$$

where ${}^{v,0}\mu_j^{'}$ are the coefficients to be determined from the experimental intensities, and A_j are the rotational operators of the form $\left\{ J_x^p J_y^q J_z^r + J_z^r J_y^q J_x^p , \varphi_\alpha \right\}$. In this expression, φ_α is direction cosine between the molecular axes α and the laboratory axis Z. The operator $\mu_Z^{'}$ has the A" symmetry as μ_Z, therefore the A_j operators depends on symmetry properties of the vibrational operator $|0\rangle\langle v|$.

  ¤ For $\Delta(v_8+v_9)$ = even, both A- and B- type transitions are observable, and, up to the second order, the A_j operators appearing in the right hand side of Eq. (II.70) are in φ_z, $\{\varphi_x, iJ_y\}$, $\{i\varphi_y, J_x\}$, and in φ_x, $\{\varphi_z, iJ_y\}$, $\{i\varphi_y, J_z\}$, for the A- and B-type expansion, respectively.

  ¤ For $\Delta(v_8+v_9)$ = odd, only C- type transitions are observable. In this case Eq. (II.70) involves only terms in $i\varphi_y$, $\{\varphi_z, J_x\}$, $\{\varphi_x, J_z\}$.

II.2.5.2 Calculation of the line strengths:

The eigenvectors are written on the symmetrized basis functions as:

$$\left| v_1 \; v_2 \; \ldots \; v_9 \; J \; K_a \; K_c \; \right\rangle_0 = \sum_v \sum_{K,\gamma} C_{K,\gamma}^v |v\rangle |J \; K \; \gamma\rangle . \tag{II.71}$$

The expression (II.68) is now written in the following way:

$$R_L^U = \left| \sum_{v'} \sum_{K'} \sum_{K''} \sum_j C_{K'}^{v'*} C_{K''}^{v''} \; {}^{v,0}\mu_j^{'} \langle J' \; K' \; \gamma' |A_j| J'' \; K'' \; \gamma'' \rangle \right|^2 . \tag{II.72}$$

In Eq. (II.72) the coefficients $C_{K'}^{v'*}$ and $C_{K''}^{v''}$ are obtained from the diagonalization of the upper and lower state Hamiltonian matrix (see Eq. II.71). Then the matrix elements of the A_j operators on the $\left| J\ K\ \gamma \right\rangle$ basis wavefunctions are easily computable as it was established by Flaud *et al* 1981 (*57*). Therefore, for the computation of R_L^U the only missing entities are the $^{v,0}\mu_j^{'}$ constants which are to be determined through a least squares fit performed on the experimental intensities, or estimated from those of other isotopomers, or predicted by ab initio calculations.

II.3 First high resolution analysis of the ν_5 band of DNO$_3$

II.3.1 Existing spectroscopic studies for the first vibrational states of DNO$_3$

For the ground vibrational state of several isotopic species of nitric acid, accurate rotation constants were achieved from high resolution studies performed in the microwave submillimeter and centimeter region (Drouin *et al.* (*31*) and Chou *et al.* (*60*) and references therein).

In the infrared, the vibrational spectrum of nitric acid was measured at low resolution by McGraw *et al.* (*32*) for several isotopic species (H^{14}NO$_3$, D^{14}NO$_3$, H^{15}NO$_3$, D^{15}NO$_3$). As for DNO$_3$, only the ν_2 (NO$_2$ a-stretch) (*33*), ν_6 (O–NO$_2$ stretch) and ν_7 (O–NO$_2$ bend) (*35*), ν_8 (out of plane NO$_2$ bend) (*37*), and ν_9 (O–D torsion) (*38*) fundamental bands were the subject of extensive high resolution infrared studies. Except for the ν_6 band for which a Fermi type resonance coupling the $6^1 \Leftrightarrow 9^2$ interacting energy levels was noticed, all other investigated bands (ν_2, ν_7, ν_8, and ν_9) appeared to be unperturbed.

The present analysis describes the first high resolution study of the ν_5 fundamental band (NO$_2$ in plane bending mode) of DNO$_3$ in the 11 µm spectral region. Fig. II.5 compares the positions of the first vibrational states of H^{14}NO$_3$ and DNO$_3$. For H^{14}NO$_3$ or H^{15}NO$_3$ the energy levels calculation had to account the strong Fermi and C-type resonances coupling the 5^1 and 9^2 energy levels. This is because, as stated in Table II.2, the vibrational energies between 5^1 and 9^2 differ in $\Delta_{99\text{-}5} = E_{99} - E_5 = 14.448$ and $\Delta_{99\text{-}5} = 3.098$ cm^{-1} for H^{14}NO$_3$ or H^{15}NO$_3$, respectively. This value has to be compared with the value, $F_0 = 8.53$ cm^{-1}, where F_0 is the zeroth order term in the expansion of the $5^1 \Leftrightarrow 9^2$ Fermi operator for both H^{14}NO$_3$ (*7*) or H^{15}NO$_3$ (*8*). By diagonalizing the $J = 0$ Hamiltonian matrix using the $\Delta_{99\text{-}5}$ and F_0 values it is possible to estimate the mean $^{99}R^5$ mixing of the 9^2 wavefunctions onto the 5^1 vibrational state defined as

$$^{99}R^5 = \left\langle \left| ^{99}C_{K,\gamma}^5 \right|^2 \right\rangle \tag{II.73}$$

where:

$$\left| 9^2 \ J \ K_a \ K_c \right\rangle = \sum_{K,\gamma} {}^{99}C_{K,\gamma}^5 \left| 5^1 \right\rangle \left| J \ K \ \gamma \right\rangle + \sum_{K,\gamma} {}^{99}C_{K,\gamma}^{99} \left| 9^2 \right\rangle \left| J \ K \ \gamma \right\rangle \tag{II.74}$$

The $\langle \ \rangle$ bracket is for the mean mixing value on the overall $9^2[J\ K_a\ K_c]$ energy levels.

By using the numerical values of $\Delta_{99\text{-}5}$ and F_0 and diagonalizing the $J = 0$ matrix, this $^{99}R^5$ mixing is estimated to be about 41 %, 18 % and 0.2 % for $H^{14}NO_3$ (*7*) and $H^{15}NO_3$ (*8*) and DNO_3, respectively. Therefore, the very weak resonances coupling the 5^1 and 9^2 energy levels of DNO_3 were not considered explicitly.

On the other hand, when examining Table II.2, it is clear that $7^1 9^1$ vibrational state is located ~160 cm^{-1} above the 5^1 state for $H^{14}NO_3$ and $H^{15}NO_3$. On the contrary, for DNO_3, $7^1 9^1$ is only ~5.4 cm^{-1} below 5^1. Therefore, due to symmetry considerations it is clear that A-type and B-type Coriolis resonances coupling together the 5^1 and $7^1 9^1$ energy levels have to be explicitly taken into account for DNO_3.
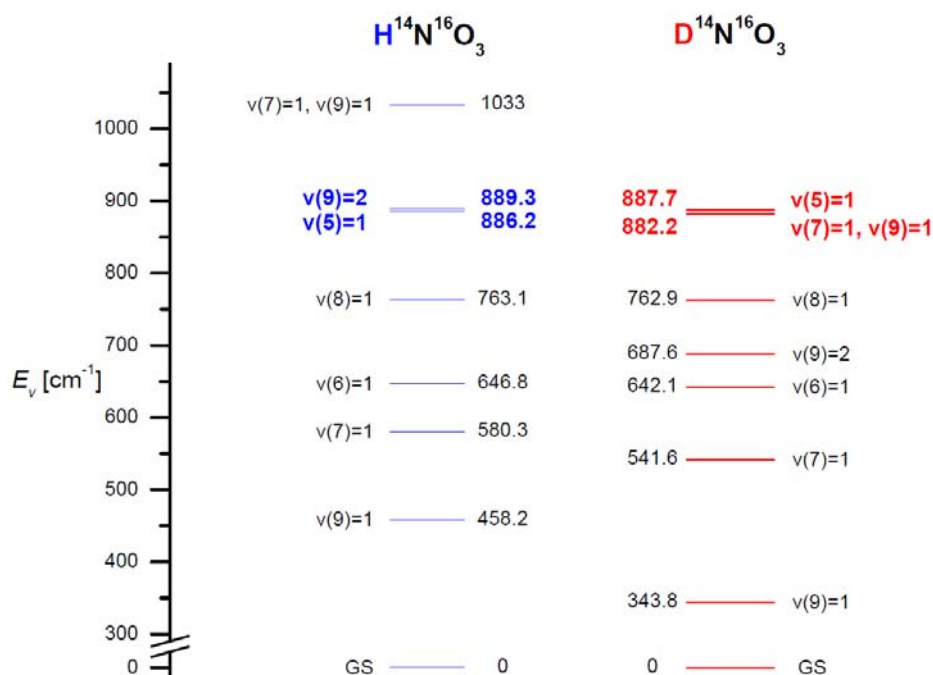
Fig. II.5 Resonance scheme for DNO₃ and HNO₃

II.3.2 Experimental details

The synthesis of DNO_3 and the recording of the high resolution Fourier transform infrared spectra were performed at the Bergische Universität in Wuppertal (Dr. Helmut Beckers and Prof. Helge Willner).

DNO_3 was synthesized from D_2SO_4 (Merck, 96% in D_2O, 99.5 % D) and KNO_3 (Merck). In a 100 mL glass bulb equipped with a magnetic stirring bar and a 10 mm valve with PTFE

stem (Young) 40 g of KNO_3 (0.4 mol) was placed. After the KNO_3 was dried in vacuum for one hour, 25 mL (0.5 mol) of D_2SO_4 was introduced into the bulb. Subsequently the bulb was connected to the vacuum line and the volatile products were distilled through a series of traps held at −20, −100, and −196 °C. The content in the bulb was stirred and heated in a water bath until the gas evolution was terminated. About 20 g of pure DNO_3 was collected in the trap held at −100 °C.

The IR gas cell (glass body, AgBr windows sealed with Kel-F wax, optical path length of 28 cm) was treated with DNO_3 vapour several times, until no proton exchange with the surface could be detected any more. For the final measurements sample pressures of 1.3, 0.4 and 0.1 mbar at cca 23°C (296 K) were used.

The infrared spectra of DNO_3 were recorded with an instrumental resolution of 0.0022 cm^{-1} in the 700−1400 cm^{-1} region on the Bruker IFS 120 HR Fourier transform spectrometer at the University of Wuppertal, equipped with a Globar source, a KBr beam splitter, and a MCT 800 detector. An optical filter was used to eliminate radiation > 1400 cm^{-1}. 60, 121 and 169 scans were co-added for the spectra recorded at pressures of 0.1, 0.4 and 1.3 mbar, respectively.

The calibration of both FT spectra recorded at two different pressures (1 Torr and < 0.1 Torr) in the region 730 – 1400 cm^{-1} was performed via model

$$\sigma_{Ref} = \sigma_{FT}\left(1 + C_{FT}\right), \tag{II.75}$$

using HITRAN 2004 (*61*) collection of H_2O (*62*), HDO (*62*), N_2O (*63*) reference line positions. These species were present in the measured gas mixtures impurities. In case of D_2O the line position values issued directly from an article by Toth (*64*).

13 lines of H_2O, 22 lines of HDO, 50 lines of D_2O and 15 lines of N_2O were localised in the higher pressure spectrum, respectively in the regions 1187 – 1387 cm^{-1}, 1354 – 1386 cm^{-1} , 1127 – 1388 cm^{-1}, and 1258 – 1273 cm^{-1}. This led to determination of the C_{FT} constants respectively 1.70(15) 10^{-6}, 1.71(20) 10^{-6}, 1.54(23) 10^{-6} and 1.65(23) 10^{-6}. These constants were weighted by square of inversed standard uncertainties to form the weighted mean value of 1.66(19) 10^{-6}.

In the lower pressure spectrum, just H_2O and D_2O lines with sufficient intensity were traced. The calibration through some 16, resp. 24, lines from region 1174 – 1386 cm^{-1}, resp. 1042 –

1271 cm^{-1}, led to C_{FT} values of 1.68(30) 10^{-6}, resp. 1.58(25) 10^{-6} which gave the weighted mean value 1.62(27) 10^{-6}.

A spectral resolution of 0.0027 cm^{-1} was determined from the FWHM value of isolated lines.

II.3.3 Analysis

Because of the particular values of the A, B and C rotational constants for nitric acid ($A \sim B \sim 2C$) there exists a K_a degeneracy (resp. a K_c degeneracy) for the rather high K_c values (resp. the very high K_a values): this means that the [J, $K_a = J - K_c$, K_c] and [J, $K_a = J - K_c + 1$, K_c] (resp. [J, K_a, $K_c = J - K_a$] and [J, K_a, $K_c = J - K_a + 1$]) energy levels are degenerate.

As already mentioned in part II.2.2-3, DNO$_3$ is a planar asymmetric molecule (C_S symmetry) and as it is expected by symmetry considerations, the ν_5 band is a hybrid band, with both A- and B-type transitions, with ($\Delta|K_a| =$ even, $\Delta|K_c| =$ odd) and ($\Delta|K_a| =$ odd, $\Delta|K_c| =$ odd) selection rules, respectively.

Fig. II.6 shows the overview of the measured spectrum in the 11 µm region. The lower trace corresponds to the experimental spectrum ($T = 296$ K and $P = 0.1$ Torr). The upper trace is the line by line calculation for DNO$_3$. The Q branch of ν_5 band is centered at 887.65 cm^{-1}. The A-type character of the ν_5 is predominant according to the general aspect of the narrow Q branch for which the strongest lines are A-type transitions involving very high K_a values ($K_a \sim J$).
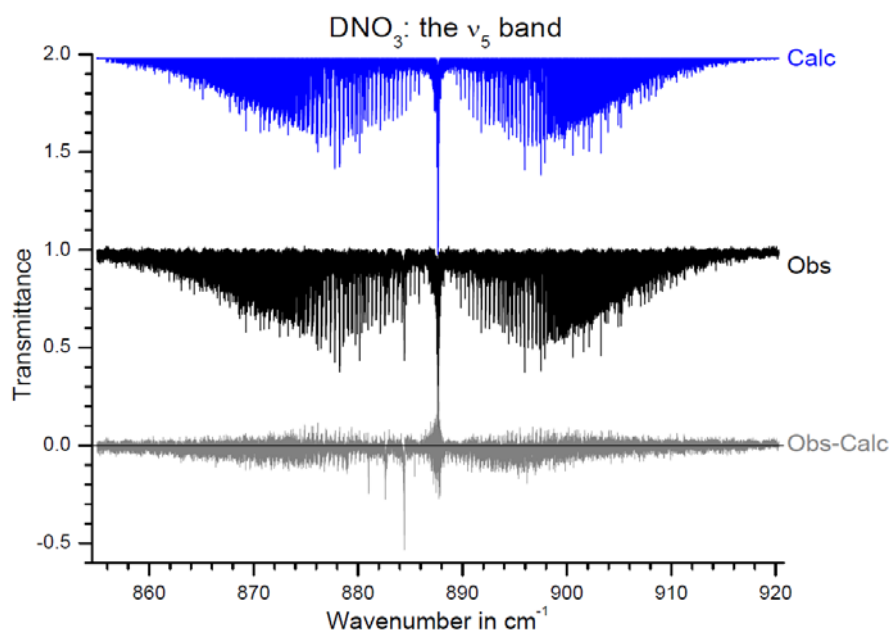

Fig. II.6 Overview of the 855-920 cm^{-1} spectral region with the ν_5 band of deuterated nitric acid

Figs. II.7-9 give details of the spectrum in the P, Q and R branches of the ν_5 band, respectively. In the P and R branches, the strongest P and R lines correspond to transitions involving high K_c values, and because of the K_a degeneracy the A- to B- type character of such transitions cannot be evaluated. The series of lines for low J values (see Fig. II.7) are grouped in stacks corresponding to the same values of $(2J' - K'_c)$, and this helped for the first assignments.

In addition, in the wings of the P and R branches, series of regular weaker transitions involving high K_a values were also observed. These series were assigned as "pure" B-type transitions, as it is exemplified on Fig. II.9. Searching for these B-type transitions, as for example the $[J, K_a = J, K_c = 0 \text{ or } 1] - [J \pm 1, K''_a = J \pm 1, K''_c = 1 \text{ or } 0]$ type transitions, helped us to confirm the A-type assignments in the narrow Q-branch ($[J, K_a = J, K_c = 0 \text{ or } 1] - [J, K''_a = J, K''_c = 1 \text{ or } 0]$ type- transitions).

Fig. II.7 shows some lines of the P branch grouped in stacks corresponding to the same $(2J - K_c)$ values. The quoted assignments are given for the upper K'_c values, with $(2J' - K'_c) = 20$ (solid triangles, ▲) and $(2J' - K'_c) = 21$ (open triangles, △). Due to a resonance which occurs for $K'_c = 14$ and 15, several $\nu_7 + \nu_9$ band transitions are also observed and some assignments are given (diamonds ♦). The "d" letter stands for degenerate transitions with $K_a = J - K_c$ and $K_a = J - K_c + 1$. The lower trace corresponds to the experimental spectrum, the medium and the upper traces are line by line calculations performed for the ν_5 and $\nu_7 + \nu_9$ interacting bands and for the $\nu_7 + \nu_9$ dark band, respectively.

Fig. II.8 shows part of Q branch together with several assignments (solid triangles ▼) of a $^Q Q_{K_a = J - 1}$ sub-branch and two assignments for the $\nu_7 + \nu_9$ band. The lower trace corresponds to the experimental spectrum, the medium and the upper traces are line by line calculations performed for the ν_5 and $\nu_7 + \nu_9$ interacting bands and for the $\nu_7 + \nu_9$ dark band only, respectively.
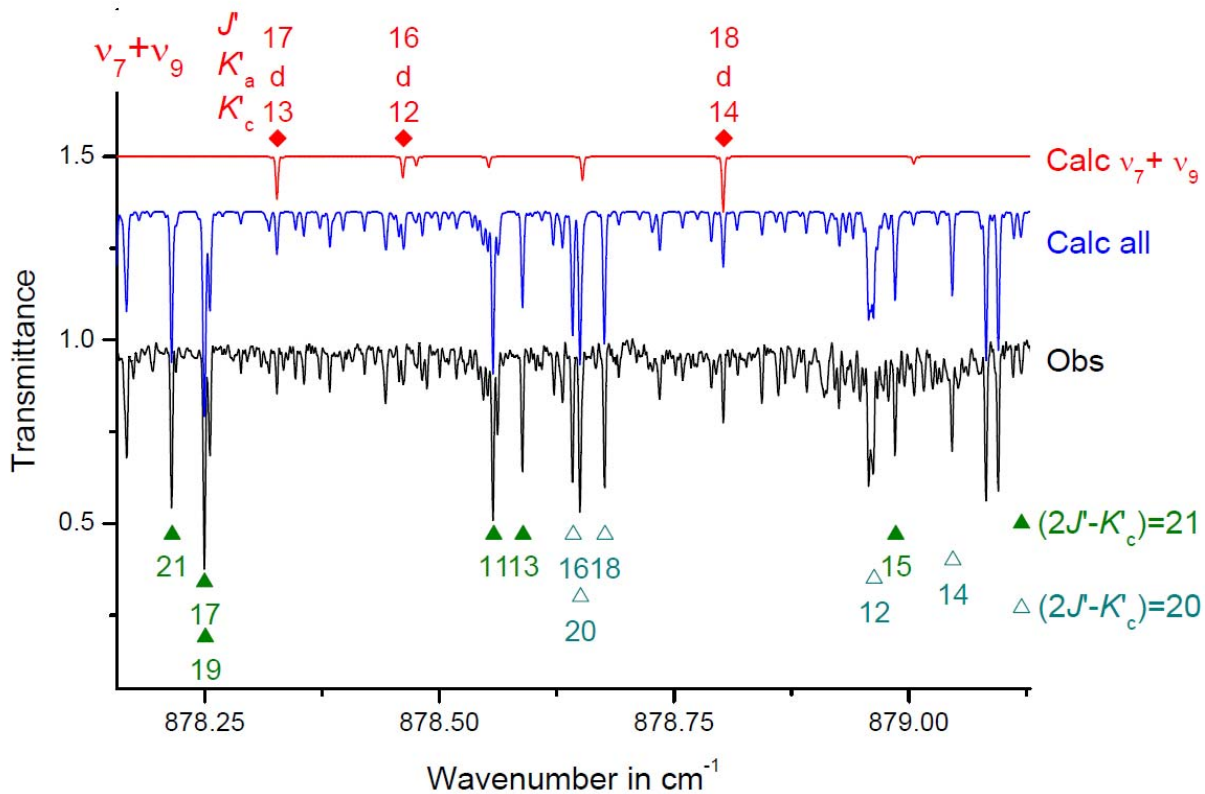
Fig. II.7 Part of P branch of the ν_5 band of DNO$_3$ near 878.6 cm^{-1} (with some upper K_c assignements)
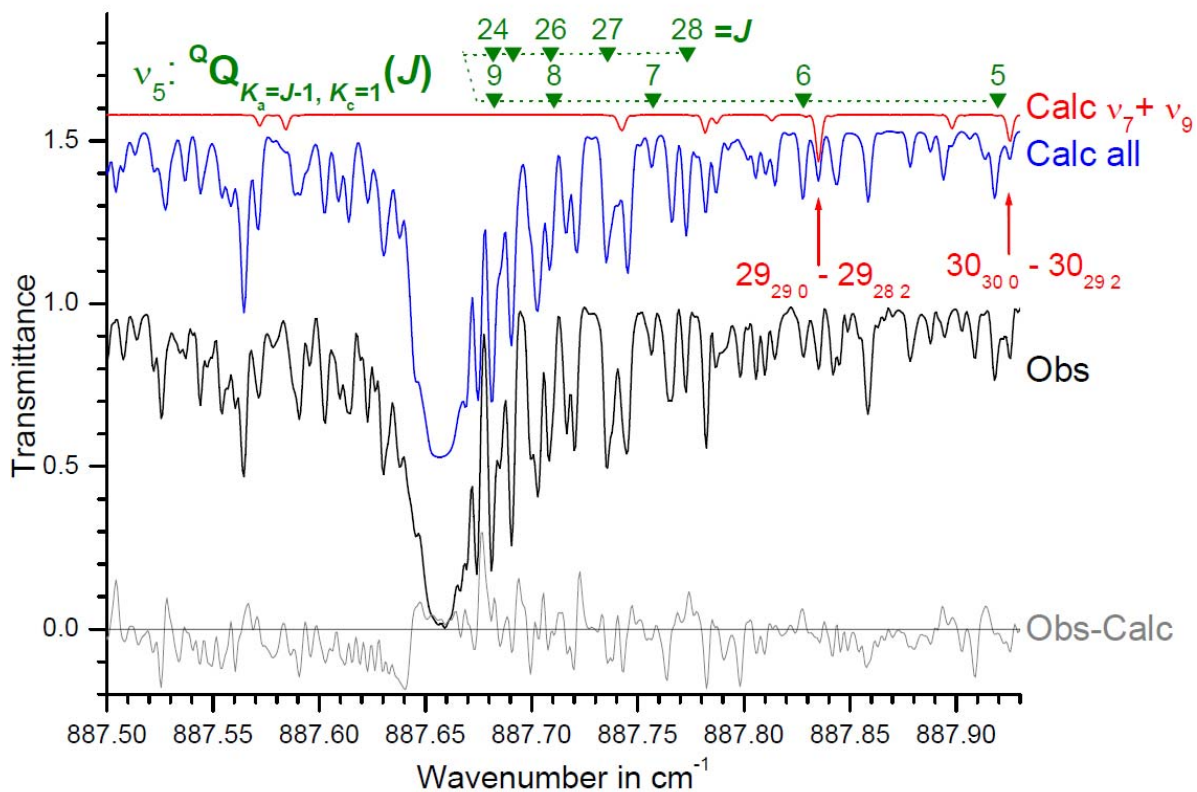
Fig. II.8 Portion of Q branch transitions of the ν_5 band in the 887.7 cm^{-1} spectral region

Fig. II.9 shows part of R branch together with some J' and K'_c (upper state) assignments for the ν_5 band. An example of a pure B- type transition is marked by an arrow. In the upper trace, examples of forbidden transitions for the $\nu_7+\nu_9$ dark (C- type) band are also given. The "d" letter in this case stands for degenerate transitions with $K_c = J - K_a$ and $K_c = J - K_a + 1$. The lower trace corresponds to the experimental spectrum, the medium and the upper traces are line by line calculations performed for the ν_5 and $\nu_7+\nu_9$ interacting bands and for the $\nu_7+\nu_9$ dark band, respectively.
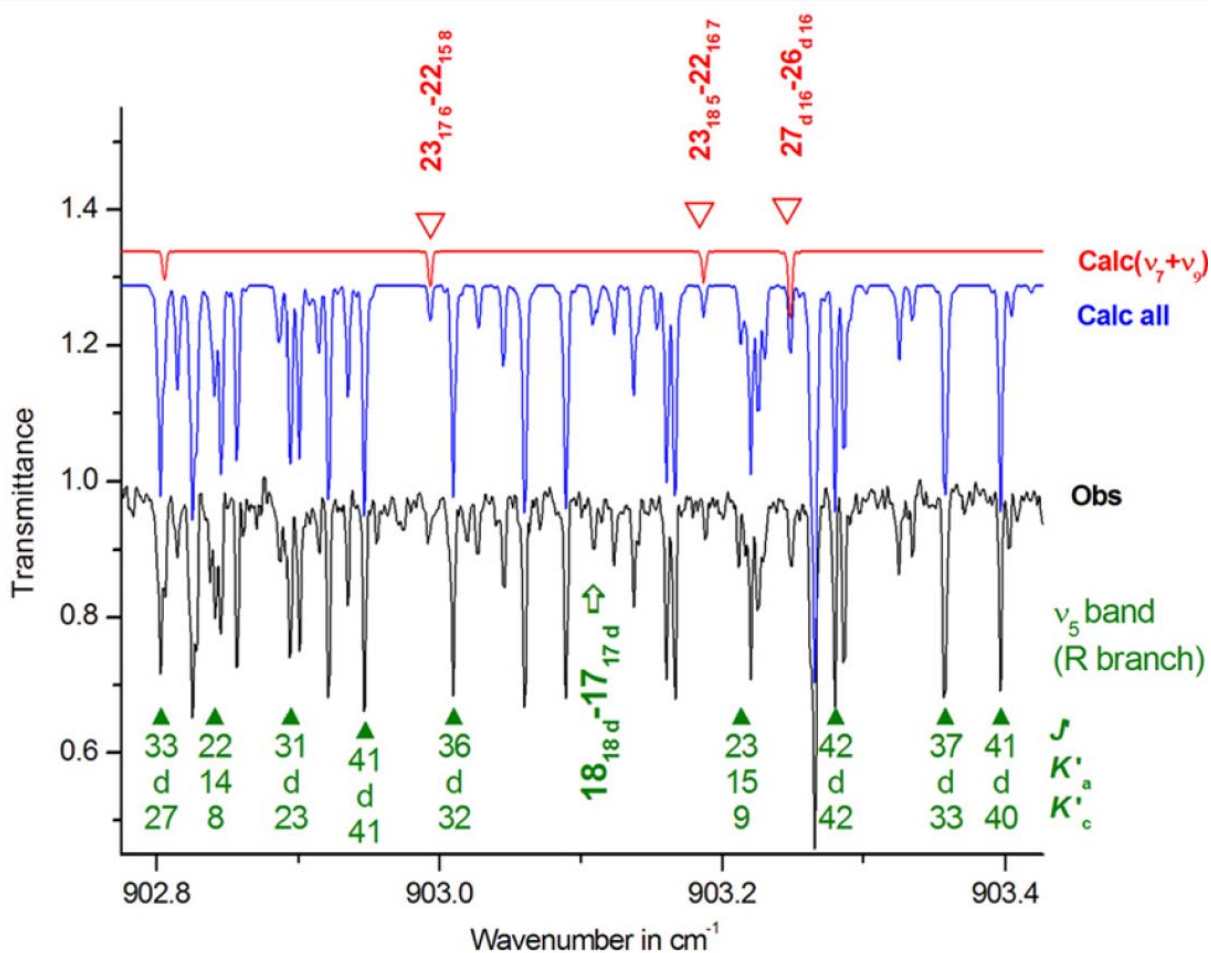
Fig. II.9 Part of R branch of the ν_5 band of DNO$_3$ near 903 cm^{-1}

Because both A- and B-type transitions are observable in the spectra, the synthetic spectrum used for the predictions was generated using, for the line intensities calculation, both A- and B-type components for the ν_5 transition moment operator ${}^5\mu'_Z$:

$$
{}^5\mu'_Z = {}^5\mu_1'^A \varphi_z + {}^5\mu_1'^B \varphi_x \tag{II.76}
$$

In this expression, φ_z and φ_x are the Z_z and Z_x components of the direction cosines between the Z laboratory fixed axis and the $z = a$ and $x = b$ molecular axes. By comparing pure A-type to pure B-type line intensities, the ratio of the absolute values of the A- ($^5\mu_1^{'A}$) to B- ($^5\mu_1^{'B}$) components of the ν_5 band transition moment operator was estimated at the value:

$$\left| {}^5\mu_1^{'B} / {}^5\mu_1^{'A} \right| \approx 0.4 \tag{II.77}$$

The details of the line intensity calculations will be given in Section II.3.4.3.

Some low and medium J and K_a transitions in the ν_5 band were first assigned. Then, using the ground state parameters of Ref. (*31*), the lower state energy levels were calculated and added to the newly observed line positions to get a list of experimental upper state energy levels. These upper state levels were inserted in a least squares fit to get an improved set of upper states parameters allowing better predictions and hence more assignments to be made.

This process was repeated iteratively until it appeared that several series were significantly perturbed, because of resonances involving the energy levels belonging to the 7^19^1 dark state located at 882.211 cm^{-1}. A model accounting for these resonances was then set up, which allowed more accurate predictions, and therefore new assignments. This iterative process was carried out until the ν_5 band was satisfactorily assigned. Table II.12 gives an overview of the results of the present analysis. As the resonances coupling the 5^1 and 7^1+9^1 energy levels are rather strong, it was possible to assign several transitions belonging to the dark $\nu_7+\nu_9$ band. Table II.13 provides a statistical analysis of the energy levels calculations. The standard deviation of the fit is $0.70\ 10^{-3}$ cm^{-1}.

	ν_5	$\nu_7 + \nu_9$
Nb of lines	2938	137
J_{Max}	68	40
Maximum K_a values	44	33
Nb of levels	1078	75

Table II.12 Range of the observed energy levels

	5^1	$7^1 9^1$
Nb of levels	1078	75
$0 \leq \delta < 1.0$	94.0 %	81.3 %
$1.0 \leq \delta < 2.0$	3.6 %	4.0 %
$2.0 \leq \delta < 4.0$	1.7 %	10.7 %
$4.0 \leq \delta < 10.0$	0.7 %	4.0 %

Table II.13 Statistical analysis ($\delta = \left| E_{obs} - E_{calc} \right|$ in 10^{-3} cm^{-1})

In addition, it has to be mentioned that lines from several hot bands were observed in the spectrum during the analysis. Fig. II.10 identifies the Q-branches of the $\nu_5+\nu_6-\nu_6$, $\nu_5+\nu_7-\nu_7$ and $\nu_5+\nu_9-\nu_9$ hot bands at 881.03, 882.61 and 884.45 cm^{-1}, respectively. These assignments are based on considerations on the relative intensities of these hot bands. In this way the position of the 5^1+6^1, 5^1+7^1 and 5^1+9^1 vibrational states of DNO$_3$ is estimated at 1523.17, 1424.20 and 1228.30 cm^{-1}, respectively, therefore, in good agreement with the low resolution measurements of McGraw *et al.* (*32*) ($\nu_5+\nu_6 \sim$ 1520 cm^{-1} and $\nu_5+\nu_7 \sim$ 1424 cm^{-1}). Because of the complexity of the spectrum, no further detailed analysis could be performed for these hot bands. Unobserved center of the $\nu_7+\nu_9$ dark band was calculated at 882.211 cm^{-1}.
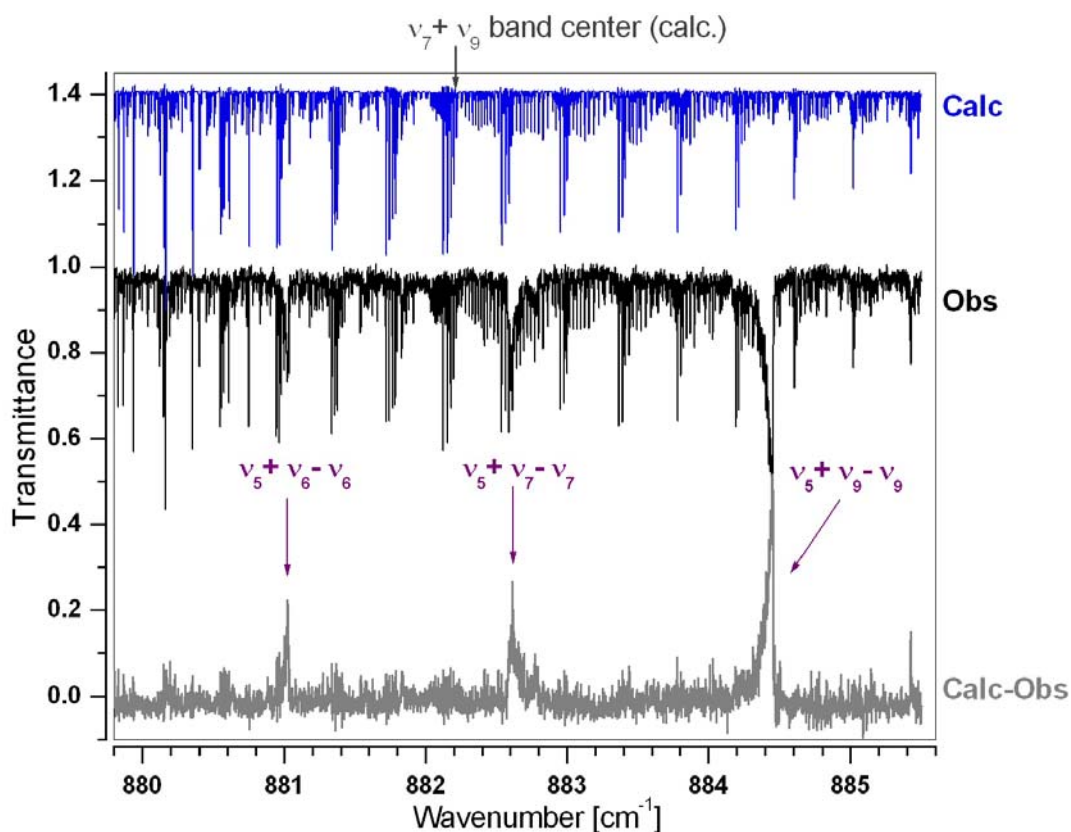
Fig. II.10 Portion of the P branch of the ν_5 band of DNO$_3$ near 883 cm^{-1}: Identification of the $\nu_5+\nu_6-\nu_6$, $\nu_5+\nu_7-\nu_7$ and $\nu_5+\nu_9-\nu_9$ hot bands

II.3.4 Energy levels and intensity calculation

II.3.4.1 Hamiltonian

The form of the Hamiltonian matrix used for the $\{5^1, 7^1 9^1\}$ interacting states of DNO_3 is described in Table II-14.

	5^1	$7^1 9^1$
5^1	$H_{5,5}$	Complex conjugate
$7^1 9^1$	$C_A + C_B$	$H_{79,79}$

Table II.14 Hamiltonian matrix - The $\{5^1, 7^1 9^1\}$ resonating states

As it is the case usually for planar C_s type molecules, the v-diagonal parts of this model are

A-reduced Watson-type Hamiltonians written in the I^r representation:

$$H_{v,v} = E_v + \left[A^v - \frac{1}{2}\left(B^v + C^v\right) \right] J_z^2 + \frac{1}{2}\left(B^v + C^v\right) \mathbf{J}^2 + \frac{1}{2}\left(B^v - C^v\right) J_{xy}^2$$

$$- \Delta_K^v J_z^4 - \Delta_{JK}^v J_z^2 \mathbf{J}^2 - \Delta_J^v \left(\mathbf{J}^2\right)^2 - \delta_K^v \left\{ J_z^2, J_{xy}^2 \right\} - 2\delta_J^v J_{xy}^2 \mathbf{J}^2 + \dots \tag{II.78}$$

$$\{A, B\} = AB + BA, \quad J_{xy}^2 = J_x^2 - J_y^2$$

Due to the relative symmetry of the $5^1 \leftrightarrow 7^1 9^1$ interacting states ($A' \leftrightarrow A''$), both A-type and B-type Coriolis operators are considered in the $5^1 \Leftrightarrow 7^1 9^1$ off diagonal blocks:

$H_{5,79} = C_A + C_B$ (A-type Coriolis, B-type Coriolis)

$$C_A = C_{A1}\, J_z + C_{A2}\left\{ iJ_y, J_x \right\} \tag{II.79}$$

$$C_B = C_{B1}\, J_x + C_{B2}\left\{ iJ_y, J_z \right\} + C_{B3}\, J_x \mathbf{J}^2 + C_{B4}\, J_x J_z^2 + C_{B5}\left(J_+^3 + J_-^3 \right) \tag{II.80}$$

The final energy levels calculation was performed for the $\{5^1, 7^1 9^1\}$ resonating states. The experimental 5^1 and $7^1 9^1$ energy levels obtained in this work were introduced in a least squares fit using this Hamiltonian model. Tables II.15 and II.16 list the Hamiltonian parameters (band centers, rotational and interacting constants, in cm^{-1} units) resulting from the fit, together with their associated statistical uncertainties (for one standard deviation). Several rotational or centrifugal distortion constants were maintained fixed at their ground state values (*31*). One has to remind that since the informations available on the rotational structure of the $7^1 9^1$ dark state concern a small sample of perturbed levels (75 as compared to

1078 for the 5^1 bright state). For this reason the rotational and centrifugal distortion constants for the 7^19^1 resonating state are effective ones, with poor physical meaning.

The results of the energy levels calculations proved to be rather satisfactory, as can be seen from the standard deviation and statistical analysis given in the Table II.13. However, several resonances could not be completely accounted for satisfactorily. Indeed the most significant disagreements are observed starting from $J\sim30$ for the levels of the 5^1 state with $K_c = 1$, 2 and 3 (with $K_a = J - K_c$ and $J - K_c + 1$). As it will be discussed in the next paragraph, this is because these resonances are local, and difficult to predict.

	0	**5^1**	**7^1+9^1**
E_V		887.657186(81)	882.20837(21)
A	0.43265424876	0.43245812(300)	0.43176867(490)
B	0.37734930500	0.376607964(570)	0.37572761(340)
C	0.20130393744	0.200482401(180)	0.20019724(320)
Δ_K	2.13530×10^{-7}	$1.61221(130)\times10^{-7}$	$3.81447(150)\times10^{-7}$
Δ_{KJ}	-0.15060×10^{-7}	$0.4704(150)\times10^{-7}$	$-1.4266(480)\times10^{-7}$
Δ_J	2.326846×10^{-7}	$2.11850(850)\times10^{-7}$	$2.450(17)\times10^{-7}$
δ_K	2.485385×10^{-7}	$3.39012(790)\times10^{-7}$	$1.6354(550)\times10^{-7}$
δ_J	0.958026×10^{-7}	$0.85602(460)\times10^{-7}$	$1.2368(210)\times10^{-7}$
H_K	0.6831×10^{-11}	$1.1408(140)\times10^{-11}$	#
H_{KJ}	-0.6856×10^{-11}	#	#
H_{JK}	1.7855×10^{-12}	#	#
H_J	-0.8156×10^{-13}	#	#
h_K	0.7103×10^{-12}	#	#
h_{JK}	0.4954×10^{-12}	#	#
h_J	-0.3070×10^{-13}	#	#
L_K	-1.420×10^{-16}	#	#
L_{KKJ}	1.2329×10^{-16}	#	#
l_{KKJ}	1.90×10^{-17}	#	#
l_{JJK}	-4.420×10^{-18}	#	#

Table II.15 Vibrational energies and rotational constants for the dyad $\{5^1,7^19^1\}$ (# Fixed to the ground state values [Drouin *et al.* (*31*)])

Operator	Parameter	Value in cm^{-1}
J_z	C_{A1}	$3.3410(25) \times 10^{-2}$
$\{i\,J_y, J_x\}$	C_{A2}	$4.622(110) \times 10^{-4}$
J_x	C_{B1}	$6.94941(560) \times 10^{-2}$
$\{i\,J_y, J_z\}$	C_{B2}	$1.25664(370) \times 10^{-3}$
$J_x J^2$	C_{B3}	$-1.044(100) \times 10^{-6}$
$J_x J_z^2$	C_{B4}	$6.3721(860) \times 10^{-6}$
$J_+^3 + J_-^3$	C_{B5}	$1.1546(160) \times 10^{-6}$

Table II.16 Coriolis interaction constants

II.3.4.2 Resonances

Due to the close proximity (Fig. II.5) of the 5^1 and $7^1 9^1$ energy levels of DNO$_3$, strong perturbations are observed during the analysis of the ν_5 band. Through A-type and B-type Coriolis resonances the wavefunctions of the $7^1 9^1$ "dark" state are mixed with those from the "bright" 5^1 state, and therefore many $\nu_7 + \nu_9$ transitions become observable.

In order to characterize these mixings and get an idea of the strength of the resonances we plot on Fig. II.11 the percentage of mixing coefficients of the 5^1 energy levels on the $\left| 7^1 9^1 \right\rangle$ vibrational state, defined as:

$$\% \left(7^1 9^1; v = 5^1 \right) = \sum_{k,\gamma} \left| {}^{79}C^5_{k',\gamma'} \right|^2 , \tag{II.81}$$

where the ${}^{79}C^5_{k',\gamma'}$ are the coefficients appearing in the expansion of the $v = 5^1$ wavefunctions resulting from the diagonalization of the Hamiltonian matrix:

$$\left| 5^1, J\,K_a\,K_c \right\rangle = \sum_{k',\gamma'} {}^{79}C^5_{k',\gamma'} \left| 7^1 9^1 \right\rangle \left| J\,k'\,\gamma' \right\rangle + \sum_{k,\gamma} {}^{5}C^5_{k,\gamma} \left| 5^1 \right\rangle \left| J\,k\,\gamma \right\rangle \tag{II.82}$$

In Eq. (II.82), $\left| J\,k\,\gamma \right\rangle$ and $\left| J\,k'\,\gamma' \right\rangle$ are the classical Wang's type symmetrized wavefunction (see Eqs. II.31 and II.32):

Fig. II.11 shows that rather regular resonances couple together the $\left| 5^1, J\,K_a\,K_c \right\rangle$ with $\left| 7^1 9^1, J\,K_a'\,K_c' \right\rangle$ energy levels for $K_c \geq 14$ and $K_c' = K_c - 1$, and these resonances reach its maximum for $J \sim -31 + 3.5 K_c$ (see the bottom trace of Fig. II.11). In addition, as it can be seen on the upper trace of Fig. II.11, numerous local and sharp resonances are observed for

low K_c values (and therefore high K_a values), with $K'_c = K_c - 3$ or $K'_c = K_c - 1$ selection rules. For the very low K_c values ($K_c = 1$, 2 and 3 in the upper panel) the resonances are sharper than for higher K_c values ($K_c = 14$ to 18 in the lower panel).
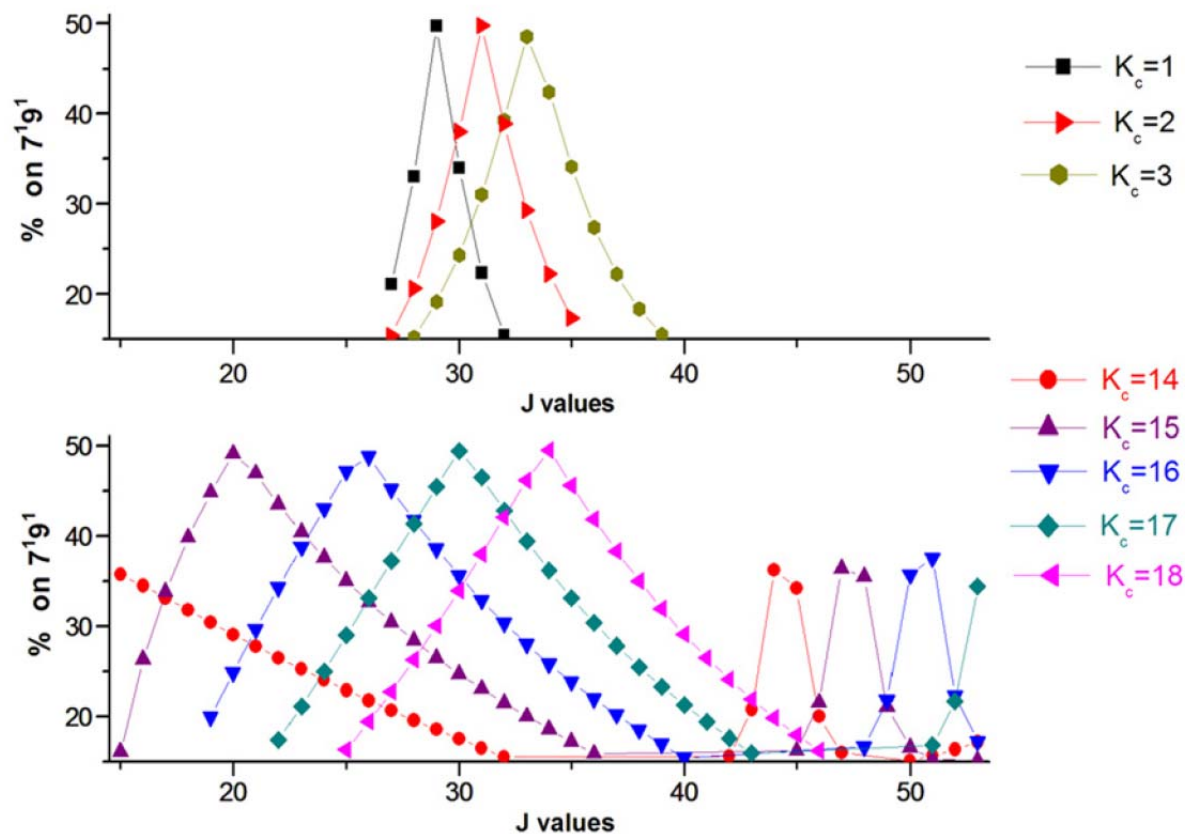
Fig. II.11 Mixing (in %) of the 5^1 [J, K_a, K_c] energy levels on the $7^1 9^1$ state versus J for different K_c values.

For the 5^1 energy levels involving high K_a values (i.e. low K_c) perturbed by $7^1 9^1$ energy levels, the resonances are difficult to model. This is because the rotational and centrifugal distortion constants for the $7^1 9^1$ resonating state obtained in this work are effective ones, preventing accurate predictions for the presumed resonating $\left| 7^1 9^1, J\, K'_a\, K'_c \right\rangle$ energy levels involving low K'_c values.

Examples of resonances were observed during the assignment of the spectrum. An example of the first type of perturbations due to the resonances involving the $5^1[J = 17$, $K_a = $ d, $K_c = 14] \Leftrightarrow 7^1 9^1[J = 17$, $K'_a = $ d, $K'_c = 13]$ and $5^1[18$, d, $15] \Leftrightarrow 7^1 9^1[18$, d, $14]$ upper levels (the d stands for the K_a degenerated value, $K_a = J - K_c$ and $J - K_c + 1$) is clearly observable in Fig. II.7. Also Fig. II.8 and II.9 give examples of resonances involving low K_c values in the Q

and R branches, respectively. Due to these resonances several transitions from the $\nu_7+\nu_9$ dark are clearly observable.

II.3.4.3 Intensity calculation

Line intensity calculations were performed using the theoretical treatment which was detailed in paragraph II.2.5.

As it was mentioned previously the $\nu_7+\nu_9$ is a dark band, and only the transition moment operator from the ν_5 bright band ($^5\mu_z'$) is supposed to contribute in the expansion given in Eq. (II.76).

Since both A-type and B-type ν_5 transitions were observed for DNO_3, the first order expansion of the transition moment operator $^5\mu_z'$ is written in the form given in Eq. (II.76), and the relative values of $^5\mu_1'^A$ and $^5\mu_1'^B$ were estimated according to the ratio of Eq. (II.77).

To the writer's knowledge, there exists no reported band intensity for the ν_5 band of DNO_3. Consequently as for $H^{15}NO_3$ (*8*), an estimation of the "absolute" line intensities was performed using the transition moment operator of the ν_5 band of $H^{14}NO_3$ (*7*).

For the (almost) pure A-type ν_5 band of $H^{14}NO_3$ the first order in the expansion of the transition moment operator is written

$$^5\mu_z'(H^{14}NO_3) \approx\ ^5\mu_1'^A(H^{14}NO_3)\varphi_z + \ldots \tag{II.83}$$

with, from Ref. (*7*):

$$^5\mu_z^{1A}(H^{14}NO_3) =\ 0.250132\ D, \tag{II.84}$$

using the expression:

$$\left|^5\mu_z^{1A}(H^{14}NO_3)\right|^2 \approx \left|^5\mu_z^{1A}(DNO_3)\right|^2 + \left|^5\mu_z^{1B}(DNO_3)\right|^2 \tag{II.85}$$

one gets:

$$^5\mu_z^{1A}(DNO_3) =\ 0.232\ D \ \text{and}\ ^5\mu_z^{1B}(DNO_3) = 0.095 D \tag{II.86}$$

Finally, the synthetic spectrum of the ν_5 band of DNO_3 was calculated in the region 846.5 – 929.6 cm^{-1}. The line positions were computed using the band centers and rotational and coupling constants which are given in Tables II.15-16 for the upper $\{5^1, 7^1 9^1\}$ resonating states and in Ref. (*31*) for the vibrational ground state.

The intensities were computed using the method described above and the A- and B- type components of the ν_5 transition moment operator given in Eq. (II.86). The calculations were performed for a "pure" isotopic sample of DNO_3 using an intensity cutoff of 0.5 x10^{-22}cm^{-1}/(molecule.cm^{-2}) at 296 K, maximum values of 70 for J' and 50 for K'_a, maximum upper and lower state energies of 2000 cm^{-1} and 1200 cm^{-1}, respectively. In this way, about 28000 lines were generated and the values

$$^{\nu_5}S(296 \text{ K})=1.37\text{x}10^{-17} \text{ cm}^{-1}/\left(\text{molecule.cm}^{-2}\right) \tag{II.87}$$

$$^{\nu_7+\nu_9}S(296 \text{ K})=0.12\text{x}10^{-17} \text{ cm}^{-1}/\left(\text{molecule.cm}^{-2}\right) \tag{II.88}$$

at 296 K were achieved for the ν_5 and $\nu_7+\nu_9$ band intensities of DNO_3, showing that the $\nu_7+\nu_9$ dark band borrows about 8 % of the ν_5 band's intensity. This final list of line positions and intensities generated for the 11 μm bands of DNO_3 has been deposited as supplementary data at the Journal of Quantitative Spectroscopy and Radiative Transfer and is available on-line (*34*).

Some comparisons between the observed and calculated spectra are given through Figs. II.6-10, the agreement between the observed and calculated spectra is in general reasonably good when one considers the difficult treatment of the interaction between 5^1 and $7^1 9^1$ states.

II.3.5 Conclusion

Using new high resolution Fourier transform infrared spectra recorded at Bergische Universitat in Wuppertal, the first analysis of the ν_5 bright band and a partial identification of the $\nu_7+\nu_9$ dark band of DNO_3 have been performed. The theoretical models which were used to calculate the line positions and intensities account for very strong Coriolis resonance (A-type and B-type) which perturb the 5^1 and 7^1+9^1 rotational energy levels. Finally a synthetic spectrum of the ν_5 band of DNO_3 was generated, using a realistic estimation of its transition moment operator.

III CH₃F collisional effect studies – experimental part

III.1 Experimental set-up

Pure rotational spectra and Stark split pure rotational spectra of $^{12}CH_3F$ used in this study in Chapters IV and V were recorded for the transitions $J: 1 \to 2$ (102 GHz) and $J: 3 \to 4$ (204 GHz) with semiconductor millimeter wave high resolution spectrometer (described in Refs. (65-67)) and the 1.5 m long Stark cell (see Fig. III.1) at ICT Prague.
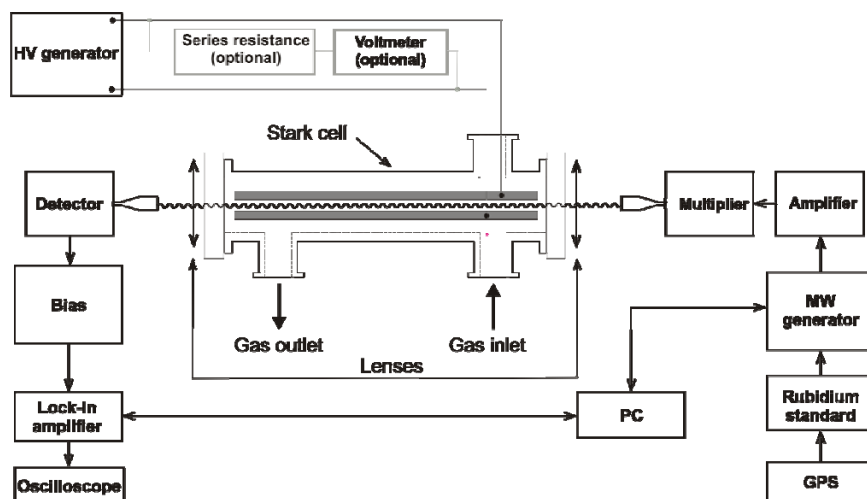
Fig. III.1 Scheme of the Prague MW spectrometer with the Stark module

Some measurements extending the lineshape study of pure rotational lines will be measured using a 3 m long free space cell without the Stark electrodes (see Fig. III.2).
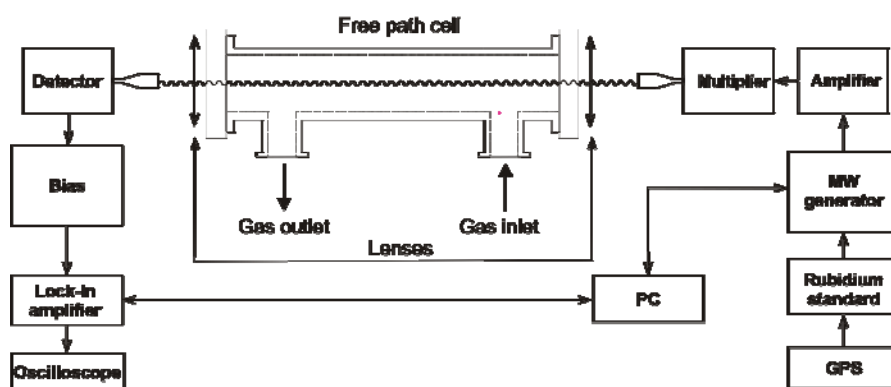
Fig. III.2 Scheme of the Prague MW spectrometer with free path cell only

It is also possible to arrange a two-way pass of the e.m. beam using 90 deg. roof top mirror with its ridge rotated at 45 degrees (compared to the direction of either electric or magnetic vector of the incident microwave (see Fig. III.3)). A polarization grid lets pass the initial

radiation through its wires into the cell but mirrors the returning beam (characterized by orthogonal orientation of its components in comparison to the initial orientation) into the detector.
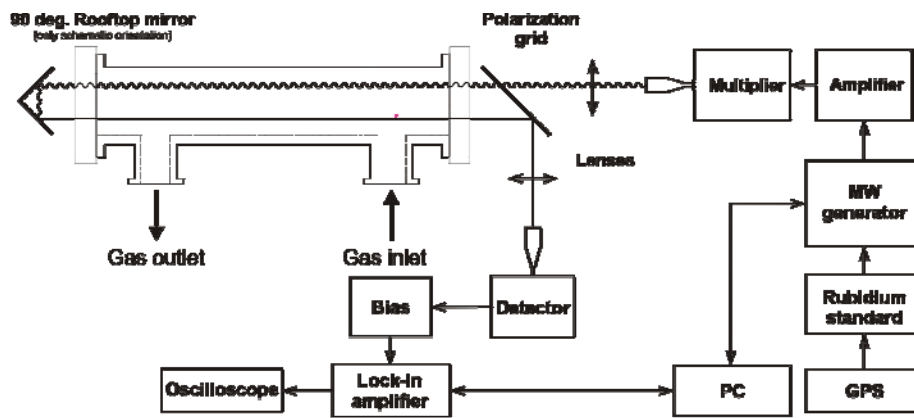
Fig. III.3 Scheme of a set-up with doubled absorption path

The microwave radiation is synthesized using a swept signal generator 83650 B (Agilent) operating from 10 MHz to 50 GHz. The signal generator is phase-locked to a rubidium atomic clock that is controlled by the cesium frequency standard via the GPS system. The frequencies above 50 GHz are generated using a set of frequency multipliers. For this study a home made tripler by Dr. Vowinkel (Köln University) and a WR 4.3x6 sextupler produced by Virginia Diodes were used together with the high power semiconductor amplifier AHP 3404 by Wisewave Technologies that ensured a sufficient radiation power before the frequency multiplication. The millimeter set-up uses a set of Schottky non-cooled diodes as detectors, in this case WR 8 ZBD and WR 5.1 ZBD detectors by Virginia Diodes. The rotational lines were measured using amplitude modulation since this modulation makes possible a more subtle numerical evaluation of the spectral background and overlapping lines than frequency modulation. An accuracy of the well developed lines measured by the amplitude modulation and subjected to the numerical treatment is estimated to be close to 10 kHz.

III.2 Pure rotational transition measurements

In the present study, microwave spectra were recorded for total pressures ranging from 3 to 250 μbar in the case of pure CH_3F and from 100 to 500 μbar in the case of CH_3F diluted in He (x_{CH3F} around 0.1). All measurements were made at room temperature and the sample pressures were measured by a capacitance gauge from Leybold CTR 91 in the range from 5 to 130 μbar and Leybold CTR 100 in the range from 5 to 500 μbar with relative uncertainty of about 5 %. Methyl fluoride (with natural isotopolog abundances) and helium were provided by Linde Gas with stated purities of 99.5 %, and 99.994 %, respectively.

First, a check of optimal absorption conditions was carried out in order to avoid the higher energy levels' saturation that would lead to nonlinear absorption. The power of generated probing microwaves at 102 (resp. 204) GHz was held at −22 (resp. −7) dBm for pressures above 7 (resp. 5) μbar. At lower sample pressures, the respective radiation input powers led to the significant saturation of CH_3F spectra and lower powers detered the signal to noise ratio due to high noise, as is shown in Fig. III.4-5. The indicated saturation of a line for given pressure was calculated as proportion of its intensity to the intensity of the same line measured with least intensive power. This calculation gives only approximative values since they are overrated - the signal to noise ratio is particularily low for low input microwave powers and so the maximal intensity may be overestimated.

Figures III.6-7 display experimental absorbancies for the J: $1 \rightarrow 2$ and J: $3 \rightarrow 4$ pure rotational transitions of methyl fluoride used further in the analysis.
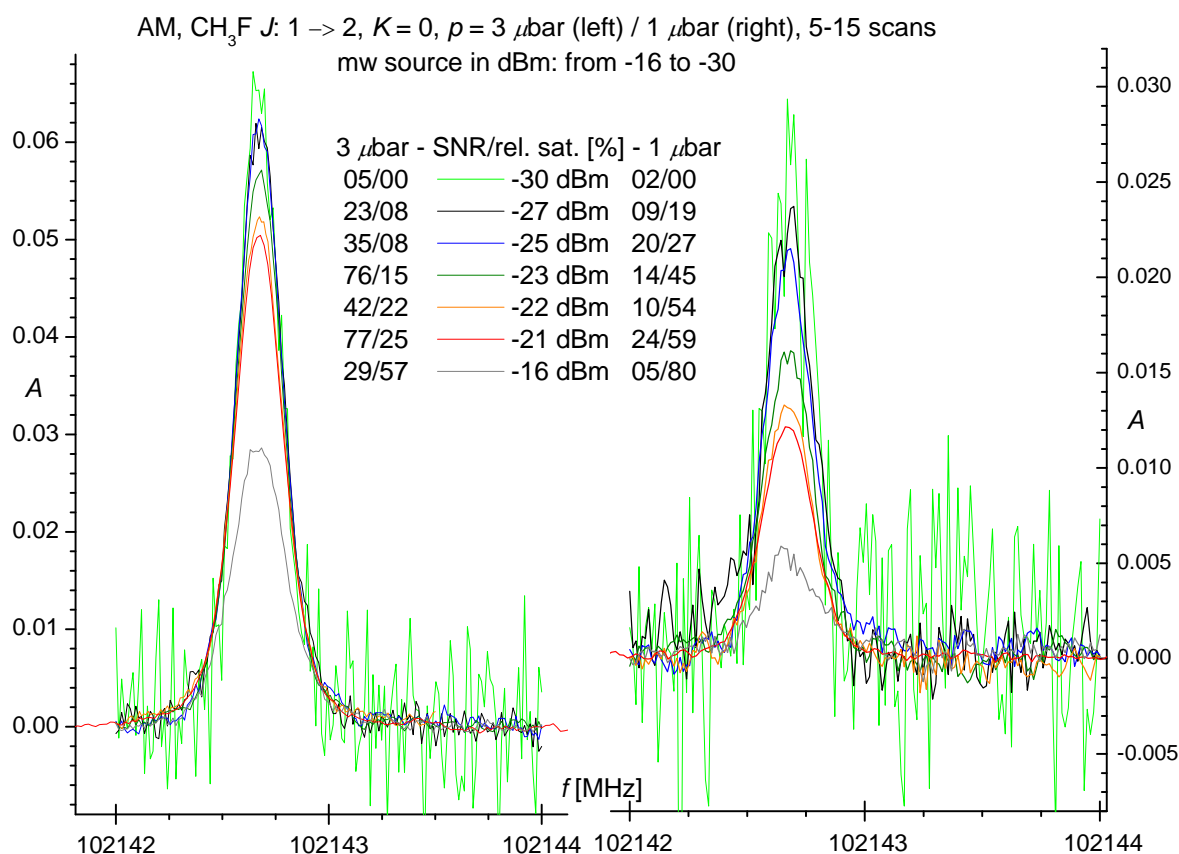
Fig. III.4 Saturation and signal to noise ratios of a CH₃F $J'' = 1$ line for different pressures and input microwave powers
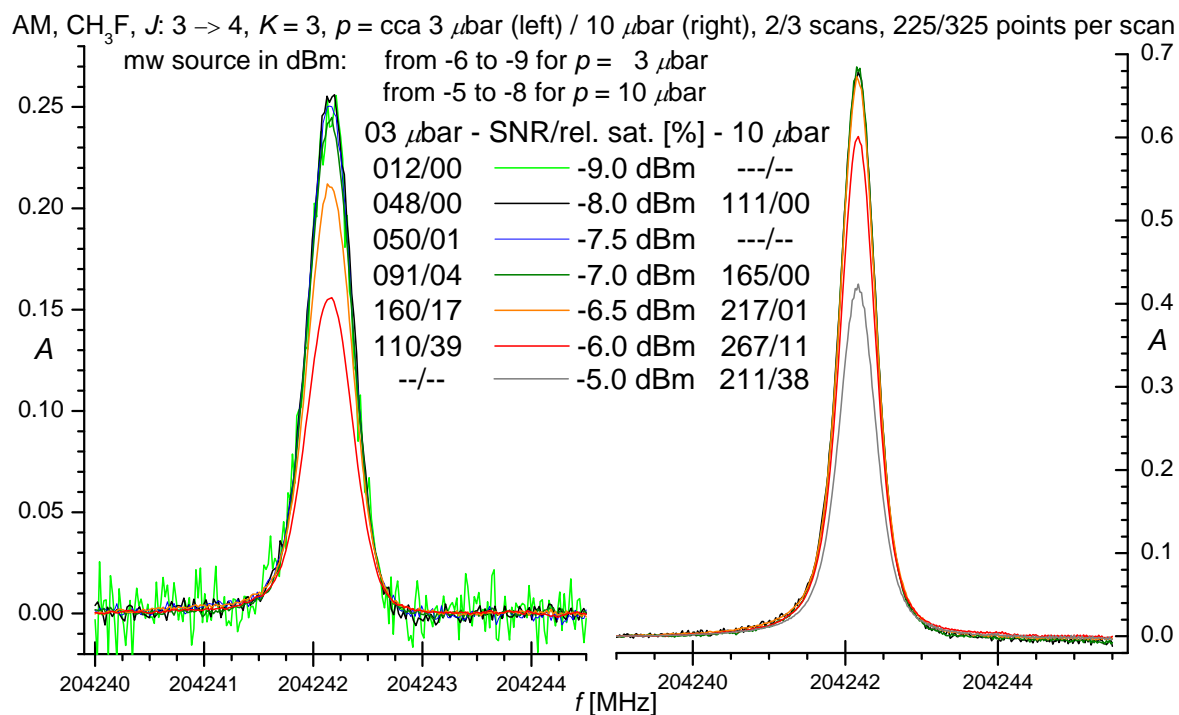
FIG. III.5 Saturation and signal to noise ratios of a CH₃F $J'' = 3$ line for different pressures and input microwave powers
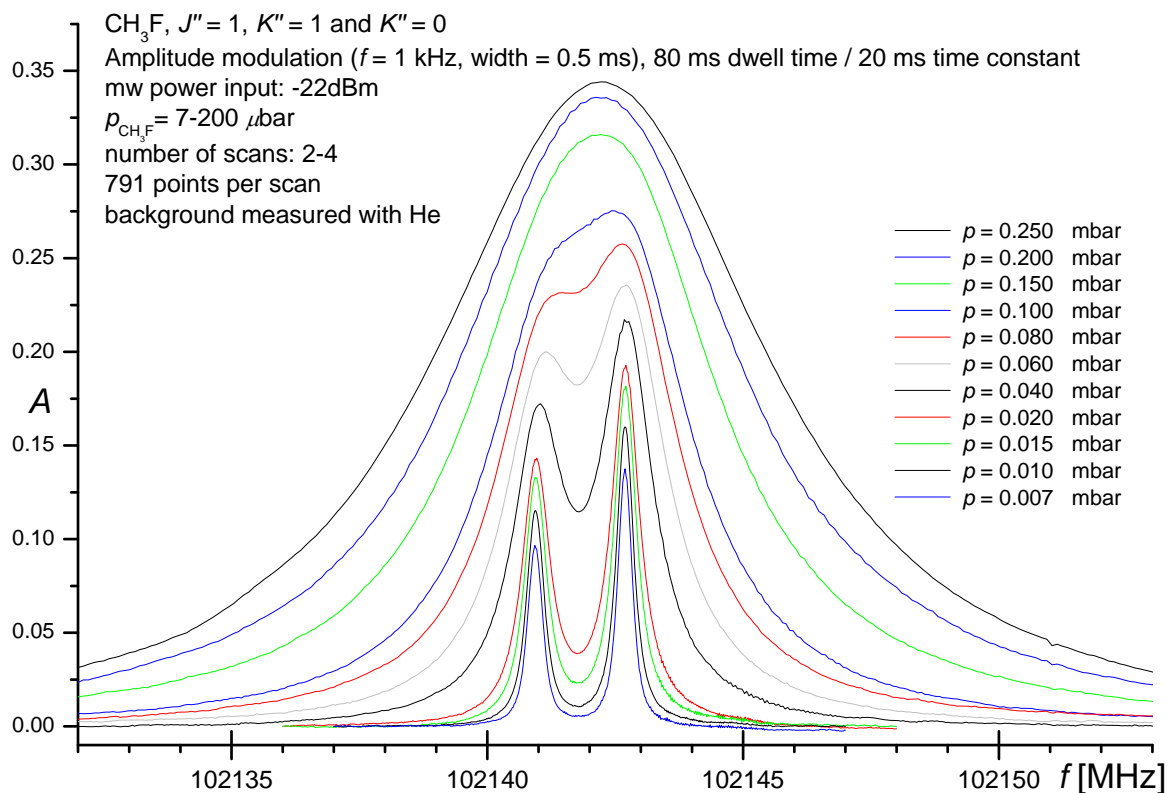
Fig. III.6 Methyl fluoride $J'' = 1$ pure rotational spectra at different pressures
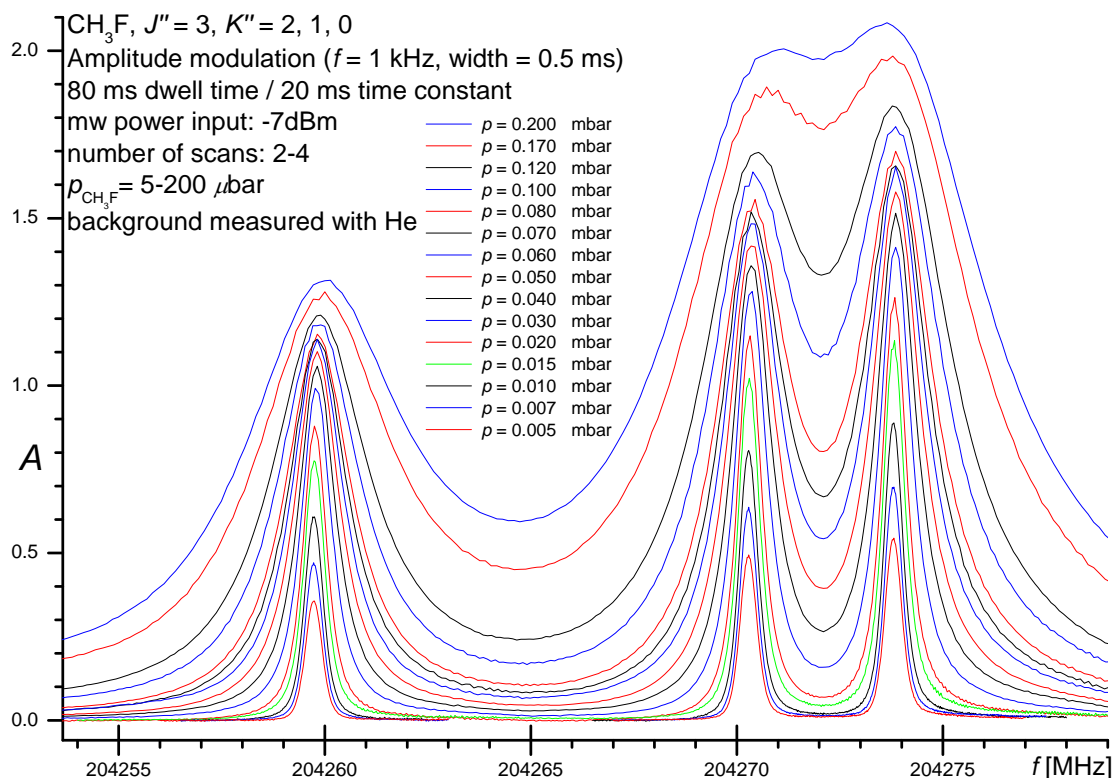
FIG. III.7 Methyl fluoride $J'' = 3$ pure rotational spectra at different pressures

A multifit procedure was used on all estimated non-saturated spectra for given J'' to retrieve experimental line positions, lineshifts and line widths. Using known rotational constants (*68*),

partition functions (at 296 K, $Z_{rot} = 7217.4$, $Z_{vib} = 1.015$ from Ref. (*69*)) and permanent electric dipole moment value (*70*), the absorption coefficients were calculated for all considered transitions. In the pressure multifit procedure the list of experimental files (for given *J*) to be analysed is first read. The experimental files are specified by the *J* number and pressure level in μbar and contain the measured frequencies and the experimental absorbancies. The experimental absorbancies are calculated as negative values of natural logarithms of the transmittance I/I_0 where *I* is detector signal (voltage) for measured absorbent gas and I_0 is detector signal (voltage) for the spectral background. The respective detector signals are averaged values issuing from multiple scans. By considering all the data for all the pressures in each iteration, this approach enables to fit also the characteristics of the spectral lines as pressure shift [MHz/Torr] and collisional broadening [MHz/Torr] over multiple pressures, including the higher pressures under which some or all treated lines are no more isolated due to pressure broadening. The pressure values are on the other hand with respect to the calculated absorption coefficients. This approach assumes the identity of the pressure value for all lines at given pressure level. This is not granted and care had to be taken during experiment to keep the pressure for such different measurements as close as possible since the dosing of the gas in the cell was carried out manually in this work. This applies for low pressures and higher *J* (e.g. for *J″*=3 lines, different *K* lines were measured separetely at the same pressure level).

III.3 Specificities of the measurements in the significant external electric field

Stark spectra of $^{12}CH_3F$ (whether pure or in mixture with helium) were recorded for *J*: $1 \rightarrow 2$ (102 GHz) and *J*: $3 \rightarrow 4$ (204 GHz) using the Stark module (see Fig. III.1) and the semiconductor millimeter wave high resolution spectrometer at the ICT in Prague. The probing electromagnetic radiation (microwave, millimeterwave, submm wave) travels between and along the Stark electrodes and transmits its power to the rotational modes of absorbing species. When the electric tension is applied on one electrode while the other is grounded, the spatial isotropy is withdrawn and the intensity of electric field between Stark plates separates the energy levels of the space orientation sensitive components (characterised by quantum number *M*) as shown in Fig. III.8. The selection rules for the Stark transitions depend on the orientation of the external electric intensity vector towards electric component of the probing beam. $\Delta M = 0$ rule applies in case of parallel orientation, $\Delta M = \pm 1$ characterizes othogonal orientation.

In these measurements, the orientation of the electric field has been set parallel or orthogonal to the electric vector of the polarized microwave probing beam. Thus the Stark transitions were obtained with both the selection rules $\Delta M = 0$ and $\Delta M = \pm 1$. Finally, the electric field intensities used in our experiments ranged from 15 to 35 V/cm. The pressures of the pure methyl fluoride ranged from 7 to10 μbar and in the experiments with the methyl fluoride diluted in the helium (x_{He} = 80-95 %), the total pressure range was 100-500 μbar.
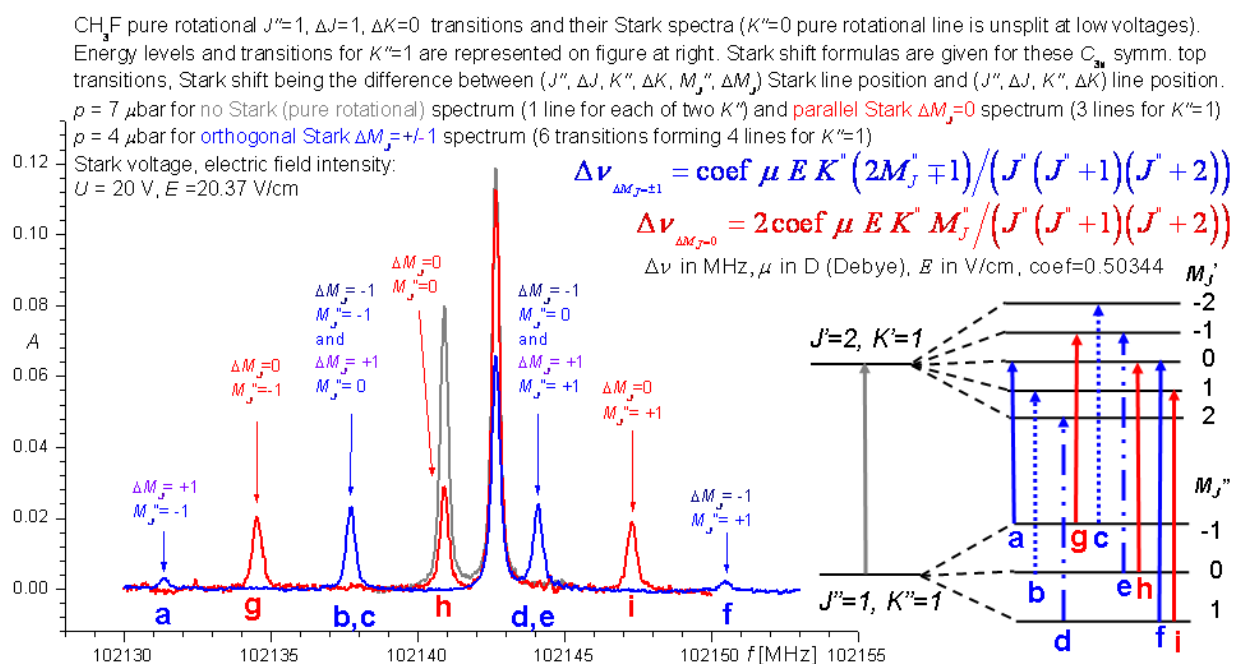
Fig. III.8   Methyl fluoride rotational spectrum and Stark spectrum for orthogonal and parallel orientation

For precise measurements of these separations, the intensity of the static electric field must be as homogenous and stable in time as possible. The better the precision, homogeneity and stability of the electric field intensity makes the better the precision of the electric dipole moment determined possible. In optimal case, the 1σ uncertainty shall not disturb at least four significant digits of the involved quantities. In the laboratory of Prof. Urban at ICT, it is possible to measure using both the parallel and orthogonal Stark effect arrangements. As alredy mentionned, these two designations refer to orientation of the intensity of the electric field between Stark plates towards the orientation of the electric component of the probing beam. By rotating the transmitter parts (multiplier, amplifier) together with detecting part (detector, bias) around the beam axis, it is possible to switch from one regime to the

other one. The two different orientations have the different selection rules for the Stark components they enable to generate.

The symmetry of this class of molecules (symmetrical top) makes that the frequencies of the pure rotational lines are multiples of $J''+1$, the transitions follow rules $\Delta J = 1$, $\Delta K = 0$ and for parallel orientation Stark effect there are $2J''+1$ Stark components. Roughly, $\nu_{\text{rot}}(J'',K'') = 2B(J''+1) - 2D_{J''}(J''+1)^2(J''+2) - 2D_{J''K''}(J''+1)K^2$, where B is a molecular rotational constant and $D_{J''}$, $D_{J''K''}$ are centrifugal distortion constants (inherent to a vibronical state). Note that the individual transition is described by the quantum numbers of the lower (e.g. J'', K'', M'', …) and upper (e.g. J', K', M', …) state involved. The intensity of the initial rotational line is least share of it. The higher rotational number J'' the lesser the maximal Stark shift of the Stark components (see formula in Fig. III.8) and the lesser their intensities (see Eqs. III.11-12).

In the case of the strong Stark field when compared to fine or hyperfine fields, a perturbation method can be used to calculate the Stark splitting. Eq. (III.1) gives the energies of Stark levels (in MHz) up to third order of the perturbation development, the coefficients being specified further:

$$E_{\text{Stark}}(J,K,M) = \sum_{i=1,3} UF^i S_{\text{coef},i} (\mu E)^i E_{\text{coef},i}(J,K,M) , \qquad \text{(III.1)}$$

where the electric field intensity E is in V/cm, dipole moment μ is in D, UF is a unity factor to pass from Debye unit to C.m via statcoulomb.cm for the dipole moment and to pass from V/cm to V/m for the intensity of the electric field:

$$UF = \mu_{\text{coef}} E_{\text{coef}} = \left(10^{-21}/c\right)(100) = 10^{-19}/c , \qquad \text{(III.2)}$$

$$S_{\text{coef},i} = \frac{10^{-6}}{h}\left(\frac{1}{2.10^6\, hB}\right)^{i-1} , \qquad \text{(III.3)}$$

with $c = 299792458$ m/s, $h = 6.62606896\ 10^{-34}$ J.s (*26*), B in MHz..

While evaluating some of the constants, the Eq. (III.1) simplifies to:

$$E_{\text{Stark}}(J,K,M) = X_1(\mu E) E_{\text{coef},1}(J,K,M) + X_2 \frac{(\mu E)^2}{B} E_{\text{coef},2}(J,K,M)$$
$$+ X_3 \frac{(\mu E)^3}{B^2} E_{\text{coef},3}(J,K,M)$$
(III.4)

where $X_1 = 0.50341175$, $X_2 = 0.12671169$, $X_3 = 0.06378816$ and the J, K, M energy level coefficients are given by Eqs. (III.5-10):

$$E_{\text{coef},1}(J,K,M) = -\frac{KM}{J(J+1)}$$
(III.5)

$$E_{\text{coef},1}(0,0,0) = 0$$
(III.6)

$$E_{\text{coef},2}(J,K,M) = \frac{(J^2-K^2)(J^2-M^2)}{J^3(2J-1)(2J+1)} - \frac{((J+1)^2-K^2)((J+1)^2-M^2)}{(J+1)^3(2J+1)(2J+3)}$$
(III.7)

$$E_{\text{coef},2}(0,0,0) = -1/3$$
(III.8)

$$E_{\text{coef},3}(J,K,M) = -MK\left(\frac{(J^2-K^2)(J^2-M^2)}{(J-1)^2 J^5(J+1)(2J-1)(2J+1)} - \frac{((J+1)^2-K^2)((J+1)^2-M^2)}{J(J+1)^5(J+2)(2J+1)(2J+3)} \right)$$
(III.9)

$$E_{\text{coef},3}(0,0,0) = E_{\text{coef},3}(1,0,0) = 0, \ E_{\text{coef},3}(1,1,M) = -M\left(\frac{1-M^2}{3} - \frac{4-M^2}{480}\right)$$
(III.10)

Relative intensities of the Stark components J, K, $M \rightarrow J+1$, K, $M+\Delta M$ ($\Delta M = -1$, 0, 1) are given by Eqs. (III.11-12) :

$$I_{\text{Stark, rel}}(J,K,M,\Delta M = 0) = \frac{(J+1)^2 - M^2}{\sum_M I_{\text{Stark}}(J,K,M,\Delta M = 0)}$$
$$= \frac{(J+1)^2 - M^2}{(2J+1)(J+1)\left(\frac{2}{3}J+1\right)}$$
(III.11)

$$I_{\text{Stark, rel}}(J,K,M,\Delta M = \pm 1) = \frac{(J + \Delta M.M + 1)(J + \Delta M.M + 2)}{\sum_{\Delta M} \sum_{M} I_{\text{Stark}}(J,K,M,\Delta M = \pm 1)}$$

$$= \frac{(J + \Delta M.M + 1)(J + \Delta M.M + 2)}{2\sum_{M} I_{\text{Stark}}(J,K,M,\Delta M = +1)} \qquad \text{(III.12)}$$

$$= \frac{(J + \Delta M.M + 1)(J + \Delta M.M + 2)}{2(2J + 1)(J + 1)\left(\dfrac{4}{3}J + 2\right)}$$

We can also remark that the fastest Stark components (the M components with the highest absolute value of $E_{\text{coef},i}(J,K,M)$ and therefore with the largest Stark shift for given J, K and voltage, i.e. $|M''| = J$ in parallel orientation ($\Delta M = 0$), $M'' = -J$ for $\Delta M = +1$ and $M'' = J$ for $\Delta M = -1$ in orthogonal orientation ($\Delta M = \pm 1$)) are also the least intensive ones.

While it is easy to resolve $J'' = 1$ CH$_3$F Stark lines with Stark field intensities of 20 V/cm (see Fig. III.8) and observe the fastest Stark components as well isolated ($|M_J''| = 1$ for $\Delta M_J = 0$, $M_J'' = -1$ for $\Delta M_J = +1$ and $M_J'' = +1$ for $\Delta M_J = -1$) the situation becomes cumbersome for higher values of the rotational quantum number. Moreover, when the pure rotational lines are split significantly also by other effects (fine, hyperfine) as in $J'' = 12$ Stark lines of CH$_3$Br (see Fig. III.9) where each rotational (J'', K'') line is also split by nuclear quadrupole hyperfine effect to four components (described by quantum number F'').
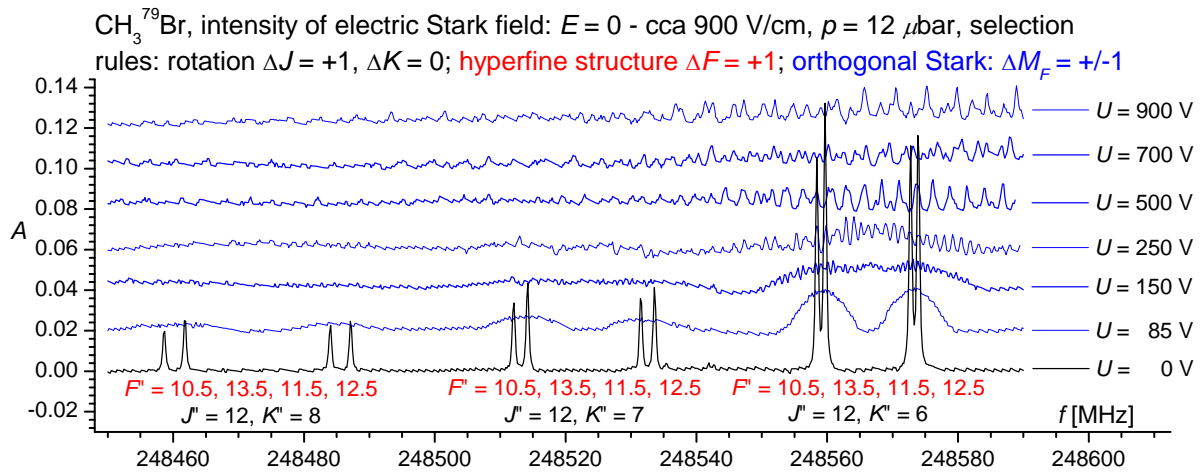
FIG. III.9 Methyl bromide rotational spectrum and Stark spectrum for orthogonal orientation

Calibration of Stark cell

Though the distance that separates the Stark plates may be measured rougly using Vernier caliper, the spectroscopic calibration leads to a more precise effective value. By measuring precisely Stark shifts of Stark components of rotational lines belonging to a species which dipole moment is known precisely and knowing the precise value of electric tension applied to electrodes (i.e. using a precise and stable Voltage generator, e.g. Fluke 5440B featuring 10 ppm output accuracy), we can determine precisely the distance separating the electrodes. The usual calibration molecules are: OCS, CH_3F and CH_3CN. Their electric dipole moments determined by different methods and groups are given in Tables III.1-3, the actually used ones are formatted in bold letters.

Experimental technique	μ [D]		Transition (No Stark Freq. [GHz] / wavenumber [cm⁻¹] / wavelenght [μm])	Comments	Authors	Year	Ref.
OCS							
mw absorption	0.710	(4)			Shulman, Dailey, Townes	1950	(*71*)
	0.7124	(2)	$J=1\rightarrow2$, $\Delta M=0$		Marshall, Weber	1957	(*72*)
MBER	0.71521	(20)	J: $1\rightarrow1$, M_J: $0\rightarrow\pm1$	mean value	Muenter	1968	(*73*)
MW absorption resonant cavity	0.7149	(3)	$(J, M) = (1,0)\rightarrow (2,1)$	least square	Dijkerman, Ruitenberg	1969	(*74*)
MBER (Molecular beam electric resonance)	0.71512	(3)		μ relative to $^{16}O^{12}C^{32}S$	De Leeuw, Dymanus	1970	(*75*)
	1.00031	(2)	J: $1\rightarrow1$, M_J: $0\rightarrow\pm1$, $^{16}O^{12}C^{34}S$				
	1.00017	(2)	J: $1\rightarrow1$, M_J: $0\rightarrow\pm1$, $^{16}O^{13}C^{32}S$				
	0.70423	(3)	(01^10) vibrational state	least square	Reinartz, Meerts, Dymanus	1972	(*76*)
	0.98473	(1)	μ(OCS (01^10))/ μ (OCS (000))				
	0.71519	**(3)**		Revision of Ref. (*75*) value based on change of recommended value of Planck constant: $6.62559(16).10^{-34}$ J.s [(*77*) used in (*75*)], $6.626196(50).10^{-34}$ J.s (*78*) used in (*79*); 2011 recommendation CODATA2006: $6.626\,068\,96(33) \times 10^{-34}$ J s (*26*)	**Reinartz, Dymanus**	**1974**	(*79*)
	0.70433	**(3)**	**(01^10) vibrational state**				
	0.98482	**(2)**	**μ (OCS (01^10))/ μ (OCS (000))**				

Table III.1 Review table of OCS electric dipole moment value determinations

Experimental technique	μ [D]		Transition (No Stark Freq. [GHz] / wavenumber [cm^{-1}] / wavelenght [μm])	Comments	Authors	Year	Ref.
CH$_3$F							
polarization	1.808		–		Smyth,	1934	(*80*)
mw absorption	1.79	(2)	J: 0→1, K = 0, ΔM_J= 0 (51.07 GHz)	mean value, (K-band waveguide Stark cell with a plane electrode)	Ghosh, Trambaluro, Gordy	1953	(*81*)
	1.8555	(15)	J: 1→2, K = 0,1	mean value	Larkin, Gordy	1963	(*82*)
	1.8572	(10)	J: 1→2, K = 0,1 (102.14 GHz); 3→4, K = 0-3 (204.24-27 GHz)	mean value	Steiner, Gordy	1966	(*83*)
IR double resonance	1.9009	(10)	v_3: 0→1, J:12→12,K>2→2	mean value, resonance with P(20) CO$_2$ laser transition, band 001-020, at 1046.8543 cm^{-1}	Brewer	1970	(*84*)
	1.8549	(10)	v_3: 0→0, J:12→12,K>2→2				
MBER	1.8585	(5)	ΔJ = 0, ΔM_J= ±1, (J,K): (1,1), (3,3), (4,4), (5,4)	mean value	Wofsy, Muenter, Klemperer	1971	(*85*)
Laser - Stark, Stark Lamb Dip for 6 lines	1.9054	(5)	69 Stark lines of v3: R(0,0)-R(5,5), Q(1,1)-Q(12,2), P(1,0)-P(5,4)	weighted mean value, CO$_2$ laser P(6)-P(30) lines in the 9.4 μm band, P = 2-20 mTorr	Freund, Duxbury, Römheld, Tiedje,	1974	(*86*)
molecular beam spectroscopy	**1.85840**	**(7)**	ΔM_J **= 1, (J,K): (1, 1)**	**least squares, calibration on OCS (01^{1}0) using μ (OCS (01^{1}0)) = 0.70423(3) D from (*76*), used const. h = 6.626176.10^{-34} J.s, c = 2.99792458.10^8 m/s**	**Marshall, Muenter**	**1980**	**(*70*)**
	1.85842	**(11)**	ΔM_J **= 1, (J,K): (2, 2)**				

Table III.2 Review table of CH$_3$F electric dipole moment value determinations

Experimental technique	μ [D]	Transition (No Stark Freq. [GHz] / wavenumber [cm^{-1}] / wavelenght [μm])	Comments	Authors	Year	Ref.
CH$_3$CN						
mw absorption	3.97	J: 1→2, K = 0, ΔM_J = 0 (36.79 GHz)	mean value	Coles, Good, Hughes	1950	(*87*)
	3.92 (6)	J=1→2 (36.79 GHz)	mean value	Ghosh, Trambaluro, Gordy	1953	(*81*)
	3.913 (2)	J: 1→2, K = 0, 1 ΔM_J = 0, ±1 (36.79 GHz)	mean value	Steiner, Gordy	1966	(*83*)
laser-Stark spectroscopy	3.925191 (48)		least squares , ν_4 ^{12}CO$_2$ P(40)-P(50) and N$_2$O P(18)-P(29) around 10.6 μm, ν_7 ^{12}CO$_2$, P(34)-P(8), and R(8)-R(26) at 9.4 μm, and ^{13}CO$_2$ P(14)-P(26), R(10)-R(24) at 9.8 μm, 550 CH$_3$F Stark lines ΔM = ±1,0; P = 20-23 mTorr	Rackley, Butcher, Römheld, Freund, Oka	1982	(*88*)
	3.929493 (92) ν_7					
	3.935513 (55) ν_4					
	3.9256 (7) CH$_3$C^{15}N		least squares analysis, CO$_2$ and N$_2$O lasers, 650 Stark lines for cca 140 ro-vibrational transitions with J< 34 and K < 11, P = few mTorr	Sakai, Katayama	1984	(*89*)
	3.9354 (7) ν_4, CH$_3$C^{15}N					
saturated absorption mw spectroscopy - Stark Lamb dip	3.9219 (15)	**J: 4→5, K = 1, 2, 3, 4, ΔM_J = ±1, M_I = 0,1; calibration of the cell on CH$_3$F J: 1→2, K = 1 using μ (CH$_3$F)= 1.85840(4) D referenced to (*70*)**	mean value	**Gadhi, Lahrouni, Legrand, Demaison**	**1995**	(*90*)
	3.92196 (12)		least squares analysis			
	3.92197 (13)		**corelated least squares**			
	3.92171 (17)		median (LMS)			

Table III.3 Review table of CH$_3$CN electric dipole moment value determinations

The Stark module used consists of a stable DC voltage generator Fluke 5440B (0 – 1100 V, claimed stability 10 ppm) and of two 150 cm × 8 cm × 1 cm finely polished stainless steel plates placed in a free path glass absorption cell. The separation d of the electrodes by quartz blocks was deduced from measured Stark shifts of the $J = 1 \rightarrow 2$, $K = 1 \rightarrow 1$, $M = -1 \rightarrow -1$ transition at low pressure using an accurate value $\mu = 1.85840(7)$ D (*70*) of the CH$_3$F permanent electric dipole moment. This was done using a relatively low voltage of 40 V creating a (small) shift of -12.741 MHz, leading to $d = 0.9790(9)$ cm, a determination by far accurate enough for the low field measurements used further.

At higher intensities of the Stark electrical field, the experimental spectra of calibration molecules CH_3F and CH_3CN suffered anomalies when confronted to calculations resulting from perturbation method. For both the molecules, it seemed like hyperfine structure is responsive, in term of the frequency position of its components, also to the higher electric field's intensity. Figs. III.10-11 resume the anomalies measured for CH_3CN and CH_3F Stark spectra recorded using in the amplitude and/or frequency modulations in the parallel orientation. The negative and positive M components sharing the same J, K numbers are given for the same voltage in sake of comparison. The pure rotational spectra are shown in the upper parts of the Figs. III.10-11. A consideration of inhomogeneity of the electric field between the Stark plates would explain this observed effect partly only since inhomogeneity would just continuously broaden the Stark lines (most obviously the Stark lines that shift easily) with increasing intensities, diminishing the absorbance peak of the transition for high intensities.

Though the effect of the electric field heterogeneity may be observed in high voltage Stark amplitude modulation spectra of CH_3CN and CH_3F as given in Figs. III.10-11, the frequency modulation spectra suggest that the hyperfine structure components are separating with the external electrical field. These puzzling details of the spectra are not yet explained since apart what seems to be Stark field dependent hyperfine structure, there are also many lines appearing in the spectrum which are not accounted for by perturbation theory calculation.

AM, CH$_3$CN, 0.001-0.020 mbar, J' = 4, K'' = 4-0, pure rotational spectra with hyperfine structure
mw setup: amplifier A425 + doubler D90,
det. WR 8 Radiometer Phys. biased -0.858 V
TC/DT 20/80 ms, 5-10 scans
AM freq. 1 kHz, 0.5ms pulse width
mw source:
-22 dBm (1 μbar, sat.)
-21 dBm (3 μbar)
-20 dBm (5-20 μbar)

for K'' = 4 also FM (magnified):
28 kHz-depth, 50 kHz-DC coupling)
mw source: -14 dBm

p = 20 μbar
p = 15 μbar
p = 10 μbar
p = 05 μbar
p = 03 μbar
p = 01 μbar

Stark spectra ΔM_J = 0: J' = 4, K'' = 3, M_J'' = -3 (on left) and 3 (on right)

U = 760 V, for d = 0.9790 cm: E = 776.3 V/cm, p = 10/15 μbar, 20-25 scans
M_I= 1, calc. Stark f = 91741.974 MHz
M_I=-1, calc. Stark f = 91742.002 MHz
M_I= 0, calc. Stark f= 91742.075 MHz

M_I= 1, calc. Stark f = 92201.786 MHz
M_I=-1, calc. Stark f = 92201.814 MHz
M_I= 0, calc. Stark f = 92201.887 MHz

U = 1030 V, for d = 0.9790 cm: E = 1052.094 V/cm, AM: p = 5/10/15/20 μbar, 25-30 scans
FM: p = 5/10 μbar, 20 scans
M_I= 1, calc. Stark f = 91660.857 MHz
M_I=-1, calc. Stark f = 91660.885 MHz
M_I= 0, calc. Stark f = 91660.958 MHz

M_I= 1, calc. Stark f = 92284.023 MHz
M_I=-1, calc. Stark f = 92284.051 MHz
M_I= 0, calc. Stark f = 92284.124 MHz

Fig. III.10 CH$_3$CN pure rotational and higher voltage Stark AM and FM spectra (identic pressure colour code)

CH$_3$F, parallel Stark orientation, pressure: 3 ubar (25 scans), 5 ubar for 2 transitions
source mw int: -24dBm (65V, sat.)/ -25dBm (other voltages)
transition: J''=1, K''=1, M_J''=-1, ΔM_J=0

U = 40-65 V (from right to left)
E = 40.86-66.39 V/cm
Stark shifts from -12.74 to -19.11 MHz
transition calc. f = 102128.166-102121.798 MHz

U = 40 V
U = 45 V
U = 50 V
U = 55 V
U = 60 V
U = 65 V

U = 500 V, for d = 0.9790 cm: E = 510.73 V/cm, p = 3 μbar, 15-20 scans
Stark line calc. f = 101982.0058 MHz, rot. line calc. f = 102140.905 MHz
Stark shift=-158.900 MHz: S1=-159.2680 MHz, S2=0.3678 MHz, S3=1.0 kHz
AM (upper blue)
FM (lower black)

U = 1075 V, for d = 0.9790 cm: E = 1098.06 V/cm, p = 3 μbar, 20-25 scans
Stark line calc. f = 101800.1885 MHz, rot. line calc. f = 102140.905 MHz
Stark shift=-340.717 MHz: S1=-342.4262 MHz, S2=1.7000 MHz, S3=9.6 kHz
AM (upper blue)
FM (lower black, 0 V/cm red)

Fig. III.11 CH$_3$F Stark parallel AM /FM spectra of one *M* component at lower and higher voltage Stark

IV Line profiles of pure rotational CH₃F lines

IV.1 General considerations

The various types of interactions of electromagnetic (e.m.) radiations with gaseous molecules manifest through specifics shapes of the resulting (absorption, scattering, etc.) spectra. Under sufficient gas density (i.e. pressure/temperature) conditions, these spectra can be significantly influenced by collisional processes occurring in the system.

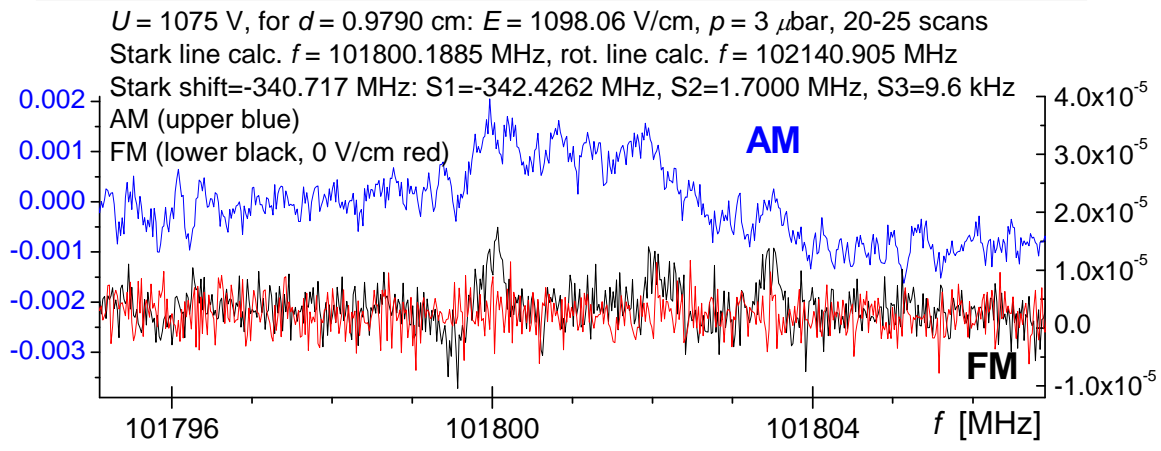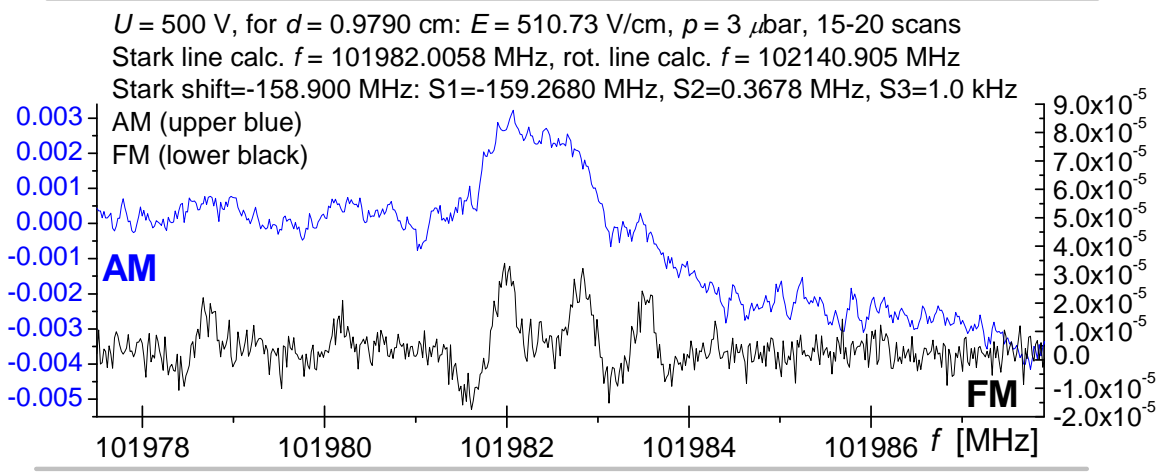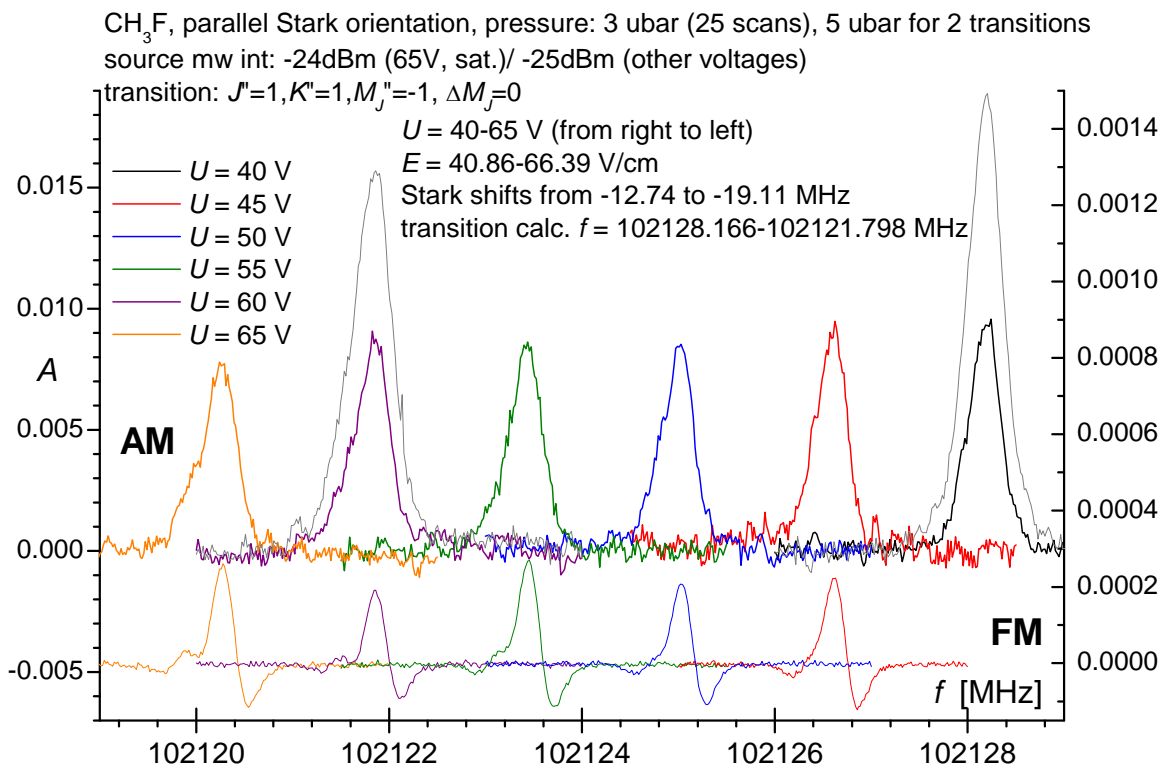The early studies dealing with spectrally isolated optical transitions, overlapping and collisionally coupled lines either in a practical way or through the development of formal theories are reviewed in chapter II. of Ref. (*17*) and thus are not recalled here. Some other models, approximate but amenable to practical calculations and/or useful for analyses and fits of experimental spectra will be presented directly (see also chapter III of Ref. (*17*), rather than the fully general formalism underlying them. From now on, we shall consider molecular gases with the following restrictions, all valid for our studies:

- Neutral molecular species

- Absorption in the spectral domain

- Weak radiation fields (no saturation, no alignment, no high order effects, etc) and non reactive collisions (no chemical reactions)

- Local thermodynamic equilibrium (LTE) so that all populations of energy levels are given by the Maxwell-Boltzmann statistics with equal translational, rotational, and vibrational temperatures.

- The inter-molecular collisions are binary: this approximation, which assumes that a molecule interacts with a single other one at a given time is valid except at very high pressures not considered in this work. The spectral shape then results from the interaction of intrinsic properties of one molecule (called the radiator or absorber) with the e.m. field and with the other particles (perturbers) through binary collisions.

- The "impact approximation" which assumes very short collisions and limits the modeling of the line-shape to the spectral region within a few cm^{-1} (a few ten GHz) around the center of the resonant optical transition.

- In cases where the transitions in the spectrum are spectrally separated (negligible overlapping), the isolated lines approximation is used which neglects the influence of line-mixing studied in chapter V. The absorption then can be computed by simply adding up the individual contributions of the transitions with proper line shapes.

- We assume the dipolar approximation which assumes that the variation of the e.m. field amplitude due to its spatial modulation over the radiator size is negligible and only take into account the contribution of the permanent electric dipole.

IV.1.1 Absorption

In classical electrodynamics a neutral gas (characterized by the scalar relative complex permittivity ε) is polarized (linear macroscopic electric polarization $\vec{\mathbf{P}}$) by the electromagnetic field (of frequency ν, polarization vector $\vec{\mathbf{E}}$ and wave vector $\vec{\mathbf{k}}$) through Maxwell equations:

$$\vec{\mathbf{P}} = \varepsilon_0(\varepsilon - 1)\vec{\mathbf{E}} \quad, \quad \text{with} \quad \varepsilon = \varepsilon' + i\varepsilon'', \tag{IV.1}$$

ε_0 being the vacuum dielectric constant.

For electromagnetic waves travelling through a gas in the z direction, the Beer-Lambert law gives the light intensity $I(\nu,z)$ at frequency ν and depth z:

$$I(\nu, z) = I(\nu, z = 0) \times \exp[-\alpha(\nu)z] \tag{IV.2}$$

where $\alpha(\nu)$ is the absorption coefficient which can be related to the imaginary part of the permittivity through:

$$\alpha(\nu) = \frac{2\pi\nu}{c}\varepsilon''(\nu) \tag{IV.3}$$

Within the dipolar approximation, $\varepsilon''(\nu)$ is the Laplace transform in time of the classical dipole autocorrelation function $C(t)$. Note that, in the following, we shall use frequencies ν instead of angular frequencies ω or wavenumber σ but that conversions are easy to make using the relations $\omega = 2\pi\nu = 2\pi c\sigma$. One can then show that the absorption coefficient is given by (17):

$$\alpha(\nu) = n_a \frac{4\pi^2\nu}{3\hbar c}\left[1 - \exp\left(-\frac{\hbar\nu}{k_B T}\right)\right] \times I(\nu), \tag{IV.4}$$

$$I(\nu) = \text{Im}[i\,\text{F}(\nu)] = \frac{1}{\pi}\text{Im}\left(i\int_0^\infty e^{i\nu t}C(t)\,dt\right), \tag{IV.5}$$

where $\text{F}(\nu)$ is the complex spectral density and $I(\nu)$ is a line profile function.

IV.2 Introduction to isolated lines profiles

As mentioned before, within the isolated lines approximation, the contributions of the various transitions to the spectrum are additive. This disregards the influence of line-mixing treated in following chapter.

Let us consider an optical transition from the initial internal state i to the final state f (i → f) with a corresponding frequency at zero pressure ν_{if} [Hz] (or equivalently wavenumber σ_{if} [m⁻¹] or angular frequency ω_{if} [rad.s⁻¹] with $\nu_{if} = c\sigma_{if} = \omega_{if}/2\pi$). The basic parameters characterizing the line shape are the frequency of its maximum ν_{MAX} thus defining the line shift $\nu_{MAX} - \nu_{if}$ and its full width at half maximum (FWHM). For spectrally asymmetric lines, when their peak is skewed toward higher or lower frequencies while the center of gravity remains the same for both asymmetrical and symmetrical profiles, an additional and convenient asymmetry parameter can be defined, for example by:

$$A = [\nu_{HF} + \nu_{LF} - 2\nu_{Max}]/[(\nu_{HF} - \nu_{LF})/2] \qquad (IV.6)$$

where ν_{HF} and ν_{LF} are the high and low frequencies at half maximum.

Two general types of line broadening may occur in a gas in thermal equilibrium for given temperature and pressure conditions: homogenous broadening and inhomogeneous broadening that, respectively, affect the line identically or not at all frequencies.

One example of inhomogeneous broadening is that due to the Doppler effect through the Maxwell-Boltzmann distribution of absorber velocity $\vec{v}$ given for the volume element $[\vec{v}, \vec{v} + d^3\vec{v}]$:

$$f_{MB}(\vec{v})\, d^3\vec{v} = (M/2\pi k_B T)^{3/2} \exp[-(v/\tilde{v})^2]\, d^3\vec{v}, \qquad (IV.7)$$

where M is the absorber mass, $v = \|\vec{v}\|$ the absorber speed, and $\tilde{v} = (2k_B T/M)^{1/2}$ the most probable speed. Doppler broadening is dominant when collisional processes influencing the line shape are negligible, i.e. at sufficiently low pressures. It is a symmetric broadening.

However, the velocity equilibrium distribution may be altered by the radiator velocity changes due to collisions. Since the collisions favor changes from large velocities to smaller ones, this so-called Dicke effect leads to a narrowing of the line.

IV.2.1 Doppler broadening, Dicke narrowing

We consider here the Doppler effect associated with the velocity $\vec{v}$ and position at time t $\vec{r}(t)$ ($\vec{r}(t) = \vec{v} \cdot t$, $\vec{r}(0) = \mathbf{0}$) of the radiator. It results in a Doppler shift $\nu_{if} v_z/c$ for the absorbed photon frequency (v_z is the radiator velocity component along the e.m. wave propagation vector $\vec{k}$: $v_z = \vec{v}.\vec{k}°$ ($\vec{k}° = \vec{k}/\|\vec{k}\|$, $k = \|\vec{k}\| = 2\pi\nu/c = 2\pi/\lambda$). Because $\pm v_z$ are equally probable, the Maxwell-Boltzmann distribution $f_M(v_z)$ leads to an inhomogenously broadened symmetric profile centered at ν_{if}.

The dipole autocorrelation function $C_{ext}(t)$ resulting from the absorber translational motion (external degrees of freedom) then reads

$$C_{ext}(t) = \left\langle \exp\left(-i\vec{k}[\vec{r}(t)-\vec{r}(0)]\right)\right\rangle = \left\langle \exp\left(-i(\vec{k}.\vec{v})t\right)\right\rangle = \exp\left(-(2\pi\Delta\nu_D t/2)^2\right),$$ (IV.8)

where $\langle...\rangle$ stands for mean value, averaged over all velocities through Maxwell-Boltzmann distribution $f_{MB}(\vec{v})$, $\Delta\nu_D = \dfrac{k\tilde{v}}{2\pi} = \nu_{if}\tilde{v}/c$, $\tilde{v} = \sqrt{2k_B T/M}$, $\tilde{v}$ being the most probable speed. The Doppler profile may be calculated from (IV.8) by using Laplace transform:

$$I_D(\Delta\nu) = \frac{1}{\pi}\mathrm{Im}\left[i\int_0^\infty e^{i\Delta\nu t}C_{ext}(t)\,\mathrm{d}t\right] = \frac{1}{2\pi\sqrt{\pi}\Delta\nu_D}\exp\left(-(\Delta\nu/\Delta\nu_D)^2\right),$$ (IV.9)

where $\Delta\nu = \nu - \nu_{if}$

The Doppler (Gaussian) profile is usually characterized by its half width at half maximum (HWHM) γ_D:

$$\gamma_D = \Delta\nu_D\sqrt{\ln(2)} = \frac{\nu_{if}}{c}\sqrt{\frac{2k_B T\ln(2)}{M}}$$ (IV.10)

$$\gamma_D[\mathrm{MHz}] = 3.5812\times10^{-7}\nu_{if}[\mathrm{MHz}]\sqrt{T[\mathrm{K}]/M[\mathrm{g.mol^{-1}}]}$$

In the Dicke narrowing model, one assumes that the collisions have only a velocity changing (VC) effect. Let $f_{VC}(\vec{v}'\rightarrow\vec{v})$ be the probability per unit time of velocity changing (from $\vec{v}'$ to $\vec{v}$) collisions. These collisions change the Doppler shift from $\nu_{if}.v'_z/c$ to $\nu_{if}.v_z/c$ and therefore change the line shape. Assuming the velocity isotropy of gas and the constancy of the velocity equilibrium distribution and thus the detailed balance principle: $f_{VC}(\vec{v}'\rightarrow\vec{v})f_{MB}(\vec{v}') = f_{VC}(\vec{v}\rightarrow\vec{v}')f_{MB}(\vec{v})$, one has:

$$f_{VC}(v_z\rightarrow v'_z) = f_{VC}(v'_z\rightarrow v_z)\exp\left(\frac{M}{2k_B T}\left(v_z^2 - v'^2_z\right)\right)$$ (IV.11)

From this relation one can conclude that collisions decreasing $|v_z|$ are more probable than those increasing it. This is in favor of the decrease of the absolute value of the Doppler shift $\nu_{if}|v_z|/c$ so that transfers are more probable from the wing of the line to the center rather than vice versa. Hence the signature of this Dicke effect is a reduction of the line width explaining the largely used term of "Dicke narrowing".

The Dicke narrowed profile can be modeled within the diffusional approximation of the thermal motion of the absorber that travels a distance $z(t)$ along the e.m. beam between times 0 and t:

$$C_{\text{ext}}(t) = \left\langle \exp\left(-ikz(t)\right) \right\rangle = \exp[-k^2 < z(t)^2 > /2] \tag{IV.12}$$

The diffusional approximation assumes that $<z(t)^2>=2Dt$ (D is the diffusion coefficient, $[D] = \text{m}^2.\text{s}^{-1}$) which shall apply in cases when the square root of the mean square displacement is small enough when compared to the wavelength λ.

$$C_{\text{ext}}(t) = e^{-k^2 Dt} \equiv C_{\text{ext}}^{\text{Diff}}(t) , \tag{IV.13}$$

where $D \equiv D_0 / P = \int_0^\infty \left\langle \text{v}_z(0)\text{v}_z(t) \right\rangle \mathrm{d}t = \frac{1}{3} \int_0^\infty \left\langle \vec{\text{v}}(0)\vec{\text{v}}(t) \right\rangle \mathrm{d}t$, $\quad$ (IV.14)

where D_0 ($[D_0] = \text{N}$) is the pressure independent value for the diffusional coefficient.

The diffusional profile may be calculated from (IV.13-14) by using Laplace transform:

$$I_{\text{Diff}}(\Delta \nu) = \frac{1}{\pi} \frac{k^2 D_0 / P}{\left(\Delta \nu\right)^2 + (k^2 D_0 / P)^2} \tag{IV.15}$$

This profile has a Lorentzian shape with $k^2 D_0 / P$ as HWHM that decreases with increasing pressure. This conforms the assumption of many collisions to occur to the absorbing molecule before it travels a wavelength.

IV.2.2 Lorentz, Dicke, Voigt, Galatry and Rautian profiles

The Lorentz profile

If the thermal motion, and thus the Doppler effect, is disregarded, the dipole autocorrelation function $C_{\text{int}}(t)$ bound to the absorber internal (rotation, vibration) degrees of freedom reads

$$C_{\text{int}}(t) = \exp\left(-i\left\langle \phi(t) \right\rangle\right) \tag{IV.16}$$

where $\left\langle \phi(t) \right\rangle = \Delta + i\Gamma$ is the averaged collisional phase shift of the radiator dipole for the optical transition, Δ being the frequency shift of the oscillating radiator dipole and Γ its decay rate, hence:

$$C_{\text{int}}(t) = \exp\left(-(\Gamma + i\Delta)t\right) \tag{IV.17}$$

Frequency shift and the decay rate are pressure dependent:

$$\Delta = P\delta, \ \Gamma = P\gamma \ , \tag{IV.18}$$

where δ is the frequency shifting coefficient and γ is the Lorentz broadening coefficient (per unit pressure).

After a Laplace transform of Eq. (IV.17) we obtain the Lorentz profile (*91*):

$$I_{\mathrm{L}}(\Delta\nu) = \frac{1}{\pi} \frac{\gamma P}{(\Delta\nu - \delta P)^2 + (\gamma P)^2} , \tag{IV.19}$$

where $\Delta\nu = \nu - \nu_{\mathrm{if}}$. In the long wavelength region, negative resonances must be taken into account, which leads, for rotational transitions, to the Van Vleck-Weisskopf profile (*92*):

$$I_{\mathrm{VVW}}(\nu) = \frac{1}{\pi}\left(\frac{\nu}{\nu_{\mathrm{if}}}\right)\left\{\frac{\Gamma}{(\nu - \nu_{\mathrm{if}} - \Delta)^2 + \Gamma^2} + \frac{\Gamma}{(\nu + \nu_{\mathrm{if}} + \Delta)^2 + \Gamma^2}\right\} \tag{IV.20}$$

The Dicke profile

Provided that velocity changing collisions do not correlate with dephasing collisions, the correlation function in the diffusional limit stands as:

$$C(t) = C_{\mathrm{ext}}^{\mathrm{Diff}}(t) C_{\mathrm{int}}(t) \tag{IV.21}$$

The Dicke profile (*93*) is then obtained from the Laplace transform of Eq. (IV.21) using Eqs. (IV.13) and (IV.17):

$$I_{\mathrm{Dicke}}(\Delta\nu) = \frac{1}{\pi} \frac{\gamma P + k^2 D_0 / P}{(\Delta\nu - \delta P)^2 + (\gamma P + k^2 D_0 / P)^2} \tag{IV.22}$$

The Voigt profile

The very popular and widely used Voigt profile (*94*) is the convolution of the Lorentz and Doppler profiles (without taking into account Dicke narrowing):

$$\begin{aligned}
I_{\mathrm{Voigt}}(\Delta\nu) &= \int_{-\infty}^{+\infty} I_{\mathrm{D}}\left(\Delta\nu', \nu_{\mathrm{D}}\right) I_{\mathrm{L}}\left(\Delta\nu - \Delta\nu', \Gamma\right) \, \mathrm{d}\Delta\nu' \\
&= \int_{-\infty}^{+\infty} \frac{1}{\sqrt{\pi}\Delta\nu_{\mathrm{D}}} \exp\left(-(\Delta\nu'/\Delta\nu_{\mathrm{D}})^2\right) \frac{1}{\pi} \frac{\Gamma}{(\Delta\nu - \Delta\nu' - \Delta)^2 + \Gamma^2} \, \mathrm{d}\Delta\nu'
\end{aligned} \tag{IV.23}$$

The expression of the Voigt profile can be obtained from the general expression (IV.5) of normalized absorption profile for isolated line, neglecting the velocity changing and speed dependence of Δ and Γ:

$$I_{\mathrm{Voigt}}(\nu) = \frac{1}{\pi} \mathrm{Im} \iiint \frac{f_{\mathrm{MB}}(\vec{\mathbf{v}})}{\nu - \nu_{\mathrm{if}} - \vec{\mathbf{k}}.\vec{\mathbf{v}} - \Delta - i\Gamma} \, \mathrm{d}^3\vec{\mathbf{v}} ,$$

that leads to:

$$I_{\text{Voigt}}(\nu) = \frac{\pi^{-3/2}}{\nu_{\text{D}}} \int_{-\infty}^{\infty} \exp(-t^2) \, \text{Im}\left\{\frac{1}{(\nu-\nu_{\text{if}})/\nu_{\text{D}}+t-\Delta-i\Gamma}\right\} \, dt \tag{IV.24}$$

Using the dimensionless parameters $\tilde{x} = \dfrac{\nu-\nu_{\text{if}}}{\Delta\nu_{\text{D}}}$, $x = \dfrac{\nu-\nu_{\text{if}}-\Delta}{\Delta\nu_{\text{D}}}$ and $y = \dfrac{\Gamma}{\Delta\nu_{\text{D}}}$ the Voigt profile can be also written as:

$$I_{\text{Voigt}}(x, y) = \int_{-\infty}^{+\infty} I_{\text{D}}(\tilde{x}')I_{\text{L}}(x-\tilde{x}', y) \, d\tilde{x}' = \frac{1}{\sqrt{\pi}} \text{Im}\left[i\,w(x, y)\right], \tag{IV.25}$$

where $w(x, y)$ is a complex probability function:

$$w(x, y) = \frac{i}{\pi} \int_{-\infty}^{+\infty} \frac{e^{-t^2}}{x-t+iy} \, dt \tag{IV.26}$$

Note that, using the same dimensionless parameters, the Doppler and Lorentz profiles take the form:

$$I_{\text{D}}(\tilde{x}) = \frac{1}{\sqrt{\pi}} \exp(-\tilde{x}^2) \quad , \quad I_{\text{L}}(x, y) = \frac{1}{\pi}\frac{y}{x^2+y^2} \tag{IV.27}$$

The Galatry profile

The Galatry profile (*95*) is an extension of the Dicke model to the Doppler model that assumes very small velocity changes of the absorber caused by collisions. It is adapted to system involving heavy radiators and light perturbers. The correlation function then takes the form:

$$C_{\text{ext}}^{\text{S}}(t) = \exp\left\{-\frac{1}{2}\left(\frac{\Delta\nu_{\text{D}}}{\nu_{\text{VC}}^{\text{S}}}\right)^2 \left[\nu_{\text{VC}}^{\text{S}}t-1+e^{-\nu_{\text{VC}}^{\text{S}}t}\right]\right\}, \tag{IV.28}$$

where $\nu_{\text{VC}}^{\text{S}}$ is the speed independent VC collision rate in the soft collision model (also called dynamical friction coefficient) that relates to the "optical" diffusion coefficient D by $\nu_{\text{VC}}^{\text{S}} = \dfrac{k_{\text{B}}T}{MD} \equiv \nu_{\text{Diff}}$.

 Assuming the independence of VC and dephasing (broadening/shifting) collisions, the Laplace transform of $C_{\text{int}}(t)C_{\text{ext}}^{\text{S}}(t)$ gives the Galatry profile:

$$I_{\text{G}}(x, y, z) = \frac{1}{\pi} \text{Im}\left\{\int_0^{\infty} i\exp\left[-(ix+y)\tilde{t}+\frac{1}{2z^2}\left(1-z\tilde{t}-e^{-z\tilde{t}}\right)\right] d\tilde{t}\right\}, \tag{IV.29}$$

with $\quad z = \nu_{\text{VC}}^{\text{S}}\big/\Delta\nu_{\text{D}} \quad$ and $\quad \tilde{t} = \Delta\nu_{\text{D}}t$ \hfill (IV.30)

The Rautian profile

The Rautian profile (*96, 97*), also called Nelkin-Ghatak profile or Rautian-Sobelman profile, is a model, which, as the Galatry profile, describes velocity changes. It is a hard collision model, thus conceptually opposite to the soft collision Galatry approach, which assumes that each collision completely thermalyses the velocity. The VC probability density for a $\vec{\mathbf{v}}' \rightarrow \vec{\mathbf{v}}$ collision is thus given by:

$$f_{\mathrm{VC}}^{\mathrm{H}}(\vec{\mathbf{v}}' \rightarrow \vec{\mathbf{v}}) = v_{\mathrm{VC}}^{\mathrm{H}} f_{\mathrm{MB}}(\vec{\mathbf{v}}) \text{ , where} \tag{IV.31}$$

$v_{\mathrm{VC}}^{\mathrm{H}}$ is the speed independent hard collision rate. Assuming the independence of VC and dephasing collisions and considering the pressure broadening, the Rautian profile can be developed as solution for the $f(\vec{\mathbf{v}}, t)$ distribution function which satisfies Boltzmann kinetic equation (see Eq. III.29 in (*17*)):

$$\frac{\partial f(\vec{\mathbf{v}}, t)}{\partial t} = \left[i \left(v_{\mathrm{if}} + \vec{\mathbf{k}}\vec{\mathbf{v}} + \Delta \right) - \left(\Gamma + v_{\mathrm{VC}}^{\mathrm{H}} \right) \right] f(\vec{\mathbf{v}}, t) + \iiint f_{\mathrm{VC}}^{\mathrm{H}}(\vec{\mathbf{v}}' \rightarrow \vec{\mathbf{v}}) f(\vec{\mathbf{v}}', t) \mathrm{d}^3 \vec{\mathbf{v}}' \tag{IV.32}$$

The solution after Laplace transform gives the expression:

$$I_{\mathrm{Raut}}(v) = \frac{1}{\pi} \mathrm{Im} \left\{ \frac{i \iiint \dfrac{f_{\mathrm{MB}}(\vec{\mathbf{v}})}{A(v)} \mathrm{d}^3\vec{\mathbf{v}}}{i - v_{\mathrm{VC}}^{\mathrm{H}} \iiint \dfrac{f_{\mathrm{MB}}(\vec{\mathbf{v}})}{A(v)} \mathrm{d}^3\vec{\mathbf{v}}} \right\}, \tag{IV.33}$$

where $A(v) = v - v_{\mathrm{if}} - \vec{\mathbf{k}}\vec{\mathbf{v}} - \Delta - i(\Gamma + v_{\mathrm{VC}}^{\mathrm{H}})$.

Calculations can thus be performed using the complex probability function introduced for the Voigt profile:

$$I_{\mathrm{Raut}}(x, y, \varsigma) = \frac{1}{\sqrt{\pi}} \mathrm{Im} \left\{ iw(x, y + \varsigma) / \left[1 - \sqrt{\pi} \varsigma w(x, y + \varsigma) \right] \right\}, \tag{IV.34}$$

with $\varsigma = v_{\mathrm{VC}}^{\mathrm{H}} / \Delta v_{\mathrm{D}}$ \tag{IV.35}

The Rautian profile reduces to the Doppler profile when $\Delta = \Gamma = \varsigma = 0$, to the Lorentz profile when $y \rightarrow$ infinity, and to Voigt profile when $\varsigma = 0$.

IV.2.3 Speed dependence

All the models presented above disregard the dependences of the broadening and shifting coefficients on the radiator speed v ($v = \|\vec{\mathbf{v}}\|$) (*98*). Nevertheless, these dependences exist and

generally lead to a narrowing of the line shape, as do the velocity changes modeled in the Rautian and Galatry profiles.

The speed dependent version of the Voigt profile is easily derived and takes the form:

$$I_{\text{sdVoigt}}(\nu) = \frac{1}{\pi} \operatorname{Im} \iiint \frac{f_{\text{MB}}(\vec{\mathbf{v}})}{\Delta \nu - \Delta(\mathbf{v}) - \vec{\mathbf{k}}.\vec{\mathbf{v}} - i\Gamma(\mathbf{v})} \mathrm{d}^3\vec{\mathbf{v}} , \qquad (\text{IV.36})$$

which can be developed, as shown in Appendix, in

$$I_{\text{sdVoigt}}(\nu) = \frac{\pi^{-3/2}}{\nu_{\text{D}}} \int_{-\infty}^{\infty} \exp(-t^2) \operatorname{Im}\left\{ \frac{1 - z'(t)}{x + t - z(t)} \right\} \mathrm{d}t , \text{ where} \qquad (\text{IV.37})$$

$$x = \frac{\nu - \nu_0}{\nu_{\text{D}}}$$

$$z'(t) = \frac{\Delta'(\tilde{\mathbf{v}}t)}{\nu_{\text{D}}} + i\frac{\Gamma'(\tilde{\mathbf{v}}t)}{\nu_{\text{D}}}$$

$$z(t) = \frac{\Delta(\tilde{\mathbf{v}}t)}{\nu_{\text{D}}} + i\frac{\Gamma(\tilde{\mathbf{v}}t)}{\nu_{\text{D}}}$$

Note at this step that the quadratic law of Rohart (*99*) is convenient for fits of measured spectra and has been widely used for this purpose. Its expression is

$$\Gamma(\tilde{\mathbf{v}}t) = \Gamma_0 + (t^2 - 1.5)\Gamma_2$$
$$\Gamma'(\tilde{\mathbf{v}}t) = 2t\Gamma_2 \qquad\qquad (\text{IV.38})$$

The speed dependent generalization of the Rautian profile has the form:

$$I_{\text{sdRaut}}(\nu) = \frac{1}{\pi} \operatorname{Im}\left\{ \frac{i\iiint \dfrac{f_{\text{MB}}(\vec{\mathbf{v}})}{A(\vec{\mathbf{v}},\nu)}\mathrm{d}^3\vec{\mathbf{v}}}{i - \nu_{\text{VC}}^{\text{H}}\iiint \dfrac{f_{\text{MB}}(\vec{\mathbf{v}})}{A(\vec{\mathbf{v}},\nu)}\mathrm{d}^3\vec{\mathbf{v}}} \right\}, \qquad (\text{IV.39})$$

where $A(\vec{\mathbf{v}},\nu) = \nu - \nu_{\text{if}} - \vec{\mathbf{k}}\vec{\mathbf{v}} - \Delta(\mathbf{v}) - i(\Gamma(\mathbf{v}) + \nu_{\text{VC}}^{\text{H}})$.

Note that, for $\nu_{\text{VC}}^{\text{H}} = 0$, the speed dependent Voigt profile is, of course, obtained. Indeed

$$\text{if } \nu_{\text{VC}}^{\text{H}} = 0, \text{ then } I_{\text{sdRaut}}(\nu) = \operatorname{Im}\left\{ \iiint \frac{f_{\text{M}}(\vec{\mathbf{v}})}{A(\vec{\mathbf{v}},\nu)}\mathrm{d}^3\vec{\mathbf{v}} \right\} = \operatorname{Im}\left\{ \iiint \frac{f_{\text{M}}(\vec{\mathbf{v}})}{A(\nu)}\mathrm{d}^3\vec{\mathbf{v}} \right\} = I_{\text{sdV}}(\nu) \quad (\text{IV.40})$$

One can easily show that the Dicke effect (due to velocity changes) vanishes at elevated pressures, when the collisional width gets much larger than the Doppler one. For instance, in the absence of speed dependence, the Rautian and Galatry profiles tend toward a Lorentz shape. On the opposite, speed dependence effects remain whatever the pressure.

Hence, although the speed dependence and Dicke narrowing have similar spectral effects, it is, in principle, possible to differentiate them experimentally provided that the investigated pressure range goes from the nearly Doppler to the collisional regime, i.e. from conditions for which the Doppler broadening is dominant to negligible.

IV.3 Case of CH$_3$F

IV.3.1 Introduction

While treating the measured pure rotational spectra for the line-mixing study presented in the next chapter, the detailed analysis of the fit residuals showed that the observed profiles of the lines, when isolated, are slightly narrower than their Voigt fits, as demonstrated by the W shaped residuals in Figs. IV.1 and IV.2.
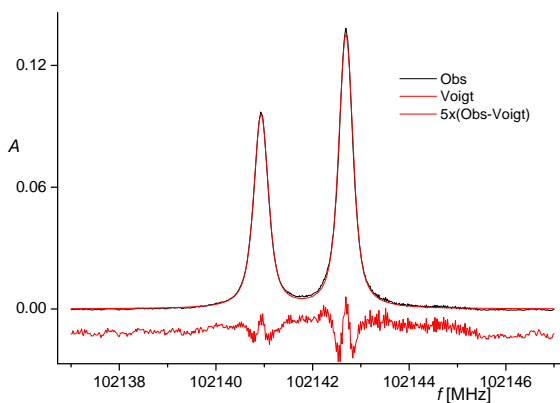

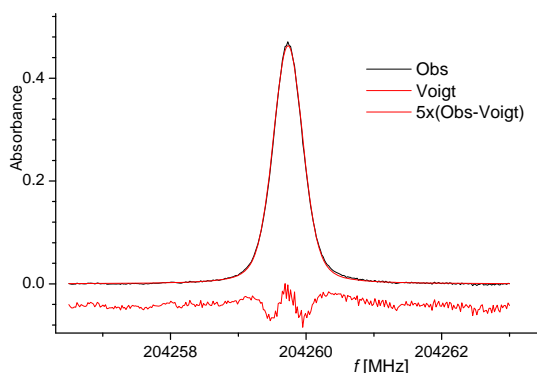**Fig. IV.1 Voigt profile residuum, CH$_3$F J: 1→2, K = 0-1, pressure 7 μbar.**

Fig. IV.2 Voigt profile residuum, CH$_3$F J = 3→4, K = 2, pressure 7 μbar.

As recalled above, this narrowing, which has been observed for many molecular systems (*17*), may results from velocity changes (Dicke effect), from the speed dependence, or from simultaneous contributions of these two processes. Note that, for CH_3F in the microwave, line narrowing has been studied, to the best of our knowledge, in Ref. (*99*) only. In this work, the $J = 1$ $K = 1$ CH_3F pure rotational transition has been studied in a time domain experiment and its narrowing has been attributed to the speed dependence of the broadening coefficient only, thus a priori disregarding any Dicke effect.

IV.3.2 Analysis

It shall be reminded that the presented analysis was carried out as a first trial study of narrowing processes in pure rotational absorbance spectra of CH_3F. The measured spectra were fitted line by line, first using the Rautian profile and the speed dependent Voigt profile presented in Sec. IV.2. As shown by Figs. IV.3-4 this leads to very significant improvements of the fits qualities with respect to what is obtained when a purely (speed independent) Voigt profile is used. Furthermore, the fits residuals obtained with these two more refined models are very good and comparable thus not permitting, at this step, any conclusion on the mechanism(s) truly involved. In fact, recall that the narrowing obtained with the Rautian and SDV profiles originate from completely different processes, i.e. the velocity changes (Rautian) and the speed dependence of the broadening coefficient (SDV).
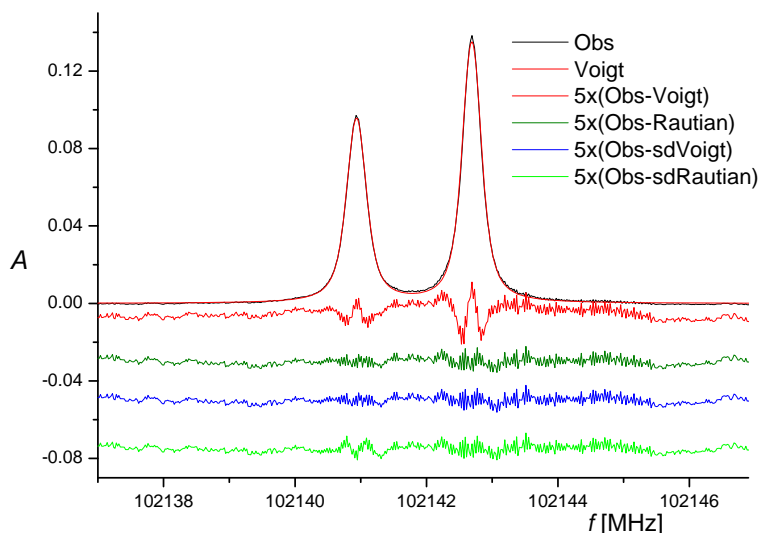

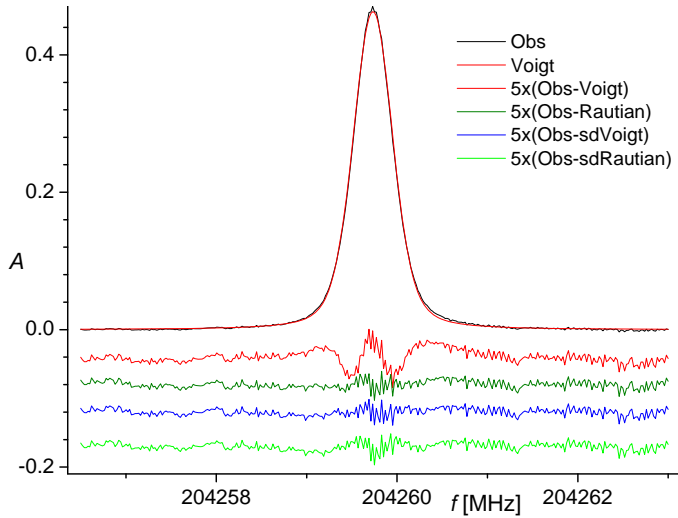**Fig. IV.3 Residuals of Voigt, Rautian and their speed dependent profiles, CH₃F, *J*: 1→2, *K* = 0-1, *p* =7 μbar.**

Fig. IV.4 Residuals of Voigt, Rautian and their speed dependent profiles, CH₃F, *J* = 3→4, *K* = 2, *p* = 7 μbar.

Although measured spectra were available in the range from about 5 to 250 μbar, only those for the lowest pressures (below about 30 μbar) were used since, for higher pressures, the fitting procedure either failed to converge or converged to physically meaningless values. This could be expected for the Rautian profile since it tends to a Voigt profile at elevated pressure forbidding a fit of the narrowing parameter. It is more unexpected for the speed dependent Voigt shape and the reason for this problem remains unclear but may be due to uncertainties and noise on the measurements. Further studies are needed to clarify this point. Nevertheless, Table IV.1 gives the values of the parameters obtained from these fits. As can be seen, the only possible comparison with previous values is reasonable.

J *K*	Voigt				sd Voigt								Rautian				sdRautian Γcalc		
	this study		Ref. (*99*)		this study				Ref. (*99*)										
	Γ	unc	Γ multifit	Γ	unc	Γ_0	unc	Γ_2	unc	Γ_0	unc	Γ_2	unc	Γ	unc	ν_{VC}^{H}	unc	Γ_{calc}	ν_{VC}^{H} unc
1 0	20.2	0.7	20.5			22.5	0.1	4.5	0.5					22.4	0.4	10.2	1.2	20.1	0.98 0.05
1	19.6	1.5	21.0	17.98	0.4	20.6	0.7	1.3	0.2	18.3	0.4	3	1	20.5	0.6	3.9	0.8	18.6	1.03 0.09
3 0	20.4	1.7	18.8			21.2	0.3	3.7	0.5					20.2	0.4	7.7	2.1	17.0	1.18 0.04
1	18.2	0.4	19.1			19.6	0.6	2.5	0.4					19.0	0.4	5.0	0.4	16.8	1.10 0.05
2	17.6	0.4	18.4			19.7	0.4	3	0.1					18.9	0.2	5.6	0.8	16.0	1.12 0.05
3	17.1	0.3	16.2			17.9	0.4	1.5	0.1					17.5	0.3	2.8	0.5	14.1	1.23 0.08

Table IV.1 Collisional parameters in [MHz/Torr] of CH₃F pure rotational lines for various profiles (1 σ uncertainties).

In order to go further and to try to differentiate between the contributions of Dicke (through ν_{VC}^{H}) and speed dependent (through the Γ_0, Γ_2 parameters) effects, a speed dependent Rautian profile was set up. Since attempts to simultaneously derive (fit) from experiments the velocity changing and speed dependence parameters failed due to the strong correlation between these two unknown quantities an alternative procedure was used. In fact, in order to constrain the model, the speed dependent broadening coefficients $\Gamma(v_a)$ and its derivative $\dfrac{d\Gamma(v_a)}{dv_a}$ were fixed to values calculated with a semi-classical model adapted to CH$_3$F from the method proposed for linear molecules by Bonamy *et al.* (*100*). These calculations, made with a program kindly communicated by Pr. Christian Boulet, provide the broadening cross section $\sigma_\Gamma(v_r)$ as a function of the the relative speed $v_r = \|\vec{v}_r\|$ with $\vec{v}_r = \vec{v}_p - \vec{v}_a$ being the relative velocity between the perturber and the absorber. Assuming a Maxwell-Boltzmann distribution for the perturber velocity, the values of $\Gamma(v_a)$, thus now versus the speed of the absorbed only, were calculated using the following relation (see Eqs. III.54-55 in (*17*)):

$$\Gamma(v_a) = \left(\tilde{v}_p \sqrt{\pi} \right)^{-3} \iiint \exp\left(-\left(\frac{v_p}{\tilde{v}_p} \right)^2 \right) \sigma_\Gamma(v_r) \, d^3\vec{v}_p \,, \tag{IV.41}$$

where $d^3\vec{v}_p = d^3\vec{v}_r$ and $\tilde{v}_p = \sqrt{\dfrac{2k_{MB}T}{M_p}}$. After integration over the orientation, Eq. (IV.41) transforms to:

$$\Gamma(v_a) = \frac{2}{v_a \tilde{v}_p \sqrt{\pi}} \int_0^{+\infty} v_r \exp\left(-\frac{v_a^2 + v_r^2}{\tilde{v}_p^2} \right) sh\left(\frac{2v_a v_r}{\tilde{v}_p^2} \right) \sigma_\Gamma(v_r) \, dv_r \tag{IV.42}$$

The calculation of $\Gamma(v_a)$ for values of v_a up to $6\tilde{v}_a$ ($\tilde{v}_a(T = 296\text{ K}) = 380$ m/s) leads to the values presented in Fig. IV.5 for the transitions under study in this work.
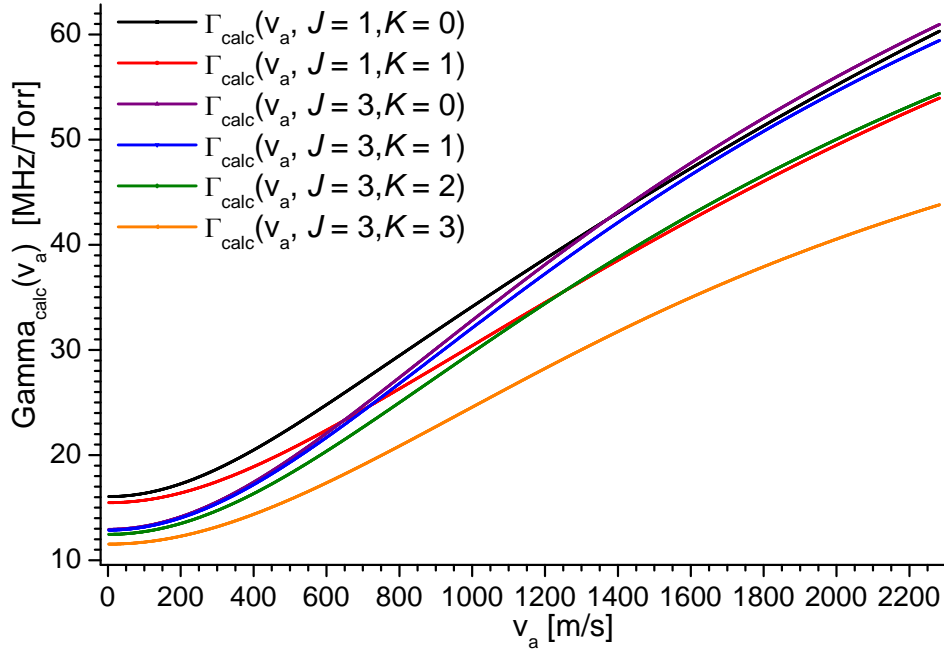
Fig. IV.5 Speed dependent broadening coefficients ($T = 296$ K): calculated values for $J = 1$ and 3 CH$_3$F lines

For practical reasons, these raw values of $\Gamma(v_a)$ were fitted with polynomial whose derivatives were afterwards used for calculation of $\dfrac{d\Gamma(v_a)}{dv_a}$ needed in the calculation of the line shape [see Eq. (IV.37)].

Since these two quantities are now fixed, the only line shape parameter adjusted parameter in the fit of measured spectra [through the numerical integration of Eq. (IV.33)] is the Rautian parameter v_{VC}^{H}. This parameter, after normalization by pressure, thus in MHz/Torr, should be constant and in this property is not obtained from our spectra in the low pressure conditions as shown in Fig. IV.6. On the opposite, above about 20 mTorr nearly pressure independent values are obtained, consistently with expectations. This is a quite promising result that needs confirmations and further analysis using improved measurements, a possible continuation of this thesis work.
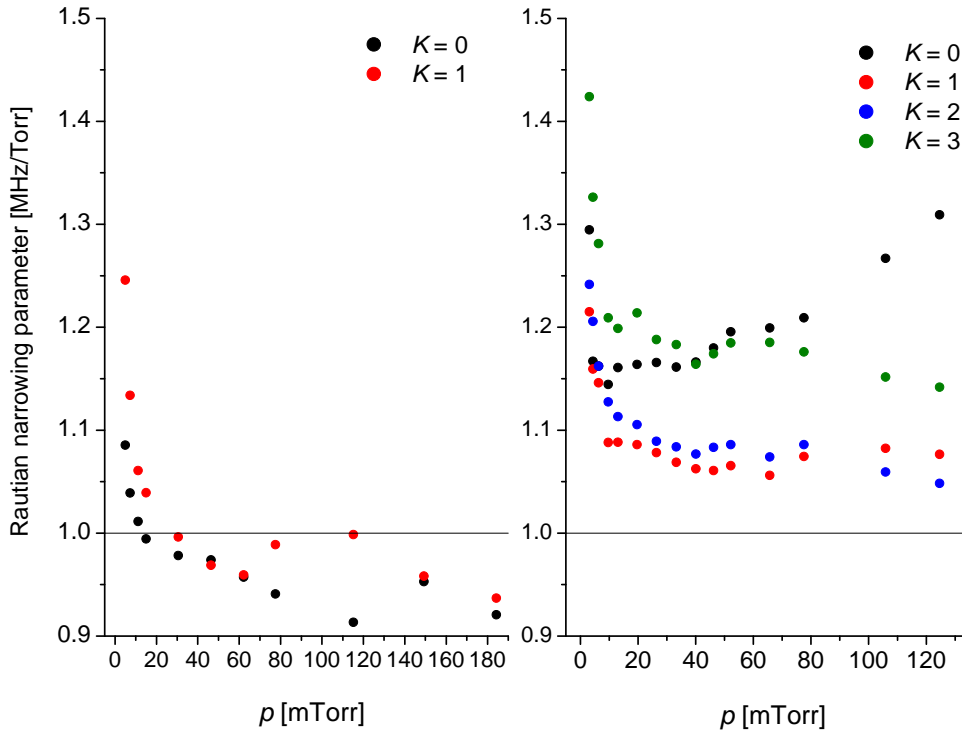
Fig. IV.6 Rautian narrowing parameter ν_{VC}^{H} in [MHz/Torr] in the Rautian speed dependent profile with calculated $\Gamma(v)$ for $J = 1$ lines (left) and $J = 3$ lines (right).

IV.3.3 Conclusion

The pure rotational lines of CH_3F were studied using Voigt profile and other more subtle profiles as speed dependent Voigt profile, Rautian profile and speed dependent Rautian profile. Speed dependent Voigt profile and Rautian profile flattened significantly the residual of the Voigt profile. On the other hand, the results using in part calculated in part fitted parameters in the speed dependent Rautian profile did not help to conclude on the impact of involved narrowing contributors since it seemed that for low pressures the profiles were overnarrowed or did not really differ from the previous models (Rautian and speed dependent Voigt, see $J = 3$ $K = 0$ transition of Fig. IV.4). The quality of experimental data is probably at the origin of failure in using speed dependent Rautian profile. The pure rotational lines have been measured in Stark cell with relatively short path length in order to evaluate the fine subtleties of the line profiles. Therefore the study will be repeated using a longer, non Stark, free path absorption cell (see Figs. III.2-3). Also, rather then a line by line fit, a multifit could be used to retrieve the collisional parameters.

V Line-mixing among CH₃F Stark lines

V.1 Introduction to collisional line mixing

When the contributions, to the absorption spectrum, of different transitions overlap significantly due to their broadening by pressure, the lines often cannot be considered as (collisionally) isolated (chapter IV of Ref. (*17*)). If the overlapping transitions are coupled to each other through collisions, the spectrum is not the sum of the contributions of the individual lines because of the collisional line mixing effect which leads to intensity transfers among the various coupled transitions. The line-mixing mechanism can be explained by considering the (simple) example of two absorption ($\Delta J = 1$) Stark lines ($\Delta M = 0$) of a symmetrical top that differ only by their M quantum number, centered at ν_{if} for the transition $J, K, M \rightarrow J+1, K, M$ and at $\nu_{i'f'}$ for the transition $J, K, M' \rightarrow J+1, K, M'$.   In the presence of radiation, a molecule in the level $i = J, K, M$ can be excited to level $f = J+1, K, M$ by absorbing a photon of frequency ν_{if}, thus generating, in the spectrum, an absorption line at frequency ν_{if}. The molecule can also be transferred through collision to the level $i' = J, K, M'$, wherefrom it can be excited to level $f' = J+1, K, M'$ by absorbing a photon of frequency $\nu_{i'f'}$, thus contributing to the absorption line at frequency $\nu_{i'f'}$ and then it can relax from level $f' = J+1, K, M'$ to $f = J+1, K, M$ by collisions (blue arrows on Fig. V.1). Through this process, a molecule initially on level i can contribute to the absorption line at frequency $\nu_{i'f'}$. The reverse path is also possible (collisional transfer from $i' = J, K, M'$ to $i = J, K, M$, absorption at ν_{if} and collisional relaxation from $f = J+1, K, M$ to $f' = J+1, K, M'$) as showed on Fig. V.1 by red arrows.
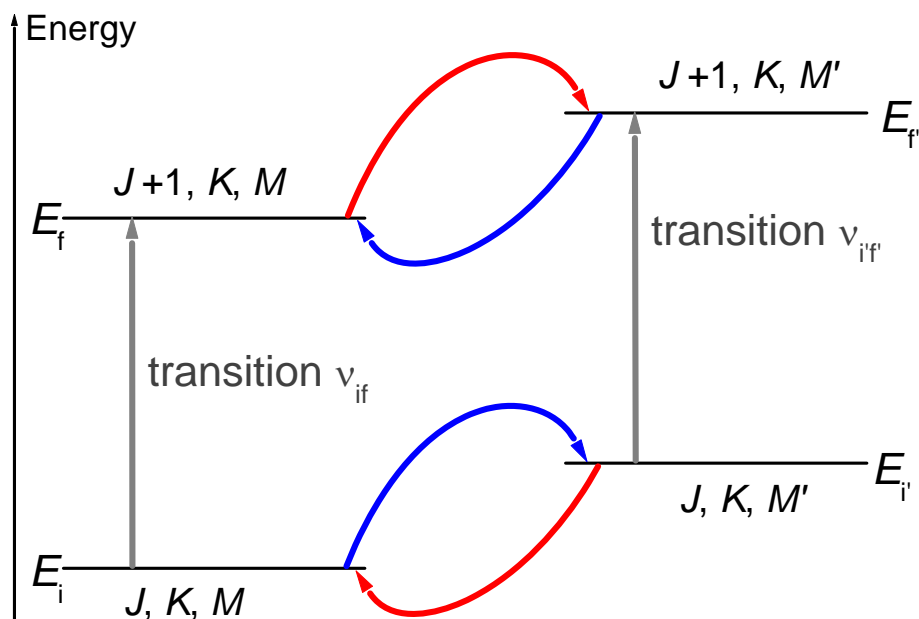
Fig. V.1 Scheme of line mixing process among two ΔM=0 Stark lines

In summary, collisional line-mixing leads to exchanges of populations between energy levels of the considered absorption transitions and this manifests, in the spectrum, through the fact that the absorption lines partially exchange their intensities.

For this effect to occur and to significantly affect absorption by pure rotational transitions (vibrational ground state), the following conditions must be fulfilled. First, collisional transfers between levels $i \leftrightarrow i', f \leftrightarrow f'$ must be permitted: levels must thus belong to the same isotopologue and be "connectable" considering their symmetries and the inter-molecular potential. For instance, within the model presented thereafter, the $\Delta M = -1$ and $\Delta M = +1$ optical transitions in Stark orthogonal orientation spectra are not coupled by collisions. Secondly, radiator-perturber interactions inducing $i \leftrightarrow i', f \leftrightarrow f'$ transfers must be efficient. One may thus disregard transfers between levels belonging to different vibrational states (or having different nuclear spins); indeed the collisional transfers between such levels are very slow and several orders of magnitude less efficient that pure rotational transfers. Finally, the populations' exchanges must have a significant effect on the spectrum itself. Recalling that the pressure broadening is some kind of measure of the effect of molecular interactions, a criterion is thus that the collisional widths of the interacting lines should be comparable or greater than the distance between line centers ($\Gamma_{if} \approx /> |\nu_{if} - \nu_{i'f'}|$).

Since the equilibrium Maxwell-Boltzmann population distribution applies in collisions, the detailed balance principle relates the exchange terms:

$$P(i \rightarrow i')\rho(i) = P(i' \rightarrow i)\rho(i'), \quad (V.1)$$

where $P(i \rightarrow i')$ is probability of transition from i to i' and $\rho(i)$ is the equilibrium relative population of the initial level of line ν_{if}. The detailed balance indicates that more probable is the process starting from the less populated level. Therefore line-mixing promotes the transfer of intensity from the weak lines to the strong lines. More generally this leads to transfers from the weak to the strong absorption regions. In comparison with shapes of isolated lines, line-mixing leads to a narrowing of profile.

V.1.1 Absorption coefficient and widths

In the following, we assume binary collisions (valid at the pressures considered in this work), we disregard the Doppler effect (which can be easily introduced through a convolution by the proper Gaussian profile), and work within the frame of the "impact approximation" (valid since we consider regions close to the line centers). With these assumptions, the normalized spectral profile of a band composed of rotational components broadened and coupled by molecular collisions is given by Refs. (*17, 101*):

$$F(\nu) = \frac{1}{\pi} \text{Im} \sum_{\ell,\ell'} \rho_\ell d_\ell d_{\ell'} \left\langle \ell' \left| \frac{1}{\nu - \mathbf{L_0} - i\mathbf{W}} \right| \ell \right\rangle \quad (V.2)$$

For each optical transition ℓ, d_ℓ is its reduced dipole transition matrix elements and ρ_ℓ is the relative population of its initial level. $\mathbf{L_0}$ is a diagonal matrix, in the line (Liouville) space, containing the unperturbed line frequencies ν_ℓ. $\mathbf{W}$ is the relaxation matrix, which is, within the binary collision approximation, proportional to the gas density (or total pressure P). Its diagonal elements are related to the pressure induced width Γ_ℓ and spectral shift Δ_ℓ of the individual lines:

$$\langle \ell | \mathbf{W} | \ell \rangle = \Gamma_\ell - i\Delta_\ell = P(\gamma_\ell - i\delta_\ell) \quad (V.3)$$

The off diagonal elements of **W** describe the couplings between the various transitions and they are responsible for the LM process. From now on, the imaginary part of **W** will be neglected. This is required in the absence of any model to construct them and this approximation is likely valid in view of the small pressure induced shifts. Knowing **W**, the collisional profile is obtained from the diagonalization of **L₀**+i**W** (*17, 102*) and it can be convolved by a Gaussian function in order to take the Doppler effect into account, if necessary.

Two asymptotic behaviors will be of primary importance for the analysis of the results in section V.2. The first is the (very) weak overlapping regime when the widths of the pressure broadened transitions are negligible when compared with the spectral distances between absorption lines $[\Gamma_\ell <<| \nu_\ell - \nu_{\ell'} | \quad \forall \ell, \ell' \neq \ell]$. The collisional profile of Eq. (V.2) then becomes the sum of "isolated" Lorentzian contributions:

$$F(\nu) = \frac{1}{\pi} \sum_\ell \rho_\ell d_\ell^2 \frac{\Gamma_\ell}{\Gamma_\ell^2 + (\nu - \nu_\ell)^2} \quad . \tag{V.4}$$

In the opposite case, i.e. for a group of completely overlapping lines $[\Gamma_\ell >>| \nu_\ell - \nu_{\ell'} | \quad \forall \ell, \ell' \neq \ell]$, the profile corresponds to that of a single "effective line" with a Lorentzian shape:

$$F(\nu) = \frac{\overline{S}}{\pi} \frac{\overline{\Gamma}}{\overline{\Gamma}^2 + (\nu - \overline{\nu})^2} \, , \tag{V.5}$$

where the intensity, frequency and width of this "effective" line are given by :

$$\overline{S} = \sum_\ell \rho_\ell d_\ell^2 \, , \quad \overline{\nu} = \frac{1}{\overline{S}} \sum_\ell \rho_\ell d_\ell^2 \nu_\ell \quad \text{and} \quad \overline{\Gamma} = \frac{1}{\overline{S}} \sum_{\ell, \ell'} \rho_\ell d_\ell d_{\ell'} \operatorname{Re}\{W_{\ell'\ell}\} . \tag{V.6}$$

Equation (V.6) shows that the line width of a bunch of completely overlapping collisionally coupled transitions is different from the weighted average of the widths of the isolated components, the latter being given by:

$$\Gamma^{WA} = \frac{1}{\overline{S}} \sum_\ell \rho_\ell d_\ell^2 \operatorname{Re}\{W_{\ell\ell}\} . \tag{V.7}$$

In fact, $\overline{\Gamma}$ is generally smaller (*17*) than Γ^{WA} because of a usually negative coupling term $\overline{S}^{-1} \sum_{\ell} \sum_{\ell' \neq \ell} \rho_{\ell} d_{\ell} d_{\ell'} \mathrm{Re}\{W_{\ell'\ell}\}$ that must be taken into account. Note that Γ^{WA} is the width of the "effective" line obtained from Eq. (V.4) in the strongly overlapping case and that it is thus the value associated with the neglect of LM effects.

In the present study we consider individual Stark transitions associated with given values of the rotational quantum numbers *J* and *K*, i.e.: $J, K, M \rightarrow J+1, K, M' = M + \Delta M$. The sums over ℓ and ℓ' in Eq. (V.2) thus become sums over *M* and *M'*. As shown in (*13*) and (*14*), and as can also be established from the IOS formalism of (*12*) and Sec. V.2.2, collisional coupling can arise only between lines having the same value of ΔM. The problem thus reduces to the three subspaces corresponding to the three possible values ($0, \pm 1$) of ΔM. Consequently $\Gamma_{\ell} \rightarrow \Gamma_{JKM}^{\Delta M}$ is the width of an isolated Stark component while $\overline{\Gamma} \rightarrow \overline{\Gamma}_{JK}$ is the width of the $J, K \rightarrow J+1, K$ rotational line when unresolved, i.e. in the zero field limit (recall that the distance between *M*-components is driven by a first order Stark effect with a constant spacing − for given values of *J* and *K* − linear in the field). Finally, the weighted average of the widths of the Stark components [see Eq. (V.7)] will be noted Γ_{JK}^{WA}.

V.1.2 Construction of the relaxation matrix

The models available to build collisional relaxation matrices within the impact and binary collision approximation range from simple empirical approaches for complex molecular systems to fully quantum calculations starting from the intermolecular potential energy surface (PES) for simple systems. With the exception of direct calculation from the PES, the models provide calculations only of the real part of the relaxation matrix.

Note at this step that one can show that the relaxation matrix **W** verifies the following properties:

1) The diagonal elements of **W** are the individual pressure-induced widths and shifts of the optical transitions (Eq. (V.3))

2) **W** satisfies the detailed balance principle which ensures the overall conservation of the populations ρ_{ℓ} of the levels

$$\langle \ell' | \mathbf{W} | \ell \rangle \rho_{\ell} = \langle \ell | \mathbf{W} | \ell' \rangle \rho_{\ell'} \qquad (V.8)$$

3) For rigid rotors and intermolecular interactions only dependent on the rotational states (i.e. no dependence on vibration), $\mathbf{W}$ verifies the following sum rule:

$$\sum_{\ell'} d_{\ell'} \langle \ell' | \mathbf{W} | \ell \rangle = 0 \iff -\frac{1}{d_\ell} \sum_{\ell' \neq \ell} d_{\ell'} \langle \ell' | \mathbf{W} | \ell \rangle = \Gamma_\ell(T) - i\Delta_\ell(T) \tag{V.9}$$

The numerous models for the construction of $\mathbf{W}$ are detailed in (*17*) and are (very) briefly recalled below.

- The simplest is a partly empirical approach based on the hard collision model where the off diagonal real elements are proportional to the relative population of the initial level:

$$\langle \ell' | \mathbf{W} | \ell \rangle = -\rho_{\ell'} \times \overline{\gamma}, \ell' \neq \ell \tag{V.10}$$

It has been largely used in the past when computer power was limited and more sophisticated models were not available, which is not the case anymore.

- Another type of phenomenological models uses statistically based energy gap fitting laws (*103*). In energy gap models, the real elements of $\mathbf{W}$ are expressed by state-to-state collisional transfer quantities between initial levels $K(\text{i'} \leftarrow \text{i})$ that are represented as functions of energy gap $\Delta E_{\text{i'i}} = |E_\text{i} - E_{\text{i'}}|$ in the statistical fitting law approach:

$$\langle \ell' | \mathbf{W} | \ell \rangle = K(i' \leftarrow i) = f_{\text{EG}}(E_i - E_{i'}) \text{ for } E_i \geq E_{i'}, \tag{V.11}$$

where $f_{\text{EG}}(\Delta E)$ is usually a power or exponential function ($a_1 |\Delta E|^{-a_2}$, $a_1 e^{-a_2 |\Delta E|}$, $a_1 |\Delta E|^{-a_2} e^{-a_3 |\Delta E|}$, …) which parameters are obtained through fits of experimental data. Such models have the advantage of easy implementation but have limited extrapolation possibilities since they rely on experimental data.

- The dynamically based scaling laws, which were originally introduced to model collisions with atoms, have more robust physical bases since they explicitly take into account the couplings of the various (spectroscopic and collisional) angular momenta. The first of these models is based on the so-called Infinite Order Sudden (IOS) approximation (*104*) and assumes instantaneous collisions to disregard the molecules rotation during collisions. Its main interest is that this model separates spectroscopic effects dependent on the internal states of the absorber (described by angular momenta coupling terms) and dynamical effects dependent on absorber-perturber interactions (described by a set of collisional quantities). Nevertheless, the IOS neglecting of the energy spacing between rotational levels leads to the breakdown of the detailed balance relation of Eq. (V.8) and to inaccurate results when collisions are "slow" (for relatively heavy molecular pairs). To correct for these limitations,

the Energy corrected Sudden (ECS, (*19*) model was proposed later on, which improves the IOS by imposing the detailed balance condition and including the collisional effects of the finite duration of collisions. The resulting approach has enabled very satisfactory predictions of line-mixing in a large variety of spectra for many molecules including linear and symmetric-top species (see review in (*17*)). Note that, for Stark components in which all *M* sub-levels have the same rotational energy and population, the IOS model, used in the following, is identical to the ECS approach.

Among approaches based on knowledge of the intermolecular potential, the fully quantum ones are the most accurate and they are considered as essentially exact. Nevertheless, in spite of the considerable increase of computer power, they are still hardly applicable to complex molecular pairs and limited to simple system and/or low temperatures. The alternative is to use a semi-classical treatment in which the translation is treated classically while the internal states are treated quantum mechanically. Among these approaches, the Neilsen and Gordon model (*105*) is considered most sophisticated but limited to interactions between linear molecules and atoms. The Anderson-Tsao-Curnutte (ATC, (*16, 106*) model enables to treat more complex collisional pairs and the Robert-Bonamy (*100*) model extends the ATC approach with a better description of close collisions. Note that a model derived from the ATC approach was applied previously to line-mixing among Stark components as discussed below.

V.2 Case of Stark components of CH_3F and CH_3F in He

V.2.1 Introduction

As reviewed in chapter IV of Ref. (*17*), LM has been the subject of numerous experimental and theoretical studies for various molecular systems and types of spectra. However, only very few studies have considered the case of collisional exchanges among hyperfine components and/or Stark resolved molecular lines, i.e. when an applied electric field removes the spatial degeneracy of the rotational levels. As first shown by Bréchignac (*12*) for CH_3F in the IR region, the "zero field widths" are significantly smaller than the widths of the various Stark resolved lines. Later on, accurate measurements were performed on pure rotational transitions of CH_3F (*13-15*), confirming the expected *M*-dependence of the widths of the *M*-components as well as the importance of LM effects.

Various theoretical treatments have been proposed to describe collisional couplings between *M*-components. Let us first mention the pioneering work of Buffa, Tarrini and co-workers (*13*), based on a generalization of the well known Anderson-Tsao-Curnutte (ATC) model (*16*). This approach has enabled a clear understanding of the collisional processes between hyperfine and Stark components of molecular spectral lines, for molecules with large dipole moments (*13-15, 18*). An alternative approach to take LM into account is to build the associated relaxation matrix using the Infinite Order Sudden (IOS) approximation (*17, 107*) or its improved Energy Corrected Sudden (ECS) extension (*17, 19, 20*). IOS/ECS models have enabled precise modeling of LM effects for many systems and types of spectra (*17*), including hyperfine components due to the nuclear spin (*21, 22*) and symmetric-top spectra (*23, 24*). However, quite surprisingly, as shown in (*14*), the IOS model developed in (*12*) apparently failed to reproduce the details of coupling processes between the Stark components of CH_3F lines. With the aim of clarifying this result we have re-examined the problem and the presented results suggest that this failure was only due to an oversimplification of the IOS formalism. Indeed, when applied properly, and using basic cross-sections previously (and independently) determined from double resonance experiments and He-broadening data, the IOS formalism leads to an agreement with experimental data comparable to that obtained in (*14*) and (*15*) within a different (ATC-like) approach.

V.2.2 The IOS relaxation matrix

The basic equations used here have been given in (*12*). In the IOS limit, the relaxation matrix elements are expressed in terms of spectroscopic factors (containing the coupling of the various angular momenta of the system) and dynamical factors $Q(L,M_a,M_b)$. Note that M diagonal values $Q(L,M,M)$ can be identified (*20, 107*) with the state to state rotational cross-sections:

$$Q(L,M,M) \equiv \sigma(J=0, K=0 \to J=L, K=M) \ . \tag{V.12}$$

Starting from Ref. (*12*), we first assume that:

$$Q(L,M_a,M_b) = Q(L)\delta_{M_a,0}\delta_{M_b,0} , \tag{V.13}$$

where:

$$Q(L) \equiv \sigma(J=0,K=0 \rightarrow J=L,K=0)$$

$$= \sigma(J=L,K=0 \rightarrow J=0,K=0)(2L+1)\exp\left(-\frac{E(J=L,K=0)}{k_B T}\right) \qquad (V.14)$$

$$\equiv Q'(L)(2L+1)\exp\left(-\frac{E(J=L,K=0)}{k_B T}\right).$$

$Q(L)$ and $Q'(L)$, as the corresponding cross sections σ, are thus related by the detailed balance relation. Equation (V.13) generalizes the approach of (*12*) where it was assumed that a predominant dipole-dipole interaction implies that only $Q'(1)$ is non zero. Even if the dipole-dipole interaction (with its $\Delta J=\pm 1; \Delta K=0$ selection rule) is the dominant contribution to intermolecular forces that connect rotational states through collisions, it can induce $|\Delta J|>1$ rotational changes through higher order terms in the expansion of the S matrix. The $\Delta J=\pm 1$ processes are likely the fastest but they are not the only ones authorized by this interaction. In our opinion, this is the origin of the relative failure; observed in (*14*), of the IOS model of Bréchignac (*12*), in reproducing the experimental data, as will be shown later on.

For CH_3F-He, the validity of Eq; (V.13) approximation has been assumed and discussed in (*108*) where the basic $Q'(L)$ cross-sections, that will be used here, were deduced from an IOS analysis of He-broadening data .

Inserting Eq. (V.13) into the IOS formalism of (*12*), one obtains the following expression for the elements of the relaxation matrix:

$$W(J,K,M;J+1,K,M+\Delta M \rightarrow J,K,M';J+1,K,M'+\Delta M) = (-1)^{M+M'}\sum_k (2k+1)$$

$$\times \begin{pmatrix} J+1 & J & k \\ M'+\Delta M & -M' & -\Delta M \end{pmatrix}\begin{pmatrix} J+1 & J & k \\ M-\Delta M & -M & -\Delta M \end{pmatrix} W^{(k)}(J,K,;J+1,K \rightarrow J,K;J+1,K)$$

$$(V.15)$$

with:

$$W^{(k)}(J,K;J+1,K \rightarrow J,K;J+1,K) = -\sum_L F_k(J,K,J+1,K;J,K,J+1,K;L)Q(L) \qquad (V.16)$$

where:

$$F_k(J,K,J+1,K;J,K,J+1,K;L) = (-1)^{k+L}(2J+1)(2J+3)\begin{pmatrix} J & L & J \\ K & 0 & -K \end{pmatrix}^2 \begin{Bmatrix} J & J+1 & k \\ J+1 & J & L \end{Bmatrix}$$

<div align="right">(V.17)</div>

where $(:::)$ and $\{:::\}$ are 3-j and 6-j coefficients, respectively. Note that:

$$W(J,K,M;J+1,K,M+\Delta M \to J,K,M;J+1,K,M+\Delta M) = \Gamma_{JKM}^{\Delta M},$$

<div align="right">(V.18)</div>

and that the symmetry relations verified by the elements of W given in (*14, 15, 18*) can be easily obtained within the IOS formalism. They will not be detailed here but one has, for instance:

$$\Gamma_{JKM}^{\Delta M=0} = \Gamma_{JK-M}^{\Delta M=0} \ .$$

<div align="right">(V.19)</div>

Using the following expression of the dipole reduced matrix element (*12*):

$$d_{JKM\Delta M} = (-1)^{J+1+M+\Delta M}\sqrt{\frac{3}{2J+1}}\begin{pmatrix} J & J+1 & 1 \\ M & -M-\Delta M & \Delta M \end{pmatrix},$$

<div align="right">(V.20)</div>

and neglecting the influence of the Stark field on the rotational distribution, it can be easily verified that $\bar{S} = \sum_\ell \rho_\ell d_\ell^2 = 1$, provided that the relative populations are defined by $\rho_\ell = 2J+1$. This last equality, which is consistent with the IOS approximation which neglects the spacing between rotational levels, is a good approximation for the low J lines considered in this paper. Then, one can show that, within the IOS limit:

$$\bar{\Gamma}_{JK} = \sum_{\ell,\ell'} \rho_\ell d_\ell d_{\ell'} \operatorname{Re}\{W_{\ell'\ell}\} \equiv W^{(1)}(J,K;J+1,K \to J,K;J+1,K) \ .$$

<div align="right">(V.21)</div>

This result is of course expected since $W^{(1)}(J,K;J+1,K \to J,K;J+1,K)$ is nothing but the IOS width of an "ordinary' rotational line $J,K \to J+1,K$ of a symmetric top molecule (*107*), in the absence of any static field.

Coming back to the collisional line-mixing process, and according to Eqs. (V.6-7), one can see that if the off diagonal elements coupling the various Stark components $M \to M+\Delta M$ are significant, $\bar{\Gamma}_{JK}$ will be significantly smaller than the weighted average Γ_{JK}^{WA} of the widths $\Gamma_{JKM}^{\Delta M}$ of these components. Stark manifolds of various M transitions thus behave similarly to

clusters of other types (*J* or *K* manifolds, *Q* branches, hyperfine components) of closely spaced lines where LM reduces the broadening with increasing pressure (*17*).

V.2.3 Data

The experimental details on the recording of the Stark microwave spectra used for the analysis of line-mixing effects were given in chapter III. Let us only recall here that Stark spectra of $^{12}CH_3F$ (either pure or in mixtures with helium) were recorded for the transitions *J*: $1 \rightarrow 2$ (102 GHz) and *J*: $3 \rightarrow 4$ (204 GHz). Orientations of the electric field parallel and orthogonal to the electric vector of the polarized microwave probing beam were applied thus leading to Stark resolved transitions with the selection rules $\Delta M = 0$ and $\Delta M = \pm 1$, respectively. Electric field intensities from 15 to 35 V/cm were used. Total pressures between 7 and 10 μbar were used for the measurements with pure methyl fluoride while values in the range 100-500 μbar were retained for mixtures with helium typically between 5 and 20 % of CH_3F.

As an example, Fig V.2 displays recorded absorbances near the $J = 1 \rightarrow 2$, $K = 1$ and $K = 0$ transitions of pure methyl fluoride diluted in helium, measured without and with Stark effect induced by a parallel external electric field of about 23.5 V/cm. Under pressure/electric field conditions for which the transitions in the recorded spectra are sufficiently isolated from each other, fits were made to extract collisional parameters. This was done through a multispectrum fitting (*109*) with Voigt profiles yielding the pressure-broadening coefficients $\gamma(CH_3F$-He) of the various lines.
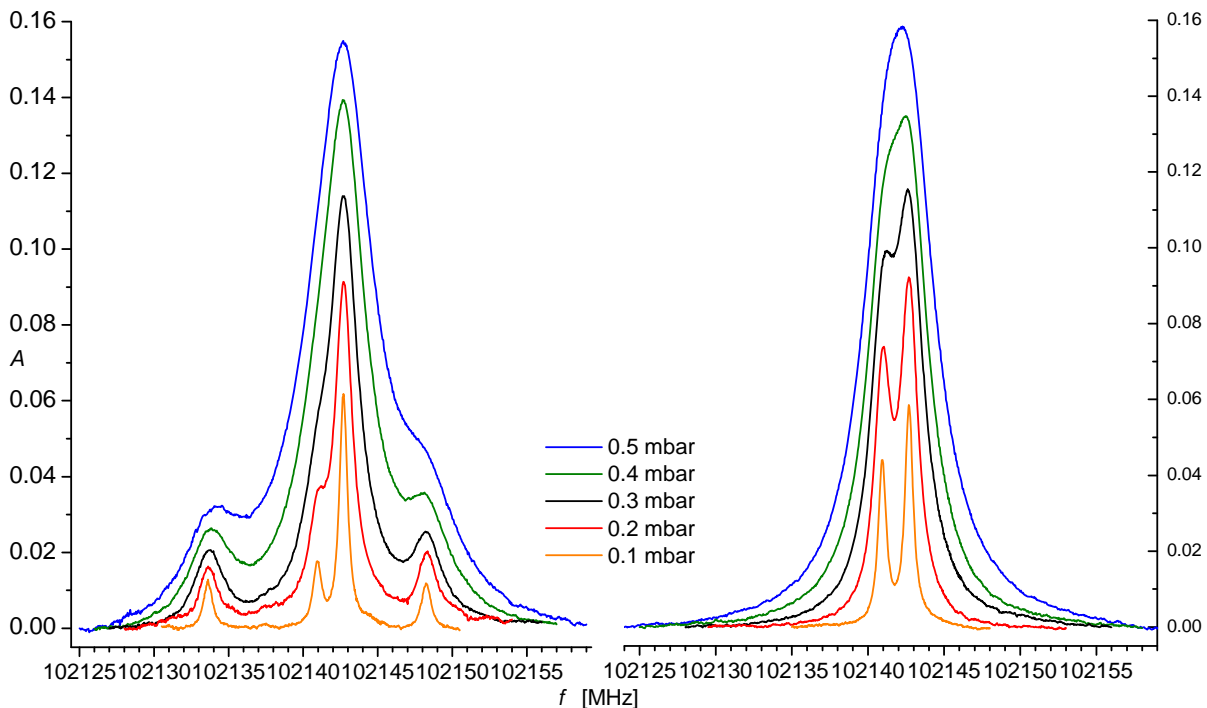
Fig. V.2 Experimental spectra of pure rotational CH$_3$F J: 1→2, K = 0-1 transitions (on right) and the parallel Stark components M = −1, 0 ,1 at E = 23.5 V/cm (on left). Total pressure 0.1-0.5 mbar, mixture CH$_3$F (x = 0.05-0.2) and He (x = 0.80-0.95).

Other typical examples, for $J = 3 \rightarrow 4$ transitions of methyl fluoride diluted in helium, are displayed in Figs. V.3-4.

Fig. V.3 Experimental (red line), Voigt fit (black line) and residuals (blue line) of CH$_3$F J: 3→4, K = 0-3, M = −3, … , 3 parallel Stark lines at E = 27 V/cm. Total pressure 0.1 mbar, mixture CH$_3$F (x = 0.05) and He (x = 0.95).

102

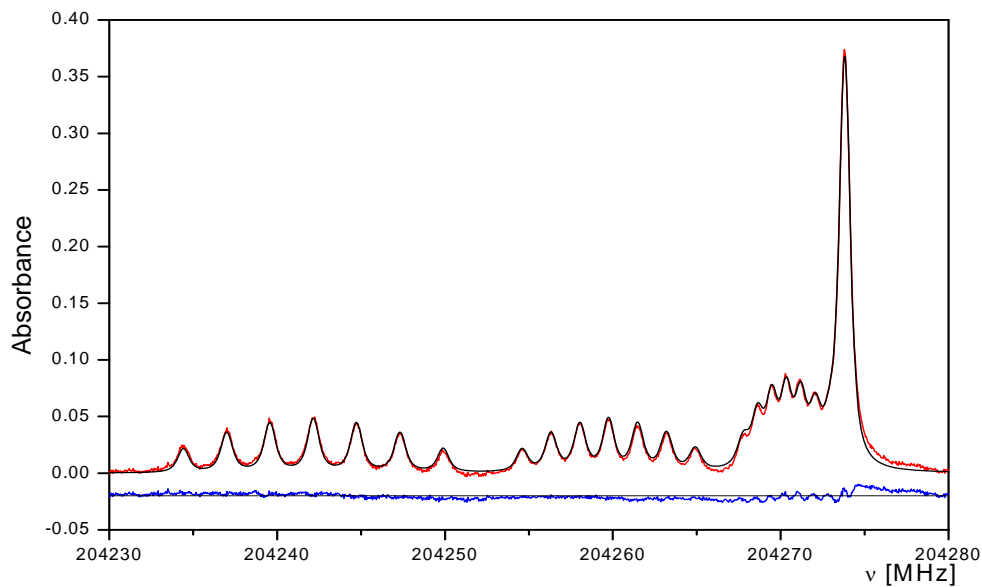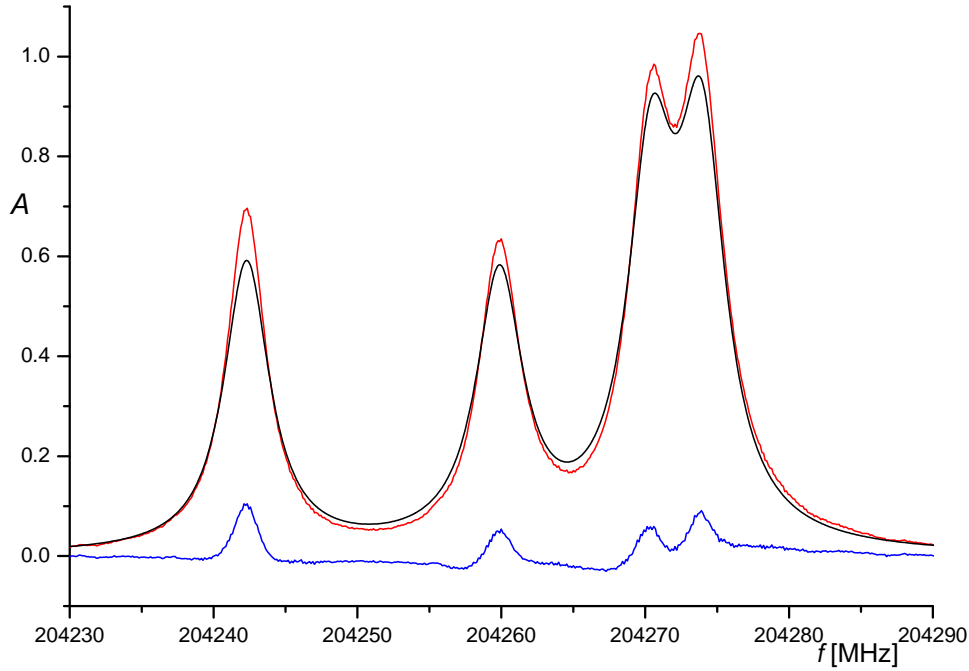**Fig. V.4 Experimental (red line), calculation based on sum of individual *M* components Voigt profiles (black line) and residuals (blue line) of CH$_3$F *J*: 3→4, *K* = 0-3 (from right to left) pure rotational lines (i.e. *E* = 0 V/cm, no Stark effect). Total pressure 0.5 mbar, mixture CH$_3$F (*x* = 13 %) and He (*x* = 0.87 %).**

Note that Fig. V.4 gives a first demonstration of LM effects. Indeed, the profile simulated neglecting LM and thus calculated from the sum of the Lorentzian contributions of the various individual *M* components with broadening values retrieved as in Fig. V.3 is obviously too broad. This is expected from the previously mentioned fact that Γ_{JK}^{WA} is greater than $\overline{\Gamma}_{JK}$. Finally, in order to estimate the uncertainty, the spectra have also been fitted one by one each giving a value of the broadening coefficient. From the scatter of the results for a given transition and various total pressures, the error on our determinations was estimated to be of less than 5 % for pure CH$_3$F and about twice for CH$_3$F-He (due to the fact that the broadening coefficients by He are about one order of magnitude smaller than those for pure CH$_3$F).

V.2.4 Analysis

According to Eqs. (V.14-17), the information required for the calculation of the relaxation matrix are the dynamical factors *Q*(*L*) [or *Q*'(*L*)].

Pure CH$_3$F: Over the past decades, rotational energy transfer in pure CH$_3$F samples have been widely investigated, in particular, by a time resolved millimetre/sub-millimeter-infrared double resonance experiment (*110*). Rotational state-to-state rates were measured

and it was shown that they can be modeled using the IOS theory and the following law for the basic cross-sections:

$$Q'(L \neq 0) \equiv \sigma(L, 0 \rightarrow 0, 0) = A \times [L(L+1)]^{-\alpha} ,$$ (V.22)

[with $Q(L = 0) = -\sum_{L \neq 0} Q(L)$]. The parameters A and α deduced from the measurements of (110) are given in Table V.I. They have been used in the present work to construct the relaxation matrix, after a slight optimization (well within the experimental uncertainty) of the parameters, based on the experimental results (14) for the $J = 5, K = 5 \rightarrow J = 6, K = 5; \Delta M = 0$ line broadening coefficients.

CH_3F-He: Line mixing among usual (i.e. zero field limit) rotational components have been studied in the ν_3 band of CH_3F perturbed by He in (108). The observed modifications with respect to the addition of Lorentzian contributions were analyzed in terms of models respectively based on the IOS and ECS approximations. Both lead to a satisfactory agreement with measurements even if the latter gives better results, particularly for high J values. The basic CH_3F-He cross sections were modeled (108) through the simple analytical law given by Eq. (V.22). The two parameters deduced in this previous study are given in Table V.1 and will be used in the present calculations.

	From previous Ref. experiments	Used in the present work
CH_3F-CH_3F	$A = 8.94 \pm 2.11$ (110) $\alpha = 1.30 \pm 0.05$	$A = 8.63$ $\alpha = 1.325$
CH_3F-He	$A = 0.31$ (108) $\alpha = 0.8$	$A = 0.31$ $\alpha = 0.8$

Table V.1 Parameters of the law of Eq. (V.22) for the basic cross sections (A is given in MHz/Torr).

Finally, let us recall that for CH_3F-He mixtures, the **W** matrix is written according to the binary collision approximation as:

$$\mathbf{W} = P[x_{CH_3F} \mathbf{W}_{CH_3F\text{-}CH_3F} + x_{He} \mathbf{W}_{CH_3F\text{-}He}] ,$$ (V.23)

where P is the total pressure while x_{CH3F} and x_{He} are the mole fractions of CH_3F and He, respectively.

V.2.4.1 Results - Pure CH₃F

Experimental values of the broadening coefficients of transitions with and without a Stark effect from the present study and from (*14*) are compared with the IOS predictions in Fig. V.5 and in Tables V.2-3.
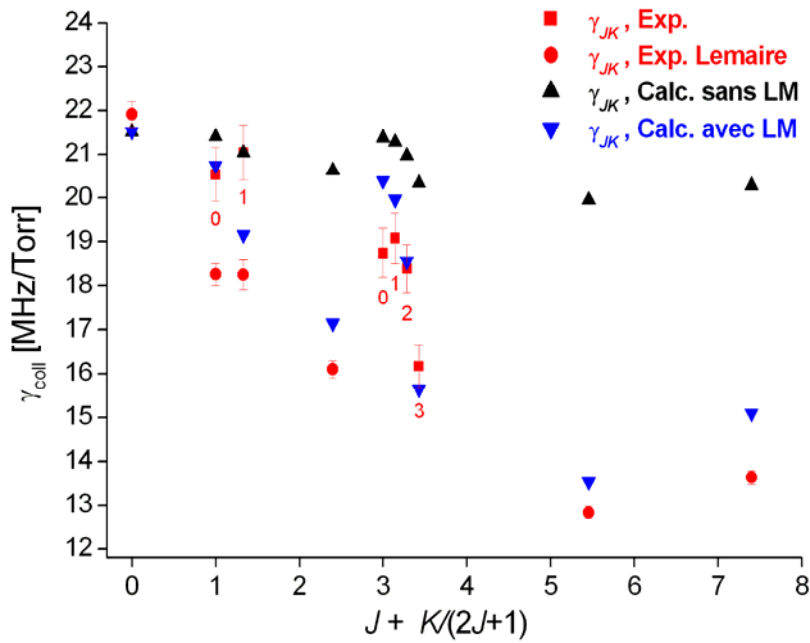

Fig. V.5 **Measured and calculated (IOS) self-broadening coefficients (in MHz/Torr) of CH₃F pure rotational lines**

$J_i,K_i \rightarrow J_f,K_f$	$M_i = M_f$	Experiment		IOS
		Present	Ref. (*14*)	
0,0→1,0	Zero field		21.9	21.5
1,0→2,0	Zero field	20.5	18.3	20.7
1,1→2,1	Zero field	21.0	18.3	19.2
2,2→3,2	Zero field		16.1	17.1
	0		23.2	21.5
	1		22.9	21.0
	2		19.7	19.2
3,0→4,0	Zero field	18.8		20.4
3,1→4,1	Zero field	19.1		19.9
	0	19.8		21.3
	1	20.7		21.3
	2	21.5		21.3
	3	21.8		21.1
3,2→4,2	Zero field	18.4		18.6
	0	25.7		21.5
	1	26.0		21.3
	2	25.1		20.7
	3	24.0		20.0
3,3→4,3	Zero field	16.2		15.6
	0	29.1		21.4
	1	28.6		21.1
	2	28.2		20.1
	3	25.2		18.0
5,5→6,5	Zero field		12.8	13.5
	0		22.4	21.3
	1		23.1	21.1
	2		22.1	20.6
	3		20.9	19.7
	4		19.7	18.3
	5		17.3	16.1
7,6→8,6	Zero field		13.6	15.1
	0		25.3	21.4
	1		25.4	21.3
	2		25.0	21.1
	3		24.3	20.7
	4		23.3	20.0
	5		21.8	19.2
	6		20.0	18.1
	7		17.6	16.9

Table V.2 Measured and calculated (IOS) self-broadening coefficients (in MHz/Torr) in the zero field limit and for isolated Stark components ($\Delta M = 0$ case).

$J_i,K_i \to J_f,K_f$	$M_i \to M_f$	Experiment		IOS
		Present	Ref. (*14*)	
$1,1 \to 2,1$	Zero field		18.2	19.2
	$-1 \to 0$		22.2	21.5
	$1 \to 0$		22.3	21.5
	$0 \to 1$ and $-1 \to -2$		19.4	20.5
	$0 \to -1$ and $1 \to 2$		19.9	19.9
$3,1 \to 4,1$	Zero field	19.1		19.9
	$-3 \to -4$ and $0 \to 1$	19.8		20.8
	$-2 \to -3$ and $1 \to 2$	18.7		21.2
	$-1 \to -2$ and $2 \to 3$	18.7		21.2
	$0 \to -1$ and $3 \to 4$	19.8		20.8
$3,2 \to 4,2$	Zero field	18.4		18.6
	$-3 \to -4$ and $0 \to 1$	22.4		19.9
	$-2 \to -3$ and $1 \to 2$	23.1		20.7
	$-1 \to -2$ and $2 \to 3$	23.1		20.7
	$0 \to -1$ and $3 \to 4$	22.4		19.9
$3,3 \to 4,3$	Zero field	16.2		15.6
	$-3 \to -4$ and $0 \to 1$	23.4		18.0
	$-2 \to -3$ and $1 \to 2$	26.3		19.9
	$-1 \to -2$ and $2 \to 3$	26.3		19.9
	$0 \to -1$ and $3 \to 4$	23.4		18.0
$5,5 \to 6,5$	Zero field		12.8	13.5
	$-5 \to -6$ and $0 \to 1$		16.6	16.4
	$-4 \to -5$ and $1 \to 2$		21.0	18.7
	$-3 \to -4$ and $2 \to 3$		22.8	19.7
	$-2 \to -3$ and $3 \to 4$		22.8	19.7

Table V.3 Measured and calculated (IOS) self-broadening coefficients (in MHz/Torr) in the zero field limit and for isolated Stark components ($\Delta M = \pm 1$ case). When two lines $\Delta M = +1$ and $\Delta M = -1$ are superimposed and since they are not coupled, the calculated value is the weighted average of their individual widths.

For the $J = 5 \to 6$, $K = 5$, and $|M|$ values from 0 to 5, the IOS matrix is given in Table V.4 and results are displayed in Fig. V.6 which also shows previous predictions (*14*). They show that, when properly applied, the IOS model does indeed lead to an agreement with the experimental data very similar to that obtained in (*14*) with the semi-classical approach based on an extension of the ATC model. It quite correctly predicts the *J*, *K* and *M* dependences of the widths and of the amplitude of the coupling process. Recall that the latter manifests through the difference between the width $\overline{\Gamma}_{JK}$ [Eq. (V.21)] of the line for zero field and the average Γ_{JK}^{WA} of those ($\Gamma_{JKM}^{\varepsilon}$) of the individual components [Eq. (V.7)]. For the $7, 6 \to 8, 6$ transitions, for instance, LM leads to a reduction of the broadening by almost a factor of two which is well predicted by our model. From the reasonable agreement between the experimental data and IOS predictions obtained for both the unresolved (zero field) and resolved Stark lines, one can deduce that the IOS evaluation of the relaxation matrix, starting from Eqs. (V.13) and (V.22), is now more reliable than assuming that only $Q'(1)$ is non zero. Consider, as in (*14*), the $J = 5, K = 5 \to J = 6, K = 5$; line and more particularly the ratio of the

width of the zero field line to the $J = 5$, $K = 5$, $M = 0 \rightarrow J = 6$, $K = 5$, $M = 0$ component. The experimental result is 0.572, the semi-classical result of (*14*) is 0.527, while the present IOS prediction is 0.63 and not 0.306 as obtained by assuming that only $Q'(1)$ is non zero. This quality of the IOS approach, when properly applied, is confirmed by the similarity of the IOS relaxation matrix for the case $J = 5$, $K = 5 \rightarrow J = 6$, $K = 5$; $\Delta M = 0$ with that obtained within the semi-classical approach (compare Table V.4 with Table III of (*15*)). Consequently the IOS formalism will give, in the intermediate regime where the Stark components are neither well resolved nor completely degenerate, results very similar to those obtained in (*15*).

M'/M	-5	-4	-3	-2	-1	0	1	2	3	4	5
-5	**+16.0**	-1.94	-0.08	0.06	0.04	0.02	0.01	0.00	0.00	0.00	0.00
-4	-1.94	**+18.3**	-2.76	-0.23	0.05	0.05	0.03	0.01	0.00	0.00	0.00
-3	-0.08	-2.76	**+19.7**	-3.22	-0.34	0.03	0.05	0.03	0.01	0.00	0.00
-2	0.06	-0.23	-3.22	**+20.6**	-3.49	-0.40	0.02	0.05	0.03	0.01	0.00
-1	0.04	0.05	-0.34	-3.49	**+21.1**	-3.61	-0.42	0.02	0.05	0.03	0.01
0	0.02	0.05	0.03	-0.40	-3.61	**+21.2**	-3.61	-0.40	0.03	0.05	0.02
1	0.01	0.03	0.05	0.02	-0.42	-3.61	**+21.1**	-3.49	-0.34	0.05	0.04
2	0.00	0.01	0.03	0.05	0.02	-0.40	-3.49	**+20.6**	-3.22	-0.23	0.06
3	0.00	0.00	0.01	0.03	0.05	0.03	-0.34	-3.22	**+19.7**	-2.76	-0.08
4	0.00	0.00	0.00	0.01	0.03	0.05	0.05	-0.23	-2.76	**+18.3**	-1.94
5	0.00	0.00	0.00	0.00	0.01	0.02	0.04	0.06	-0.08	-1.94	**+16.0**

Table V.4 IOS relaxation matrix elements $W(J,K,M; J+1,K,M \rightarrow J,K,M'; J+1,K,M')$ **(in MHz/Torr) coupling *M* components of the $J = 5$, $K = 5 \rightarrow J = 6$, $K = 5$, $\Delta M = 0$ transitions in pure CH$_3$F.**
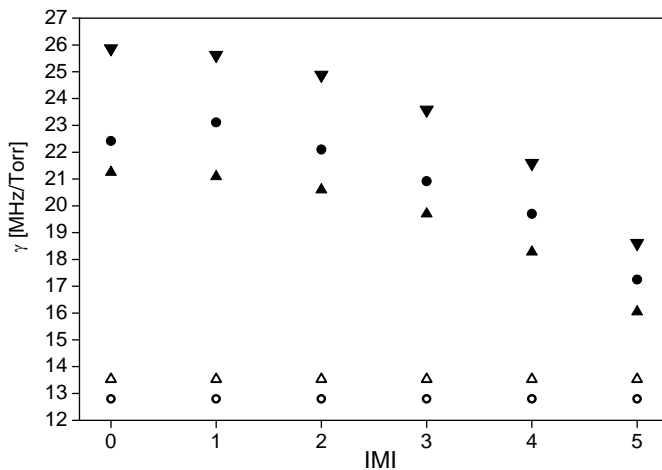

Fig. V.6 CH$_3$F self-broadening coefficients $\gamma_{JKM}^{\Delta M} = \gamma_{JK\text{-}M}^{\Delta M}$ **vs |*M*| for *J*: $5 \rightarrow 6$, $K = 5$, $M = -5$ to 5, $\Delta M = 0$:** ● **Experimental values from Ref. (*14*),** ▼ **calculated values using a semi-classical approach (*14*),** ▲ **values calculated in this study with the IOS model. For comparison, the measured (○) and calculated (Δ, IOS) collisional-broadening coefficients ($\overline{\gamma}_{JK}$) in the zero field limit for the *J*: $5 \rightarrow 6$, $K = 5$ line are also shown.**

V.2.4.2 Results - CH$_3$F diluted in Helium

We shall note that presently measured values (typically 2.6 MHz/Torr) for He- broadening coefficients of CH$_3$F pure rotational lines (the zero field limit of Stark effect) are in good agreement with previous determinations (*111, 112*). The quality of used IOS model is shown by Fig. V.7 which compares our IOS predictions and Grigoriev (*111*) experimental values for some Q branch lines of the ν_3 fundemental band.

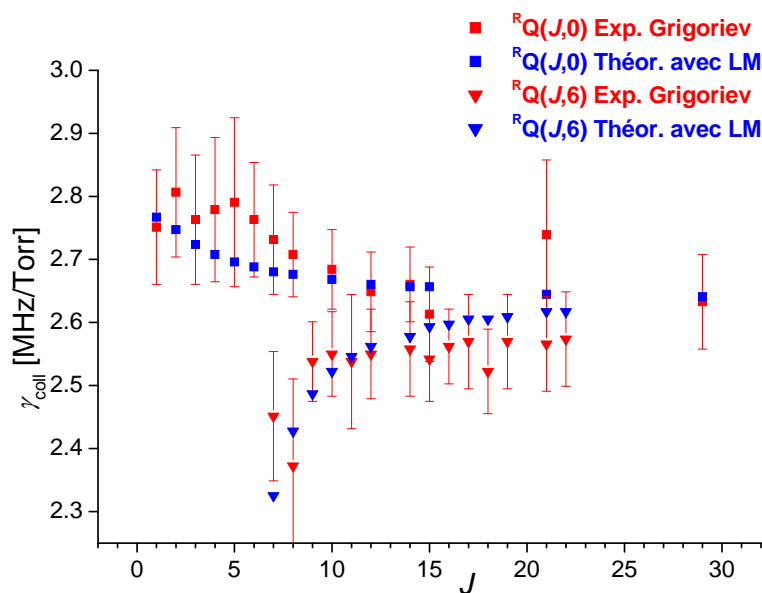**Fig. V.7 IOS and experimental values of He- broadening coefficients of CH$_3$F ν_3 band rovibrational lines**

The results obtained for pure rotational lines of CH$_3$F diluted in He are given in Figs. V.8-9 and are included in Tables V.5-6.
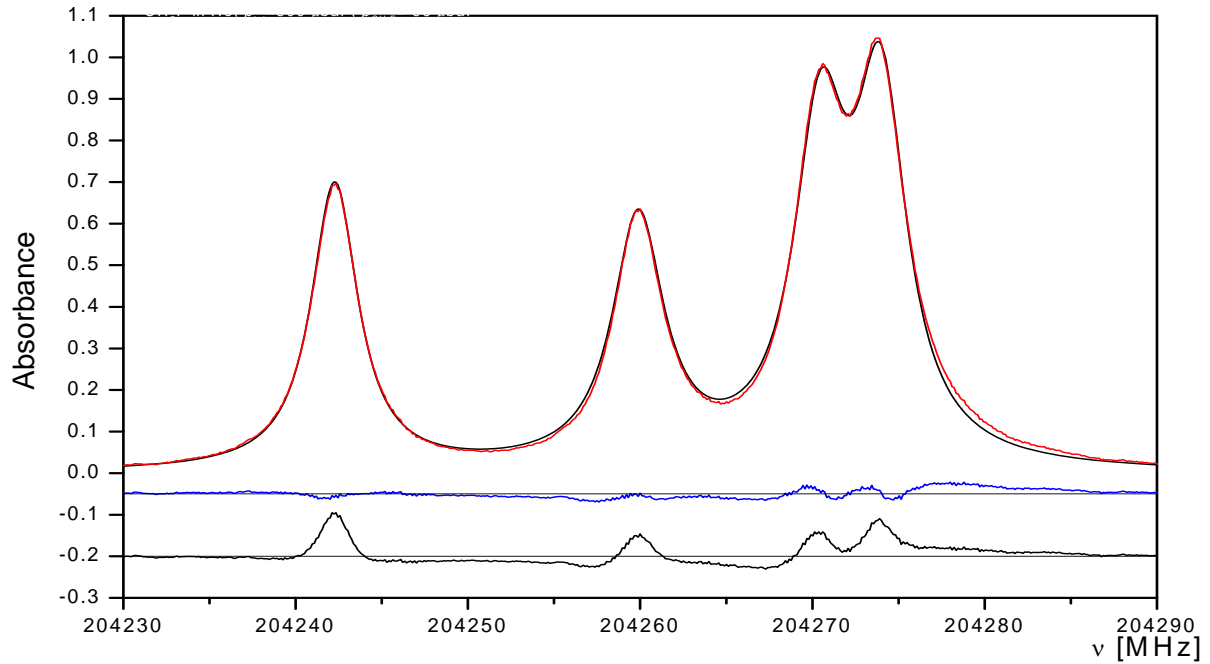
Fig. V.8 Experimental (red) and fitted (black) spectrum and shifted residuals (blue lower trace) for the transitions *J*: 3→4, *K* = 0 to 3 (from right to left) without Stark effect. Total pressure 0.5 mbar, $x(CH_3F) = 13$ %, $x(He) = 87$ %. The black lower trace gives the shifted difference between measured values and those calculated by summing Voigt profiles of all *M* components.
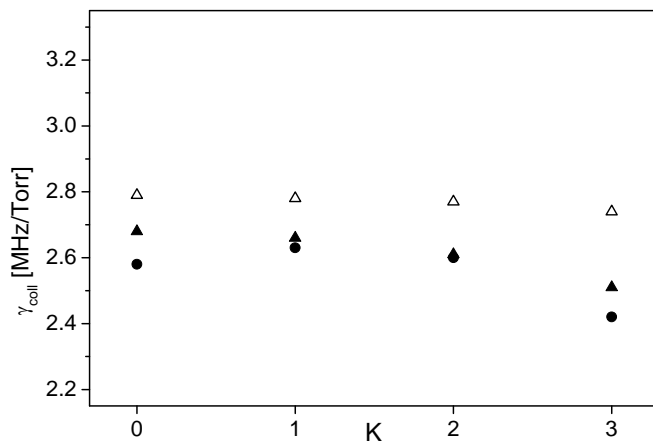
Fig. V.9 CH_3F-He broadening coefficients in the zero field limit $\overline{\gamma}_{JK}$ vs. *K* for *J*: 3→4, *K* = 0-3: ● measured values, ▲ IOS calculated results; the △ symbols correspond to the IOS predictions of the weighted average of the widths of the Stark components γ_{JK}^{WA} .

Furthermore, in spite of a larger uncertainty due to the difficulty to extract the He broadening parameters, it may be reasonably concluded that the observed "zero field- widths" are smaller than the widths of the individual Stark components and consequently of their weighted average (see Fig. V.10 and Tables V.5-6). Here again, the IOS model succeeds at reproducing the amplitude of the coupling process. However, more accurate experiments are clearly

needed to quantify the *M-* dependences of the widths, allowing then a deeper analysis of the *J*, *K* and *M* dependences of the relaxation matrix.

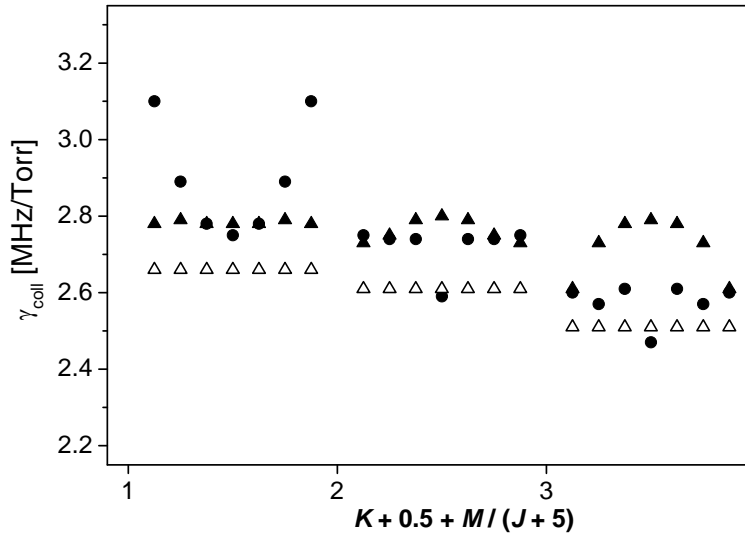**Fig. V.10** CH$_3$F-He broadening coefficients $\gamma_{JKM}^{\Delta M} = \gamma_{JK-M}^{\Delta M}$ as a function of *J*, *K*, *M* for *J*: 3 → 4, *K* = 1 to 3, *M* = −3 to 3, Δ*M* = 0: ● measured values, ▲ IOS calculated results. For comparison, the collisional-broadening coefficients ($\overline{\gamma}_{JK}$ calculated from the IOS model) in the zero field limit for *J*: 3 → 4, *K*= 1 to 3 are also given (△). The three sets of seven results correspond, from left to right to *K* = 1-3 while, in each *K* set, the seven results from left to right are for *M* = −3 to 3.

$J_i,K_i \rightarrow J_f,K_f$	$M_i = M_f$	Meas.	IOS
1,1→2,1	Zero field	2.8	2.7
	0	2.4	2.8
	1	3.0	2.8
3,1→4,1	Zero field	2.6	2.7
	0	2.7	2.8
	1	2.8	2.8
	2	2.9	2.8
	3	3.1	2.8
3,2→4,2	Zero field	2.6	2.6
	0	2.6	2.8
	1	2.7	2.8
	2	2.7	2.7
	3	2.7	2.7
3,3→4,3	Zero field	2.4	2.5
	0	2.5	2.8
	1	2.6	2.8
	2	2.6	2.7
	3	2.6	2.6

Table V.5 Measured and calculated (IOS) He-broadening coefficients (in MHz/Torr) in the zero field limit and for isolated Stark components (Δ*M* = 0 case).

$J_i,K_i \rightarrow J_f,K_f$	$M_i \rightarrow M_f$	Meas.	IOS
$1,1 \rightarrow 2,1$	Zero field	2.8	2.7
	$-1 \rightarrow 0$	2.3	2.8
	$1 \rightarrow 0$	2.3	2.8
	$0 \rightarrow 1$ and $-1 \rightarrow -2$	2.0	2.75
	$0 \rightarrow -1$ and $1 \rightarrow 2$	2.0	2.75
$3,1 \rightarrow 4,1$	Zero field	2.6	2.7
	$-3 \rightarrow -4$ and $0 \rightarrow 1$	3.0	2.75
	$-2 \rightarrow -3$ and $1 \rightarrow 2$	3.6	2.8
	$-1 \rightarrow -2$ and $2 \rightarrow 3$	3.6	2.8
	$0 \rightarrow -1$ and $3 \rightarrow 4$	3.0	2.75
$3,2 \rightarrow 4,2$	Zero field	2.6	2.6
	$-3 \rightarrow -4$ and $0 \rightarrow 1$	3.2	2.75
	$-2 \rightarrow -3$ and $1 \rightarrow 2$	3.0	2.8
	$-1 \rightarrow -2$ and $2 \rightarrow 3$	3.0	2.8
	$0 \rightarrow -1$ and $3 \rightarrow 4$	3.2	2.75
$3,3 \rightarrow 4,3$	Zero field	2.4	2.5
	$-3 \rightarrow -4$ and $0 \rightarrow 1$	2.8	2.75
	$-2 \rightarrow -3$ and $1 \rightarrow 2$	2.9	2.7
	$-1 \rightarrow -2$ and $2 \rightarrow 3$	2.9	2.7
	$0 \rightarrow -1$ and $3 \rightarrow 4$	2.8	2.75

Table V.6 Measured and calculated (IOS) He-broadening coefficients (in MHz/Torr) in the zero field limit and for isolated Stark components ($\Delta M = \pm 1$ case). When two lines $\Delta M = +1$ and $\Delta M = -1$ are superimposed and since they are not coupled, the calculated value is the weighted average of their individual widths.

V.2.5 Conclusion

The measurements presented in this study complete previous results of (*14, 15*) on the self broadening of CH_3F microwave transitions and provide, for the first time, values for He-broadened Stark components. Furthermore, through a correct use of the IOS approximation, we have shown that this model leads to very satisfactory results for the self- and He-broadening coefficients of absorption lines both in the zero field limit and when Stark components are separated by an external electric field. This is, to the writer's knowledge, the first successful demonstration of the ability of the IOS approximation to model line-mixing effects among Stark transitions.

Figures V.11-12 give a good overall view of the present study. In these plots, the spectra have been directly calculated starting from the IOS relaxation matrix **W**, either using the full **W** or restricting it to its diagonal part. The first calculation thus takes line mixing into account while the second does not (uncoupled lines) and corresponds to the addition of individual Lorentzian/Voigt line contributions. As can be seen in Fig. V.11, in the "high-field/low pressures" regime where the Stark components are well resolved, LM effects are small, as expected (*17*), and both approaches give a good prediction of the various Stark components profiles.
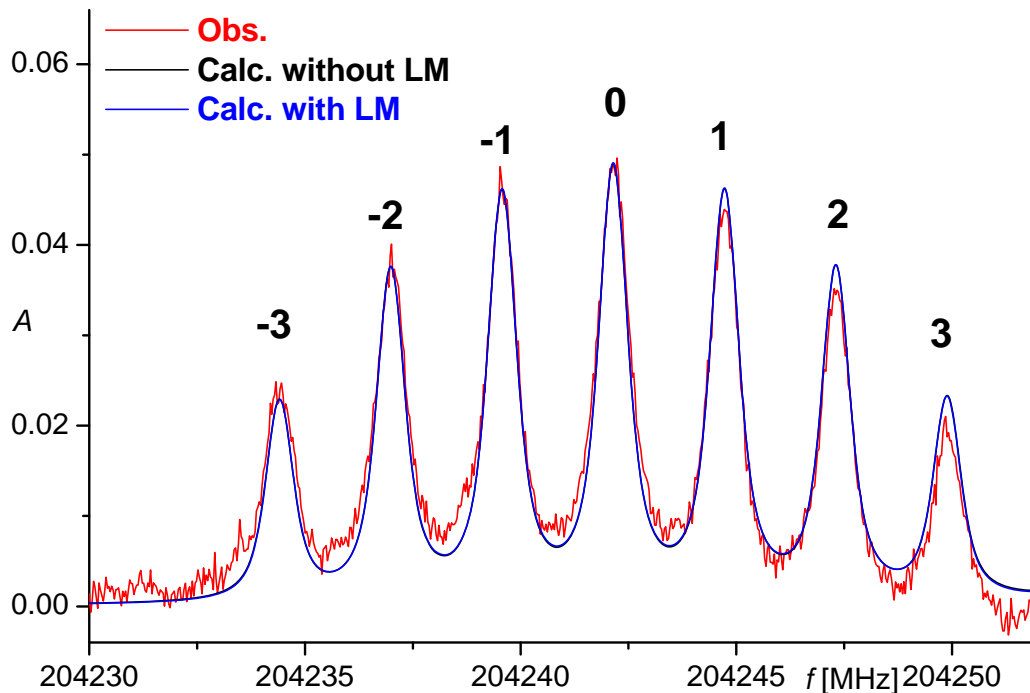
Fig. V.11 CH$_3$F Stark spectrum (Helium broadened): J: $3 \rightarrow 4$, $K = 3$, $\Delta M = 0$, $M = -3,\ldots,3$; $E = 27$ V/cm, $p_{\text{tot}} = 0.1$mbar, $x_{\text{CH}_3\text{F}} = 5$ %

If the static field is removed (and also in the "low-field/high pressures" regime), all these components collapse (Fig. V.12) into a single line whose width is significantly smaller than those of the individual transitions. Assuming a diagonal relaxation matrix then significantly overestimates the observed broadening while using a full matrix leads to very satisfactory results.
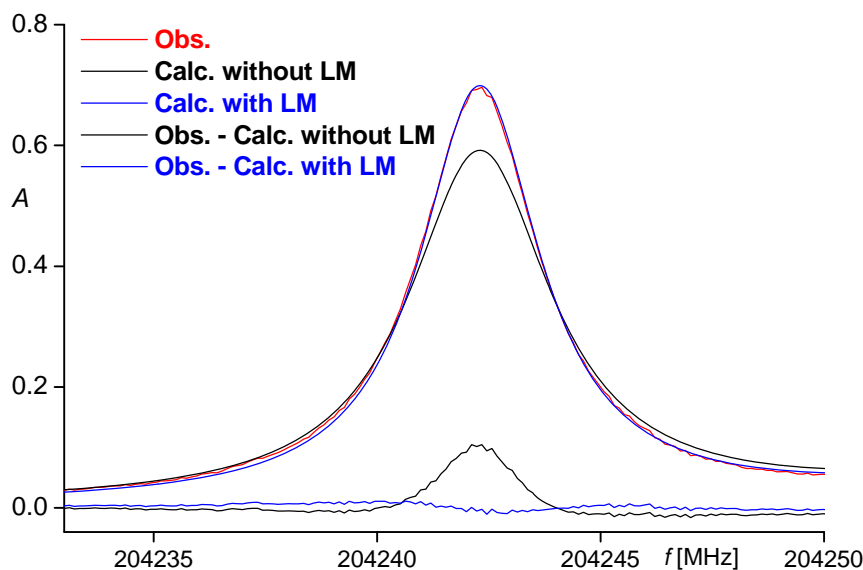
Fig. V.12 CH$_3$F pure rotational spectrum: J: $3 \rightarrow 4$, $K = 3$, $P_{\text{tot}} = 0.5$mbar, $x(\text{CH}_3\text{F}) = 13$ %

Further similar studies of CH_3F-He mixtures for more transitions and higher rotational quantum numbers would be of great interest. These would enable to test the limits of the IOS model and to evaluate the improvements brought by the adiabaticity corrections (*20*) of the Energy Corrected Sudden model. Furthermore, when available, extended experimental data could be compared with the results of direct calculations starting from the intermolecular potential. This could be done within the close-coupling scheme using the sophisticated CH_3F-He potential of Ref. (*113*).

VI Conclusion

Two independent studies in experimental and theoretic gas phase molecular spectroscopy are presented in this thesis: an analysis of the infrared spectra of deuterated nitric acid ($D^{14}NO_3$) and an analysis of collisional effects in the Stark and non Stark microwave spectra of methyl fluoride (CH_3F). These studies were carried out in the frame of co-tutelle thesis program organized by Université Paris-Est (UPE) and by Institute of Chemical Technology, Prague (ICT Prague).

The first part of the thesis presents the first high resolution analysis of the ν_5 fundamental band (NO_2 in plane bending mode) of DNO_3 (deuterated nitric acid) in the 11 μm spectral region. In order to carry out the project, we used an infrared spectrum of $D^{14}NO_3$ recorded with a Fourier transform spectrometer in the $700-1400$ cm^{-1} region by Profs. Helmut Beckers and Helge Willner at Bergische Universität in Wuppertal. The analysis of the ν_5 band of DNO_3 centred at 887.657 cm^{-1} which is mostly an A-type band, was performed at LISA. Our study shows that the fundamental ν_5 band is very perturbed. In the case of DNO_3, there is the $\nu_7 + \nu_9$ "dark" combination band situated at 882.211 cm^{-1}. The 5^1 and 7^19^1 energy levels of DNO_3 are therefore coupled through A and B type Coriolis resonances. The resonance scheme for $D^{14}NO_3$ thus differs a lot from those involve in $H^{14}NO_3$ and $H^{15}NO_3$, since, for these two isotopologues, the 5^1 and 9^2 energy levels are coupled through Fermi and C type Coriolis resonances. Finally, the absolute line intensities for the ν_5 band of DNO_3 were calculated using the ν_5 transition operator from $H^{14}NO_3$. The hot bands $\nu_5+\nu_6-\nu_6$, $\nu_5+\nu_7-\nu_7$ and $\nu_5+\nu_9-\nu_9$ located at 881.03, 882.61 and 884.45 cm^{-1}, respectively, were also identified in the spectrum.

The second part of the thesis is devoted to the analysis of the spectral shape, when influenced by collisions, of pure rotational spectra of CH_3F (CH_3F-CH_3F, CH_3F-He) in the absence or presence of a Stark effect. The microwave spectra were recorded at ICT Prague and analysed at LISA. Various profiles have been used to model the shapes of the lines when spectreally isolated. As expected, the widely used Voigt profile leads, at the lower pressures when the lines are spectrally separated, to errors with a shape characteristic of a narrowing that could be partially removed by using speed dependent Voigt profiles as well as by Rautian profiles. A speed dependent Rautian profile with calculated self-broadening speed dependent coefficients was also used, in an attempt to take both the speed dependence and Dicke narrowing into account. The results seem promising but remain not conclusive likely due to

the insufficient quality of the measured spectra. Self- and He-broadening coefficients of microwave transitions of CH_3F have also been measured with and without the presence of an external electric field. This provides values for the $J, K {\rightarrow} J + 1, K$ ($K = 0, …, J$) transitions for $J = 1$ and $J = 3$ as well as for the various $J, K, M \rightarrow J+1, K, M'$ ($|M| = 0, …, J$; $|M{-}M'| = 0, 1$) Stark components. The measurements presented in this study complete previous results of Lemaire *et al.* (*14, 15*) on the self broadening of CH_3F microwave transitions and provide, for the first time, values for He-broadened Stark components. Furthermore, through a correct use of the Infinite Order Sudden (IOS) approximation, it is shown that this model leads to very satisfactory predictions of line-mixing effects for the self- and He-broadening coefficients of absorption lines both in the zero field limit and when Stark components are separated by an external electric field. This is the first successful demonstration of the ability of the IOS approximation to model line-mixing effects among Stark transitions.

$* * *$

The work presented in this thesis was published in two articles:

J. Koubek, C. Boulet, A. Perrin, Š. Urban and J.-M. Hartmann, Line-mixing between rotational Stark components of CH_3F self-perturbed and perturbed by helium: Experimental results and IOS analysis, Journal of Molecular Spectroscopy, Journal of Molecular Spectroscopy, 266, 2011, 12-20

J. Koubek, A. Perrin, H. Beckers, H. Willner and Š. Urban, First analysis of the ν_5 band of DNO_3 (deuterated nitric acid) in the 11 μm region, Journal of Quantitative Spectroscopy & Radiative Transfer, 111, 2010, 1184-1192

Three more articles co-signed by Jindřich Koubek were published during his thesis studies:

S. Zvánovec, P. Černý, P. Piksa, T. Kořínek, P. Pechač, M. Mazánek, J. Varga, J. Koubek, Š. Urban, The Use of the Fabry-Perot Interferometer for High Resolution Microwave Spectroscopy, Journal of Molecular Spectroscopy, 256, 2009, 141-145

L. Nová Stříteská, M. Šimečková, P. Kania, P. Musil, L. Kolesniková, J. Koubek and Š. Urban, Precise ground state molecular parameters of chloromethane, Journal of Molecular Structure, 919, 2009, 89-93

P. Kania, L. Nová Stříteská, M. Šimečková, P. Musil, L. Kolesniková, J. Koubek and Š. Urban, Rotational spectrum of ^{13}C chloromethanes, Journal of Molecular Spectroscopy, 252 , 2008, 90-92

VII References

1. *Scientific Assessment of Ozone Depletion: 1998*. Global Ozone Research and Monitoring Project (World Meteorological Organization (WMO), Geneva, 1999).
2. *Scientific Assessment of Ozone Depletion: 2006*. Global Ozone Research and Monitoring Project (World Meteorological Organization (WMO), Geneva, 2007).
3. F. Mencaraglia *et al.*, *J. Geophys. Res.* **111**, (2006).
4. A. Perrin, *Spectrochimica Acta Part A: Molecular and Biomolecular Spectroscopy* **54**, 375 (1998).
5. G. Brizzi, M. Carlotti, J. M. Flaud, A. Perrin, M. Ridolfi, *Geophys. Res. Lett.* **34**, (2007).
6. D. T. Petkie, T. M. Goyette, P. Helminger, H. M. Pickett, F. C. De Lucia, *Journal of Molecular Spectroscopy* **208**, 121 (2001).
7. A. Perrin *et al.*, *Journal of Molecular Spectroscopy* **228**, 375 (2004).
8. A. Perrin, R. Mbiaké, *Journal of Molecular Spectroscopy* **237**, 27 (2006).
9. D. T. Petkie *et al.*, *Journal of Molecular Spectroscopy* **251**, 358 (2008).
10. L. Gomez *et al.*, *Journal of Quantitative Spectroscopy and Radiative Transfer* **110**, 675 (2009).
11. C. Gutle, J. Demaison, H. D. Rudolph, *Journal of Molecular Spectroscopy* **254**, 99 (2009).
12. P. Brechignac, *The Journal of Chemical Physics* **76**, 3389 (1982).
13. G. Buffa, A. Di Lieto, P. Minguzzi, O. Tarrini, M. Tonelli, *Physical Review A* **34**, 1065 (1986).
14. V. Lemaire *et al.*, *The Journal of Chemical Physics* **106**, 8995 (1997).
15. V. Lemaire *et al.*, *The Journal of Chemical Physics* **110**, 9418 (1999).
16. C. J. Tsao, B. Curnutte, *Journal of Quantitative Spectroscopy and Radiative Transfer* **2**, 41 (1962/3//, 1962).
17. J.-M. Hartmann, C. Boulet, D. Robert, *Collisional Effects on Molecular Spectra*. (Elsevier, Amsterdam, 2008).
18. S. Belli, G. Buffa, O. Tarrini, *Physical Review A* **55**, 183 (1997).
19. A. E. DePristo, S. D. Augustin, R. Ramaswamy, H. Rabitz, *The Journal of Chemical Physics* **71**, 850 (1979).
20. A. M. Richard, A. E. DePristo, *Chemical Physics* **69**, 273 (1982).
21. S. Green, *The Journal of Chemical Physics* **88**, 7331 (1988).
22. P. M. Flaud, J. Orphal, C. Boulet, J. M. Hartmann, *Journal of Molecular Spectroscopy* **235**, 149 (2006).
23. S. Hadded, F. Thibault, P. M. Flaud, H. Aroui, J. M. Hartmann, *The Journal of Chemical Physics* **116**, 7544 (2002).
24. S. Hadded, F. Thibault, P. M. Flaud, H. Aroui, J. M. Hartmann, *The Journal of Chemical Physics* **120**, 217 (2004).
25. M. Born, R. Oppenheimer, *Annalen der Physik* **389**, 457 (1927).
26. P. J. Mohr, B. N. Taylor, D. B. Newell, *Reviews of Modern Physics* **80**, 633 (2008).
27. C. Eckart, *Physical Review* **47**, 552 (1935).
28. B. T. Darling, D. M. Dennison, *Physical Review* **57**, 128 (1940).
29. J. K. G. Watson, *Molecular Physics: An International Journal at the Interface Between Chemistry and Physics* **15**, 479 (1968).
30. D. T. Petkie, P. Helminger, R. A. H. Butler, S. Albert, F. C. De Lucia, *Journal of Molecular Spectroscopy* **218**, 127 (2003).
31. B. J. Drouin *et al.*, *Journal of Molecular Spectroscopy* **236**, 29 (2006).
32. G. E. McGraw, D. L. Bernitt, I. C. Hisatsune, *The Journal of Chemical Physics* **42**, 237 (1965).
33. T. L. Tan *et al.*, *Journal of Molecular Spectroscopy* **166**, 97 (1994).
34. J. Koubek, A. Perrin, H. Beckers, H. Willner, S. Urban, *Journal of Quantitative Spectroscopy and Radiative Transfer* **111**, 1184 (2010).
35. A. G. Maki *et al.*, *Journal of Molecular Spectroscopy* **157**, 248 (1993).
36. F. Keller *et al.*, *Journal of Molecular Spectroscopy* **191**, 306 (1998).

37.   T. L. Tan *et al.*, *Journal of Molecular Spectroscopy* **149**, 425 (1991).
38.   T. L. Tan *et al.*, *Journal of Molecular Spectroscopy* **150**, 486 (1991).
39.   A. Goldman, C. P. Rinsland, A. Perrin, J. M. Flaud, *Journal of Quantitative Spectroscopy and Radiative Transfer* **60**, 851 (1998).
40.   P. R. Bunker, *Molecular symmetry and spectroscopy*. (Academic Press (New York), 1979), pp. xv, 424 p.
41.   A. Perrin, O. Lado-Bordowsky, A. Valentin, *Molecular Physics* **67**, 249 (10 June 1989, 1989).
42.   A. G. Maki, W. B. Olson, *Journal of Molecular Spectroscopy* **133**, 171 (1989).
43.   H. Partridge, D. W. Schwenke, *The Journal of Chemical Physics* **106**, 4618 (1997).
44.   D. W. Schwenke, *Spectrochimica Acta Part A: Molecular and Biomolecular Spectroscopy* **58**, 849 (2002).
45.   V. G. Tyuterev, S. Tashkun, P. Jensen, A. Barbe, T. Cours, *Journal of Molecular Spectroscopy* **198**, 57 (1999).
46.   S. N. Yurchenko, M. Carvajal, W. Thiel, P. Jensen, *Journal of Molecular Spectroscopy* **239**, 71 (2006).
47.   J. H. Van Vleck, *Physical Review* **33**, 467 (1929).
48.   W. H. Shaffer, H. H. Nielsen, L. H. Thomas, *Physical Review* **56**, 895 (1939).
49.   M. Goldsmith, G. Amat, H. H. Nielsen, *The Journal of Chemical Physics* **24**, 1178 (1956).
50.   G. Amat, H. H. Nielsen, G. Tarrago, *Rotation-vibration of polyatomic molecules: Higher order energies and frequencies of spectral transitions*. (M. Dekker (New York), 1971), pp. vi, 441 p.
51.   D. Papousek, M. R. Aliev, *Molecular Vibrational--Rotational Spectra*. (Elsevier, Amsterdam, 1982).
52.   H. H. Nielsen, *Reviews of Modern Physics* **23**, 90 (1951).
53.   J. K. G. Watson, in *Vibrational Spectra and Structure,* J. R. Durig, Ed. (Elsevier, Amsterdam, 1977), vol. 6.
54.   J. K. G. Watson, *The Journal of Chemical Physics* **46**, 1935 (1967).
55.   J. K. G. Watson, *The Journal of Chemical Physics* **48**, 4517 (1968).
56.   J. K. G. Watson, *The Journal of Chemical Physics* **48**, 181 (1968).
57.   J.-M. Flaud, C. Camy-Peyret, R. A. Toth, *Water Vapour Line Parameters from Microwave to Medium Infrared*. (Pergamon press, Oxford, 1981).
58.   V. I. Perevalov, V. G. Tyuterev, *Journal of Molecular Spectroscopy* **96**, 56 (1982).
59.   C. Camy-Peyret, J.-M. Flaud, in *Flaud, J.-M. Camy-Peyret, C.,* K. Narahari Rao, Ed. (Academic Press, Orlando, 1985), vol. III.
60.   S. G. Chou, D. T. Petkie, R. A. H. Butler, C. E. Miller, *Journal of Molecular Spectroscopy* **211**, 284 (2002).
61.   L. S. Rothman *et al.*, *Journal of Quantitative Spectroscopy and Radiative Transfer* **96**, 139 (2005).
62.   R. A. Toth, *Journal of Molecular Spectroscopy* **190**, 379 (1998).
63.   R. A. Toth, *Appl. Opt.* **30**, 5289 (1991).
64.   R. A. Toth, *Journal of Molecular Spectroscopy* **162**, 41 (1993).
65.   P. Kania, Institute of Chemical Technology Prague (2006).
66.   P. Kania, L. Stříteská, M. Šimečková, Š. Urban, *Journal of Molecular Structure* **795**, 209 (2006).
67.   L. Nová Stříteská *et al.*, *Journal of Molecular Structure* **919**, 89 (2009).
68.   F. X. Brown, D. Dangoisse, J. Gadhi, G. Wlodarczak, J. Demaison, *Journal of Molecular Structure* **190**, 401 (1988).
69.   M. Lepčre, G. Blanquet, J. Walrand, J.-P. Bouanich, *Journal of Molecular Spectroscopy* **180**, 218 (1996).
70.   M. D. Marshall, J. S. Muenter, *Journal of Molecular Spectroscopy* **83**, 279 (1980).
71.   R. G. Shulman, B. P. Dailey, C. H. Townes, *Physical Review* **78**, 145 (1950).
72.   S. A. Marshall, J. Weber, *Physical Review* **105**, 1502 (1957).
73.   J. S. Muenter, *The Journal of Chemical Physics* **48**, 4544 (1968).
74.   H. A. Dijkerman, G. Ruitenberg, *Chemical Physics Letters* **3**, 172 (1969).

75.   F. H. De Leeuw, A. Dymanus, *Chemical Physics Letters* **7**, 288 (1970).
76.   J. M. L. J. Reinartz, W. L. Meertz, A. Dymanus, *Chemical Physics Letters* **16**, 576 (1972).
77.   E. R. Cohen, J. W. M. DuMond, *Reviews of Modern Physics* **37**, 537 (1965).
78.   B. N. Taylor, W. H. Parker, D. N. Langenberg, *Reviews of Modern Physics* **41**, 375 (1969).
79.   J. M. L. J. Reinartz, A. Dymanus, *Chemical Physics Letters* **24**, 346 (1974).
80.   C. P. Smyth, K. B. McAlpine, *The Journal of Chemical Physics* **2**, 499 (1934).
81.   S. N. Ghosh, R. Trambarulo, W. Gordy, *The Journal of Chemical Physics* **21**, 308 (1953).
82.   D. M. Larkin, W. Gordy, *The Journal of Chemical Physics* **38**, 2329 (1963).
83.   P. Alston Steiner, W. Gordy, *Journal of Molecular Spectroscopy* **21**, 291 (1966).
84.   R. G. Brewer, *Physical Review Letters* **25**, 1639 (1970).
85.   S. C. Wofsy, J. S. Muenter, W. Klemperer, *The Journal of Chemical Physics* **55**, 2014 (1971).
86.   S. M. Freund, G. Duxbury, M. Römheld, J. T. Tiedje, T. Oka, *Journal of Molecular Spectroscopy* **52**, 38 (1974).
87.   D. K. Coles, W. E. Good, R. H. Hughes, *Physical Review* **79**, (1950).
88.   S. A. Rackley, R. J. Butcher, M. Römheld, S. M. Freund, T. Oka, *Journal of Molecular Spectroscopy* **92**, 203 (1982).
89.   J. Sakai, M. Katayama, *Journal of Molecular Structure* **190**, 113 (1988).
90.   J. Gadhi, A. Lahrouni, J. Legrand, J. Demaison, *Journal de Chimie Physique* **92**, 1984 (1995).
91.   H. A. Lorentz, *Proc. R. Acad.* **8,**, 591 (1906).
92.   J. H. Van Vleck, V. F. Weisskopf, *Reviews of Modern Physics* **17**, 227 (1945).
93.   J. P. Wittke, R. H. Dicke, *Physical Review* **103**, 620 (1956).
94.   W. Voigt, *Sitzungsber. Bayerische Akad. Wiss.* **42**, (1912).
95.   L. Galatry, *Physical Review* **122**, 1218 (1961).
96.   S. Rautian, J. Sobel'man, *Sov Phys Usp* **9**, (1967).
97.   M. Nelkin, A. Ghatak, *Physical Review* **135**, A4 (1964).
98.   P. R. Berman, *Journal of Quantitative Spectroscopy and Radiative Transfer* **12**, 1331 (1972).
99.   F. Rohart, A. Ellendt, F. Kaghat, H. Mäder, *Journal of Molecular Spectroscopy* **185**, 222 (1997).
100.   D. Robert, J. Bonamy, *Journal de Physique* **40**, 923 (1979).
101.   E. W. Smith, *The Journal of Chemical Physics* **74**, 6658 (1981).
102.   R. G. Gordon, R. P. McGinnis, *The Journal of Chemical Physics* **49**, 2455 (1968).
103.   T. A. Brunner, D. Pritchard, *Fitting Laws for Rotationally Inelastic Collisions*. Advances in Chemical Physics (John Wiley & Sons, Inc., 1982), pp. 589-641.
104.   R. Goldflam, S. Green, D. J. Kouri, *The Journal of Chemical Physics* **67**, 4149 (1977).
105.   W. B. Neilsen, R. G. Gordon, *The Journal of Chemical Physics* **58**, 4131 (1973).
106.   P. W. Anderson, *Physical Review* **76**, 647 (1949).
107.   S. Green, *The Journal of Chemical Physics* **70**, 816 (1979).
108.   F. Thibault, J. Boissoles, I. M. Grigoriev, N. N. Filippov, M. V. Tonkov, *European Physical Journal D* **6**, 343 (1999).
109.   D. C. Benner, C. P. Rinsland, V. M. Devi, M. A. H. Smith, D. Atkins, *Journal of Quantitative Spectroscopy and Radiative Transfer* **53**, 705 (1995).
110.   H. O. Everitt, F. C. DeLucia, *The Journal of Chemical Physics* **92**, 6480 (1990).
111.   I. M. Grigoriev, J.-P. Bouanich, G. Blanquet, J. Walrand, M. Lepčre, *Journal of Molecular Spectroscopy* **186**, 48 (1997).
112.   M. M. Beaky, D. C. Flatin, J. J. Holton, T. M. Goyette, F. C. De Lucia, *Journal of Molecular Structure* **352-353**, 245 (1995).
113.   B. Bussery-Honvault, R. Moszynski, J. Boissoles, *Journal of Molecular Spectroscopy* **232**, 73 (2005).

VIII Appendices

VIII.1 Appendix 1: Derivation of speed dependent Voigt profile formula

The speed dependent Voigt profile is derived for an isolated line centered at frequency ν_{if}, disregarding thus the line-mixing effects. The Doppler effect is taken in account as well as the dependences of collisional broadening and shifting parameters on the speed v of the absorbing molecule. The Dicke narrowing is not considered. The normalized absorption profile is that of equation (IV.36) stated in IV.2.3.:

$$I_{sdVoigt}(\nu) = \frac{1}{\pi} \operatorname{Im}\left\{\iiint f_M(\vec{v})\left[\nu - \nu_{if} - \Delta(v) - \vec{k}.\vec{v} - i\Gamma(v)\right]^{-1} d^3\vec{v}\right\} \qquad (VIII.1.1)$$

Remark, that following equation is equivalent to VIII.1.1 through $\operatorname{Im}\{iZ\} = \operatorname{Re}\{Z\}$:

$$I_{sdVoigt}(\nu) = \frac{1}{\pi} \operatorname{Re}\left\{\iiint f_M(\vec{v})\left[\Gamma(v) - i(\nu - \nu_{if} - \Delta(v) - \vec{k}.\vec{v})\right]^{-1} d^3\vec{v}\right\} \qquad (VIII.1.2)$$

The wave propagation vector can be expressed, assuming that it is along the z axis, as:

$\vec{k} = \vec{z}\,\nu_{if}/c$. The normalised Maxwell-Boltzmann distribution of the radiator velocity expression using Euler angles is:

$$f_{MB}(\vec{v})\, d^3\vec{v} = \left(\tilde{v}\sqrt{\pi}\right)^{-3} d\phi \sin(\theta)\, d\theta\, v^2 \exp\left[-(v/\tilde{v})^2\right], \qquad (VIII.1.3)$$

with $\phi \in [0, 2\pi]$, $\theta \in [0, \pi]$, $v \in [0, +\infty]$, $\tilde{v} = \sqrt{\dfrac{2\,k_B\,T}{M}}$, $\qquad (VIII.1.4)$

and, with this coordinate system, one has where $\vec{k}.\vec{v} = \dfrac{\nu_{if}}{c}\,v\cos(\theta)$.

Equation (VIII.1.1) after adaptation of relations (VIII.1.3-4) leads to

$$I_{sdVoigt}(\nu) = \frac{\left(\tilde{v}\sqrt{\pi}\right)^{-3}}{\pi} \int_0^{2\pi} d\phi \int_0^{+\infty} v^2 \exp\left[-(v/\tilde{v})^2\right]\, dv$$

$$\times \int_0^{\pi} \sin(\theta)\, d\theta\, \operatorname{Im}\left\{\frac{1}{\nu - \nu_{if} - \Delta(v) - \dfrac{\nu_{if}}{c}\, v\cos(\theta) - i\Gamma(v)}\right\} \qquad (VIII.1.5)$$

and gives after integration over ϕ and θ :

$$I_{\text{sdVoigt}}(\nu) = \frac{\left(\tilde{v}\,\sqrt{\pi}\right)^{-3}}{\pi}\,2\pi\int_{0}^{+\infty} v^2\,\exp\left[-\left(v/\tilde{v}\right)^2\right]\,dv$$
$$\times\frac{c}{v\,\nu_{\text{if}}}\,\text{Im}\left\{\left[\ln\left(\nu-\nu_{\text{if}}-\Delta(v)-\frac{\nu_{\text{if}}}{c}\,v\,\cos(\theta)-i\Gamma(v)\right)\right]_{0}^{\pi}\right\} \qquad \text{(VIII.1.6)}$$

$$I_{\text{sdVoigt}}(\nu) = \frac{c}{v\,\nu_{\text{if}}}\,\frac{\left(\tilde{v}\,\sqrt{\pi}\right)^{-3}}{\pi}\,2\pi\int_{0}^{+\infty} v^2\,\exp\left[-\left(v/\tilde{v}\right)^2\right]dv$$
$$\times\text{Im}\left\{\ln\left(\nu-\nu_{\text{if}}-\Delta(v)+\frac{\nu_{\text{if}}}{c}\,v\,-i\Gamma(v)\right)-\ln\left(\nu-\nu_{\text{if}}-\Delta(v)-\frac{\nu_{\text{if}}}{c}\,-i\Gamma(v)\right)\right\} \qquad \text{(VIII.1.7)}$$

Remarking the equivalence:

$$-\int_{0}^{+\infty} v^2\,\exp\left[-\left(v/\tilde{v}\right)^2\right]dv\,\ln\left(\nu-\nu_{\text{if}}-\Delta(v)-\frac{\nu_{\text{if}}}{c}\,-i\Gamma(v)\right)=$$
$$\int_{-\infty}^{0} v^2\,\exp\left[-\left(v/\tilde{v}\right)^2\right]dv\,\ln\left(\nu-\nu_{\text{if}}-\Delta(v)+\frac{\nu_{\text{if}}}{c}\,-i\Gamma(v)\right) \qquad \text{(VIII.1.8)}$$

and after simplifications of the equation (VIII.1.7) we obtain:

$$I_{\text{sdVoigt}}(\nu) = 2\left(\tilde{v}\,\sqrt{\pi}\right)^{-3}\frac{c}{\nu_{\text{if}}}\int_{-\infty}^{+\infty} v\,\exp\left[-\left(v/\tilde{v}\right)^2\right]$$
$$\times\text{Im}\left\{\ln\left(\nu-\nu_{\text{if}}-\Delta(v)+\frac{\nu_{\text{if}}}{c}\,v\,-i\Gamma(v)\right)\right\}\,dv \qquad \text{(VIII.1.9)}$$

After integrating per partes of the equation (VIII.1.9) we obtain:

$$I_{\text{sdVoigt}}(\nu) = \left(\tilde{v}\,\sqrt{\pi}\right)^{-3}\frac{c}{\nu_{\text{if}}}\,\tilde{v}^2\int_{-\infty}^{+\infty} e^{-\left(\frac{v}{\tilde{v}}\right)^2}\,\text{Im}\left\{\frac{\frac{\nu_{\text{if}}}{c}\,-\Delta'(v)\,-i\Gamma'(v)}{\nu-\nu_{\text{if}}-\Delta(v)+\frac{\nu_{\text{if}}}{c}\,v\,-i\Gamma(v)}\right\}\,dv \qquad \text{(VIII.1.10)}$$

Performing of a change of variables $v\to\tilde{v}\,t$ and introduction of $\nu_{\text{D}}=\frac{\nu_{\text{if}}}{c}\,\tilde{v}$ leads then to:

$$I_{\text{sdVoigt}}(\nu) = \pi^{-3/2}\,\frac{1}{\nu_{\text{D}}}\int_{-\infty}^{+\infty}\exp\left(-t^2\right)\,\text{Im}\left\{\frac{1-z'(t)}{x+t\,-z(t)}\right\}\,dt \qquad \text{(VIII.1.11)}$$

$$x = \frac{\nu - \nu_{if}}{\nu_D}$$

$$z'(t) = \frac{\Delta'(\tilde{v}t)}{\nu_D} + i\frac{\Gamma'(\tilde{v}t)}{\nu_D} \qquad \text{(VIII.1.12)}$$

$$z(t) = \frac{\Delta(\tilde{v}t)}{\nu_D} + i\frac{\Gamma(\tilde{v}t)}{\nu_D}$$

Remark: if speed dependence neglected, ie $\Delta'(\tilde{v}t) = \Gamma'(\tilde{v}t) = 0$, we reduce equation (VIII.1.11) to a Voigt profile formula:

$$I_{\text{Voigt}}(\nu) = \frac{\pi^{-3/2}}{\nu_D} \int_{-\infty}^{+\infty} \exp(-t^2) \ \text{Im}\left\{ \frac{1}{x+t\ -iy} \right\} dt \ , \ x = \frac{\nu - \nu_{if}}{\nu_D}, y = \frac{\Gamma}{\nu_D} \qquad \text{(VIII.1.13)}$$

VIII.2 Appendix 2: Derivation of Speed dependent Rautian profile formula

In order to get the speed dependent Rautian profile that has the form:

$$I_{sdRaut}(\nu) = \frac{1}{\pi} \text{Im} \left\{ \frac{i \iiint \frac{f_{MB}(\vec{v})}{A(\vec{v},\nu)} d^3\vec{v}}{i - \nu_{VC}^H \iiint \frac{f_{MB}(\vec{v})}{A(\vec{v},\nu)} d^3\vec{v}} \right\}, \tag{IV.39}$$

where $A(\vec{v},\nu) = \nu - \nu_{if} - \vec{k}\vec{v} - \Delta(v) - i(\Gamma(v) + \nu_{VC}^H)$,

we start from the general normalized absorption profile valid for isolated line when Dicke effect, Doppler effect as well as the dependence of collisional line-broadening and line-shifting parameters on speed of the molecule v are considered (see Eq. IV.4-5), counting here with real part of the complex spectral density $\text{Im}\{iZ\} = \text{Re}\{Z\}$:

$$I(\nu) = \frac{1}{\pi} \text{Re} \left\{ \int_0^{+\infty} \exp(i\nu t) \, C(t) \, dt \right\}, \tag{VIII.2.1}$$

where $C(t)$ is matrix element of the dipolar autocorrelation function, that can be detailed as:

$$C(t) = \iiint C(\vec{v}, t) \, d^3\vec{v}, \quad C(\vec{v}, t=0) = f_{MB}(\vec{v}) \tag{VIII.2.2}$$

Differential equation for $C(\vec{v}, t)$ gives:

$$\begin{aligned}
\frac{d}{dt} C(\vec{v}, t) = & \left[i\left(\nu_{if} + \vec{k}.\vec{v} + \Delta(v)\right) - \Gamma(v) \right] C(\vec{v}, t) \\
& - \iiint f(\vec{v} \to \vec{v}') \, C(\vec{v}, t) \, d^3\vec{v}' \\
& + \iiint f(\vec{v}' \to \vec{v}) \, C(\vec{v}', t) \, d^3\vec{v}'
\end{aligned} \qquad , \tag{VIII.2.3}$$

where $f(\vec{v}' \to \vec{v})$ is frequency of velocity change $\vec{v}' \to \vec{v}$ due to collisions.

Hard collision model sets:

$$f(\vec{v}' \to \vec{v}) = f_{MB}(\vec{v}) \, \nu_{VC}^H \tag{VIII.2.4}$$

Using

$$\widehat{C}(\vec{v},\nu) = \int \exp(i\nu t) C(\vec{v},t) \, dt \,, \tag{VIII.2.5}$$

we get:

$$\mathrm{i}\,v\,\widehat{C}(\vec{\mathbf{v}},\nu)\;-\;f_{\mathrm{MB}}(\vec{\mathbf{v}})=\left[\mathrm{i}\left(\nu_{\mathrm{if}}+\vec{\mathbf{k}}.\vec{\mathbf{v}}\;+\;\Delta(\mathrm{v})\right)-\Gamma(\mathrm{v})\right]\widehat{C}(\vec{\mathbf{v}},\nu)$$
$$-\nu_{\mathrm{VC}}^{\mathrm{H}}\;\widehat{C}(\vec{\mathbf{v}},\nu)\;+\;\nu_{\mathrm{VC}}^{\mathrm{H}}\,f_{\mathrm{MB}}(\vec{\mathbf{v}})\;\iiint\widehat{C}(\vec{\mathbf{v}}',\nu)\,\mathrm{d}^{3}\vec{\mathbf{v}}' \tag{VIII.2.6}$$

If we put $A(\vec{\mathbf{v}},\nu)\;=\nu-\nu_{\mathrm{if}}-\vec{\mathbf{k}}.\vec{\mathbf{v}}\;-\;\Delta(\mathrm{v})-\mathrm{i}\Gamma(\mathrm{v})-\mathrm{i}\nu_{\mathrm{VC}}^{\mathrm{H}}$, $\tag{VIII.2.7}$

then we can write also:

$$-f_{\mathrm{M}}(\vec{\mathbf{v}})=-\mathrm{i}A(\vec{\mathbf{v}},\nu)\,\widehat{C}(\vec{\mathbf{v}},\nu)+\;\nu_{\mathrm{VC}}^{\mathrm{H}}\,f_{\mathrm{MB}}(\vec{\mathbf{v}})\;\iiint\widehat{C}(\vec{\mathbf{v}}',\nu)\,\mathrm{d}^{3}\vec{\mathbf{v}}', \tag{VIII.2.8}$$

which leads to:

$$\widehat{C}(\vec{\mathbf{v}},\nu)\;=\frac{f_{\mathrm{MB}}(\vec{\mathbf{v}})}{\mathrm{i}A(\vec{\mathbf{v}},\nu)}+\frac{\nu_{\mathrm{VC}}^{\mathrm{H}}\,f_{\mathrm{MB}}(\vec{\mathbf{v}})}{\mathrm{i}A(\vec{\mathbf{v}},\nu)}\iiint\widehat{C}(\vec{\mathbf{v}}',\nu)\,\mathrm{d}^{3}\vec{\mathbf{v}}' \tag{VIII.2.9}$$

After integration over velocities and realizing that:

$$\iiint\widehat{C}(\vec{\mathbf{v}}',\nu)\,\mathrm{d}^{3}\vec{\mathbf{v}}'\;=I(\,\nu\,), \tag{VIII.2.10}$$

we obtain finally:

$$I_{\mathrm{sdRaut}}(\nu)=\frac{1}{\pi}\mathrm{Re}\left\{\frac{\displaystyle\iiint\frac{f_{\mathrm{MB}}(\vec{\mathbf{v}})}{\mathrm{i}A(\vec{\mathbf{v}},\nu)}\mathrm{d}^{3}\vec{\mathbf{v}}}{1-\nu_{\mathrm{VC}}^{\mathrm{H}}\;\displaystyle\iiint\frac{f_{\mathrm{MB}}(\vec{\mathbf{v}})}{\mathrm{i}A(\vec{\mathbf{v}},\nu)}\mathrm{d}^{3}\vec{\mathbf{v}}}\right\} \tag{VIII.2.11}$$

The equation (VIII.2.11) can be transformed using equality $\mathrm{Im}\{\mathrm{i}Z\}=\mathrm{Re}\{Z\}$ to:

$$I_{\mathrm{sdRaut}}(\nu)=\frac{1}{\pi}\mathrm{Im}\left\{\mathrm{i}\,\frac{\displaystyle\iiint\frac{f_{\mathrm{MB}}(\vec{\mathbf{v}})}{\mathrm{i}A(\vec{\mathbf{v}},\nu)}\mathrm{d}^{3}\vec{\mathbf{v}}}{1-\nu_{\mathrm{VC}}^{\mathrm{H}}\;\displaystyle\iiint\frac{f_{\mathrm{M}}(\vec{\mathbf{v}})}{\mathrm{i}A(\vec{\mathbf{v}},\nu)}\mathrm{d}^{3}\vec{\mathbf{v}}}\right\}=\frac{1}{\pi}\mathrm{Im}\left\{\frac{\displaystyle\iiint\frac{f_{\mathrm{MB}}(\vec{\mathbf{v}})}{A(\vec{\mathbf{v}},\nu)}\mathrm{d}^{3}\vec{\mathbf{v}}}{1-\nu_{\mathrm{VC}}^{\mathrm{H}}\;\displaystyle\iiint\frac{f_{\mathrm{MB}}((\vec{\mathbf{v}}))}{\mathrm{i}A(\vec{\mathbf{v}},\nu)}\mathrm{d}^{3}\vec{\mathbf{v}}}\right\}$$

$$=\frac{1}{\pi}\mathrm{Im}\left\{\frac{\mathrm{i}\displaystyle\iiint\frac{f_{\mathrm{MB}}(\vec{\mathbf{v}})}{A(\vec{\mathbf{v}},\nu)}\mathrm{d}^{3}\vec{\mathbf{v}}}{\mathrm{i}-\nu_{\mathrm{VC}}^{\mathrm{H}}\;\displaystyle\iiint\frac{f_{\mathrm{M}}(\vec{\mathbf{v}})}{A(\vec{\mathbf{v}},\nu)}\mathrm{d}^{3}\vec{\mathbf{v}}}\right\} \tag{VIII.2.12}$$

Note that if we neglect the Rautian narrowing parameter $\nu_{\mathrm{VC}}^{\mathrm{H}}$, the speed dependent Rautian profile converge to speed dependent Voigt profile:

if $\nu_{\mathrm{VC}}^{\mathrm{H}}=0$, then $I_{\mathrm{sdRaut}}(\nu)=\mathrm{Im}\left\{\iiint\frac{f_{\mathrm{M}}(\vec{\mathbf{v}})}{A(\vec{\mathbf{v}},\nu)}\mathrm{d}^{3}\vec{\mathbf{v}}\right\}=I_{\mathrm{sdVoigt}}(\nu)$ $\tag{VIII.2.13}$